TÉCNICO LISBOA

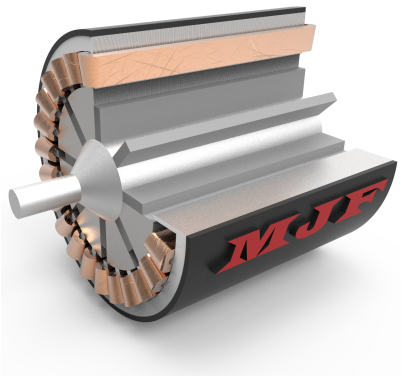

Design and Implementation of a 20 kW, 12000 RPM Permanent Magnet Synchronous Motor (PMSM) for the IST Formula Student Powertrain

João Gonçalo Viseu Vieira Sarrico

Thesis to obtain the Master of Science Degree in

Electrical and Computer Engineering

Supervisor(s): Prof. Dr. Paulo José da Costa Branco
Prof. Dr. João Filipe Pereira Fernandes

Examination Committee

Chairperson: Prof. Dr. Rui Manuel Gameiro de Castro
Supervisor: Prof. Dr. Paulo José da Costa Branco
Member of the Committee: Prof. Dr. Silviano Santos Rafael

November 2017

Dedicated to my mother for all the unconditional support in everything and to my father for instilling the passion for motorsport.

Acknowledgments

I would like to leave here a remark of appreciation to all the people who helped me during this journey. It was a big one, more than 2 years of work squeezed to be incorporated inside this master thesis, a work that started long before the initial date of this thesis. It was a journey marked by ups and downs, a lot of new challenges that never stopped from coming up, not even at the end. But, maybe because of that, it was a wonderful journey where, bad or good solutions were discovered and used that allowed this project to evolve a little more. Even when major failures happened, and time and money limitations almost ceased the MJF project from being created.

This work could have never been done without the help of many people during this journey, in many different ways: they teach me how to use different softwares, assisted me with all my issues and questions, motivated me to go further.

First of all, and because family always comes first, to my mother, my hero, who supported and supports me relentlessly not only during this tasks but in all the tasks a life can have. To my father for giving me this passion for motorsport and the mindset to never give up. To my beautiful sisters Marta and Rita for all the joy, happiness and companionship during my life. Also to Filipa, not only for all the support, care, understanding and unconditional love, but also for the exhaustive help during this project. I cannot forget, of course my grandma, and both grandpas for all the love given. To my cousin Luis, who left us too early, for being a human example of friendship.

Next to my teacher and advisor on this work, Prof. Paulo Branco, who always tried to show me the correct path and fought a lot for me in order to provide the basic materials needed for this thesis. A new friend that I will keep in my future life. Also, my co-advisor, Prof. João Fernandes for all the time spent teaching me how to use the FEA Software and the assistance, when I assumed I had reached a dead-end.

To FST Lisboa team, who made this project possible. Providing the sponsorships, materials, knowledge and assist during all the process. Specially to Pedro for the big talks and lessons about electrical stuff and more, a true friend, who never failed me. To Rui, who cannot hear a no for an answer, crucial during the bad moments (and not only) and always there to cheer me up. To Vicktor, gigantic Viktor, who supported me with a lot of mechanical stuff, always with a lot of enthusiasm and willingness to help. He is clearly the number one fan of the MJF project. Fontes, the man most cited in this thesis, that (together with Filipa) assured to keep the MJF cool(ed). “Prof.” Santos, for his exhaustive assistance, during the development of the optimization script and for reviewing my thesis. Bruno for the assistance on the test-bench design and manufacture. I will never forget the pain he went through, just to drill a hole on a 15 mm sheet of the test-bench base. To Carlos who always tried to assure that my decisions were the correct ones throughout the project.

To my friends, from all over the places, university, school,etc, who made this last 6 years of college easier with all the support and companionship. To Francisco and Sá, to whom I owe a big debt from pulling me out of work. To Machado, Lopes, Prata, Xavier, Renato and Kevin for the fellowship shown during the first years in the university. To Carlos, Luís, Michael and Alykhan, friends for life, for all the

big moments and adventures during the last 15 years.

To Lehmus (Portugal), personally represented by Dr. Nuno Santos, that together with Mr. Carlos were responsible for powering the MJF motor with the professional winding carried out and all the explanations involved.

To Edeatech, personally represented by Eng.Ventura Belinho for manufacturing the most complex piece of art of the MJF, the shaft, and also for trusting on this project and will continue to do so in the future versions.

Prof. Luís Sousa for providing his powerful computers to run more than 2000 hours of extensive studies and for all the effort put on the team, a true example of complicity.

To Mike for not only providing shelter for me in his home in the UK, but also contributed to improve my thesis English by reviewing it.

To Mr. Duarte, Mr. Joao and Mr. Pedro for assisting me during the tests and also during the manufacturing process when using the lathe and milling cutter.

To my faculty Instituto Superior Técnico for contributing to my intellectual formation, having given me the toughest challenges.

To Colégio Militar for contributing to my formation as a person and for given me friends for life. Part of what I am today I owe to this School.

Resumo

Com o crescimento de carros híbridos e 100% eléctricos em competicção automóvel, novas máquinas eléctricas estão a ser desenvolvidas.

Esta tese trata o projecto, fabrico e teste de um motor síncrono de ímanes permanentes para um carro eléctrico de Formula Student, onde se requer uma alta relação peso/potência e torque/potência. Especificamente, definiu-se um motor capaz de gerar 20 Nm, atingir velocidades de 12000 RPM e uma potência de pico de 20 kW. Uma análise aos materiais e métodos de fabrico para cada componente do motor foi executada, permitindo a seleção dos que melhor se adequam.

Durante a fase de projecto e depois de terem sido seleccionados os materiais e métodos, um *script* de optimização foi desenvolvido por forma a identificar os parâmetros que melhor beneficiam a produção de binário, cumprindo os constrangimentos definidos. Esse *script* foi melhorado com base nas conclusões retiradas dos ensaios experimentais. Análises mecânicas e térmicas foram realizadas para aumentar a robustez e facilidade de manufactura da máquina. Os métodos utilizados durante a manufactura do motor e da bancada de ensaios incluíram corte-laser, corte por jacto de água, fresa CNC e torno mecânico.

Um estudo relativo à organização das bobines foi realizado para validar a capacidade do motor atingir 12000 RPM e um torque de 20 Nm sem atingir o limite térmico. Testes de performance e eficiência foram realizados, posteriormente. Os requerimentos do projecto foram garantidos, apesar de algumas limitações terem comprometido alguns resultados. Finalmente, foram recomendadas alterações com vista a melhorar a performance do motor.

Palavras-chave: *Formula Student* carro de competição eléctrico, Motor síncrono de ímanes permanentes, alta performance, algoritmo de optimização, projecto/construção/teste de motor eléctrico

Abstract

With the recent growth in hybrid and fully electric race car competitions, new electric machines technologies are being developed.

This thesis concerns the design, manufacture and test of a PMSM for a Formula Student electric car requiring a high ratio of weight/power and torque/power. Specifically, it was defined an high-performance motor suitable for the race car, capable of producing 20 Nm, rotating at 12000 RPM and with a peak power of 20 kW. Analyses of the materials and manufacturing processes for each part of the motor have been performed, allowing the selection of those most suitable for the application.

In the design phase and after having taken into account the material and manufacturing methods selected, an optimization script was developed to identify the best parameters regarding the torque production while complying with the relevant constraints. Improvements to the script were implemented after the test validation. Mechanical and thermal analyses were conducted in order to increase motor robustness and manufacturability. The main manufacturing methods used for the motor and test bench manufacturing included laser cutting, water-jet, CNC milling and lathe turning methods.

Windings tests were performed to validate the layout producing a back-electromotive force capable of reaching 12000 RPM and a maximum torque of 20 Nm without reaching the thermal limits. Subsequently, the final winding, performance and efficiency tests were performed. The design requirements values were reached, although few limitations have compromised some of the results. Furthermore, concluding this thesis, several changes that can improve the motor performance have been recommended.

Keywords: Formula Student Electric Racecar; Permanent Magnet Synchronous Motor; High Performance; Optimized geometry; Electric motor design/manufacture/test.

Contents

List of Tables

List of Figures

Nomenclature

Greek symbols

$\alpha\beta$	Stator-fixed coordinates
$\bar{\epsilon}$	Electromotive force voltage [V]
μ_0	Permeability [H/m]
ω	Angular Velocity [rad/s]
ω, ω_r, ω_s	Mechanical rotor velocity, rotor and stator circuit velocity [rad/s]
ϕ_{coil}	Flux through each coil [Wb]
ψ_s, ψ_r	Vector of stator, rotor flux [Wb]
ψ_{sd}, ψ_{sq}, ψ_{rd}, ψ_{rq}	dq components of the stator, rotor flux [Wb]
σ	Tensile Stress [MP$_a$]
σ_{Neod}	Electric conductivity of Neodymium magnets [S/m]
τ	Shear Strength [MP$_a$]
θ	Displacement angle [rad]
ϑ, ϑ_s	Rotor angle, angle of flux orientated coordinate [rad]
B_ω	Tangential component of the flux density [T]
$i_{s\alpha}, i_{s\beta}$	$\alpha\beta$ components of the stator current [A]

Roman symbols

a_c	Acceleration [m/s^2]
A_{bridge}	Magnet-bridge thickness [m]
A_{Fin}	Fin Area [m^2]
AS	Air-gap size [mm]
B	Magnetic flux density [T]

b_m Magnet width [m]

B_r Radial component of the flux density [T]

D Electric Displacement [C/m^2]

dq Field synchronous or rotor flux orientated coordinate system

dS Differential surface area in cylindrical coordinates

E Electric Field [N/C]

F Force [N]

f_s Frequency of stator [Hz]

H Magnetic field strength [A/m]

h_m Magnet height [m]

i Current [A]

i_d, i_q dq components of the stator, rotor current [A]

i_s, i_r Vector of stator current, vector of rotor current [A]

I_{RMS} Root mean square current [A]

i_{sd}, i_{sq}, i_{rd}, i_{rq} dq components of the stator, rotor current [A]

i_{su}, i_{sv}, i_{sw} Stator current of phases u, v, w [A]

J_z Induced current density in z axis [J/m^2]

K_{Eddy} Eddy constant

K_{hyst} Hysteresis constant of the material

L Active length of the machine [m]

l_m Magnet length [m]

LT Length of teeth [mm]

m Mass [kg]

MT Magnet length [mm]

MW Magnet width [mm]

N_T Number of turns of each coil

n_{pp} Number of pair of poles

P Power [kW]

p Number of poles

P_{Iron} Iron losses [W]

P_{Joule} Joule Losses [W]

P_{Neod} Magnet losses [W]

Q_s Number of slots

R Resistance [Ω]

r Radius of the closed surface in the motor airgap [m]

r_s Middle Airgap radius [m]

RR Rotor radius [mm]

SR Shaft radius [mm]

t Time [s]

T_e Eletromagnetic torque [Nm]

TW Teeth width [mm]

U Stator phase U

u_s, u_r Vector of stator, rotor voltage [V]

V Stator phase V

v Velocity [m/s]

W Mechanical frequency of the rotor [rad/s]

W Stator phase W

$W_{coenergy}$ Magnetic Coenergy [J]

Subscripts

n_1 Outward normal from the object

Superscripts

T Transpose

Glossary

AC Alternating current.

BEMF Back Electromotive Force.

BPM Brushless permanent magnet.

CAD Computer-aided design.

CU Control Unit.

DC Direct current.

EMF Electromotive Force.

F1 Formula One.

FEA Finite Element Analysis.

FoS Factor of Safety.

FS Formula Student.

FSAE Formula Society of Automotive Engineers.

FSG Formula Student Germany.

FSSpain Formula Student Spain.

FST Formula Student Tecnico.

FST 07e Formula Student Técnico seventh protype car, the fourth fully electric one

FST 08e Formula Student Técnico eight protype car, the fifth fully electric one

FSUK Formula Student United Kingdom.

GA Genetic Algorithm.

IGBT Insulated-Gate Bipolar Transistor.

IPM Interior permanent magnet.

IST Instituto Superior Técnico.

kW Kilowatt.

LMP1 Le Mans Prototype class one.

mmf Magnetomotive Force.

MST Maxwell Stress Tensor.

NASA National Aeronautics and Space Administration.

NdFeB Neodymium Iron Boron.

Nm Newton meter.

PM Permanent Mgnets.

PMSM Permanent Magnet Synchronous Machines.

RMS Root Mean Square.

RPM Revolutions per minute.

SAE Society of Automotive Engineers.

SmCo Samarium Cobalt.

SMPM Surface mounted permanent magnet.

SPSM Salient-Pole Synchronous Machines.

SRA Stress Relief Annealing.

SW SolidWorks.

TM Terminal Module.

WEDM Wire Electric Discharge Machining.

Chapter 1

Introduction

1.1 Framework and motivation

The main objective of this thesis is to contribute to the development of an electric motor for the FST 08e car, known as the MJF motor. The FST 08e is the future race car of the Formula Student Técnico FST Lisboa team. Formula Student FS is a global competition for engineering students where teams from universities around the world design, manufacture and race their cars under competitive conditions.

The overall motivation of the work is justified by the following text [1]: *"[...]the competition aims to inspire and develop enterprising and innovative young engineers. [...] The format of the event is such that it provides an ideal opportunity for the students to demonstrate and improve their capabilities to deliver a complex and integrated product in the demanding environment of a motorsport competition."*

In the past, the FST team has participated with seven car versions, the last four ones being electrically propelled vehicles, which are becoming more common on the track.

Figure 1.1 shows the FST 07e car which raced in the 2017 season. The latest is the seventh car fully designed and built by the team, and the fourth electric one. This car will be used in the near future to validate an improved version of the motor proposed by this thesis. In fact, next year's formula student car, the FST 08e, will incorporate a powertrain including the motor developed and validated under the present thesis, as it met all the dynamic and performance goals defined by the FST Lisboa team.

Figure 1.2 and Figure 1.3 show the evolution of the FST Lisboa electric motors. As it can be seen in these figures, the electric motor, which is one of the most important systems of the car, has never been designed in the previous four FST electric powertrain prototypes. Over the past years, the electric motors that were used in the cars were always different. This was a result of the main team philosophies, which changed from one prototype to the next, according to the results achieved and derived by the objectives established by the different teams. All the different powertrains have used different commercial motors available on the market and because they were originally built to accomplish different purposes, all cars needed to be adapted in some way to the electric motors selected.

Figure 1.1: The FST07e car with the Powertrain members during its official presentation.

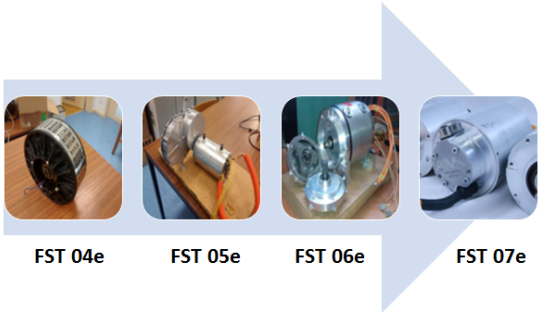

Figure 1.2: FST Lisboa electric motor evolution through different cars.

	FST 04e	FST 05e	FST 06e	FST 07e
P_nom [kW]	12	27.6	30.4	12.3
P_max [kW]	**30**	**32**	**50**	**30***
T_nom [Nm]	30	12	65	9.8
T_max [Nm]	**53**	**24**	**107**	**21**
N_nom [RPM/1000]	4	25	5	12
N_max [RPM/1000]	6	40	8.5	20
Weight[Kg]	10.9	7.15	13.6	3.55
Ratio[kW/Kg]	**2.75**	**4.5**	**3.1**	**8.5**

(a) Table with motor specifications. * Not specified on the datasheet.

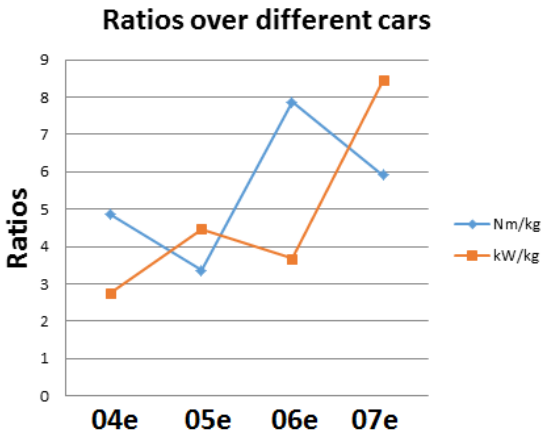

(b) Evolution of Nm per kg and kW per kg of the motors.

Figure 1.3: Characteristics of the motors of the FST Lisboa cars.

In this context, the current team decided to work on the design and manufacture of a tailored-made motor. The purpose was to further learn about electric traction systems of racing cars and also to design the system according to the car specifications and not the opposite, insuring the motor suitability for the FS race car. This choice enables the improvement of the system in the future, improving its scalability, as the knowledge and the manufacture of the electric motor is being optimized, avoiding the dependency on commercial solutions available in the market.

1.2 Objectives and goals of the dissertation

The proposed objectives of this thesis are the following:

1. To present the reviewed literature on the use of Permanent Magnet Synchronous Machines (PMSM) in electric racing cars;
2. To study different magnetic circuit geometries for the PMSM that meet the given performance requirements of the desired maximum power, maximum speed and maximum torque, respectively: 20 kilowatt (kW), 12000 Revolutions per Minute (RPM) and 20 Newton meter (Nm);
3. To optimize the magnetic circuit of the PMSM using an Evolutionary algorithm coupled to a Finite Element Analysis (FEA) program. The objective functions of the algorithm will be associated to the electromagnetic torque, balanced stator windings distribution and minimization of the magnetomotive force harmonics in the air-gap. Constraints will be the volume, power losses and weight of the motor;
4. To build a prototype based on the results of item 3) using suitable materials and stator iron laminate cutting methods. After assembling the motor, experimental tests will be performed to obtain the electromechanical motor characteristics.

Within the FST Lisboa team framework, the objective of this thesis was to optimize and contribute to the technological advancement of the powertrain system, mainly regarding the electric motor of the new vehicle, the FST 08e. Experimental tests and validation of the new electric motor are also a requirement. In parallel, new knowledge, both theoretical and practical, about the car powertrain system will be obtained within the scope of this work.

To develop an electric motor there are several areas that need to be considered. Within the framework of this thesis, the project is focused on the areas of electromagnetics and mechanics. Specifically, this included the design and manufacture of the main components of the motor: shaft, motor housing, rotor and stator. Additionally, other components of the overall vehicle powertrain system were also considered, such as encoders, inverters and batteries.

In terms of general design and manufacture processes, this thesis included consideration of design requirements, technical analysis, material selection, system integration and manufacturing processes. Contributions were also made toward the motor prototype manufacturing and its testing.

In conclusion, the design of this bespoke electric motor aims to increase the electromechanical performance and consequently the competitiveness of the car, allowing the FST Lisboa team to achieve three main goals (left diagram in Figure 1.4):

1. To fully adapt the design parameters of the electric motor to the car requirements;
2. To undertake continuous optimization of the motor;
3. To acquire and develop an overall knowledge of the electric traction system.

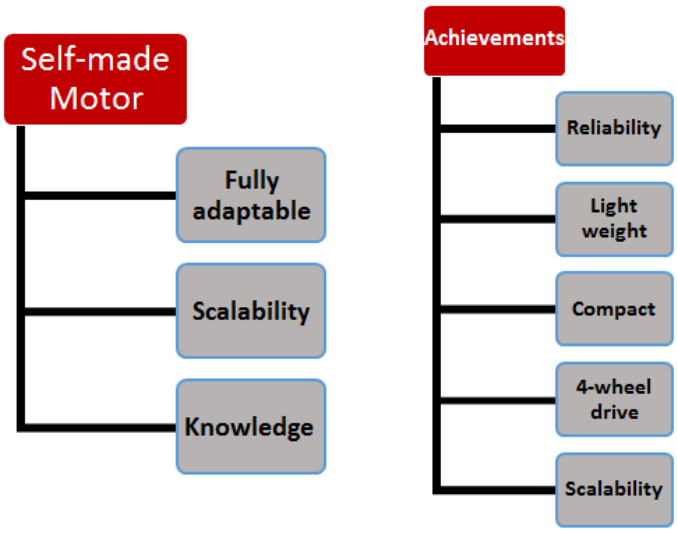

Figure 1.4: FST 08e Powertrain main goals and achievements.

Oriented outcomes of this research include the following achievements for the new tailored motor (right diagram in Figure 1.4):

1. Maintain and improve reliability;
2. Decrease the overall weight;
3. Achieve a more compact solution (less volume);
4. Provide a suitable control solution for a 4-wheel drive (4WD) car;
5. Scalability in the design as in potential to be enlarged.

1.3 Structure of the dissertation

The present dissertation comprises six chapters. Following this introduction, Chapter 2 presents a revision of the main issues related to electric motors, namely for two main phases: i) to select the motor type and ii) to proceed to its design. Particular emphasis is given to the materials and manufacturing technologies to fabricate the motor's components. A review of electric motor integration in race cars, (in the FST 07e car where the FST 08e motors will be tested) and of motor controllers are also presented on this chapter.

Chapter 3 is focused on the motor design and the definition of the requirements, taking into account an optimal lap simulation.

Chapter 4 presents a detailed description of the prototype manufacturing set-up, processes and instrumentation used. The test bench design and manufacture is also included in this chapter.

Chapter 5 presents overall testing of the prototype and the results obtained.

Finally, Chapter 6 summarizes a set of conclusions and the main contributions of this dissertation. It also includes some comments for future development.

Chapter 2

Technical Overview

2.1 Introduction

This study concerns the electric motor for the FST 08e car. Three main tasks were performed: first, the design of the motor prototype, next, the manufacturing, and finally, testing of the prototype.

In this chapter the main methodologies and approaches for electric motor design are presented. Also, an overview concerning the motor main components and the most common electric motor types is presented. Special emphasis is applied to PMSM, the solution adopted for the FST 08e car.

Besides the motor design, this dissertation was strongly focused on manufacturing of the prototype. Therefore, the technical overview also shows the main technologies analysed for the construction of the different components for the motor prototype.

2.2 Electric race cars

"In order to be competitive in this business it is necessary to operate at the outer edges of the performance envelope. The closer we come to the edge, the greater the risk of falling off becomes." [2]

The objective of a race car is ultimately simple: to travel a fixed distance in less time than the other teams, independently of the type of that competition, from a sprint race to endurance. Within this goal, teams must be the most effective within their limitations of human, financial and temporal resources.

In a racing environment, it is very important to understand the general principles of Vehicle Dynamics, which can be summarized as the study of the forces acting on vehicles in motion and the changes in its response [2].

Vehicle Dynamics can be divided into the following topics in order of their influence on the track time: linear acceleration, braking capacity, cornering power, top speed, controllability and response.

The linear acceleration is the single most important aspect in race car performance. The ability to accelerate faster depends on the power available at the driving wheels, tractive capacity of the driving tires, vehicle weight, aerodynamic drag, rolling resistance and component rotational inertia.

The braking capacity is relatively less important than the ability to accelerate because less time is

spent braking than accelerating. It is essentially the acceleration reversed but it differs in the number of tractive wheels versus the braking wheels (normally all four wheels brake).

Above all, race cars are required to go around corners. In the Formula Student competition, this aspect is most significant, as the tracks have short straight lines and many corners. Firstly, the faster the car corners, the less time is required to cover the same distance; second, a car that corners at higher speed does not waste time accelerating when exiting the corner. The most important factors concerning cornering are outside the scope of this thesis. They include suspension geometry, vehicle load transfer characteristics, vehicle downforce, tires, car weight and height of the vehicle's center of gravity.

Maximum speed is not so important in race cars as it appears to be, especially at Formula Student level, where the distances involved are not great enough for the cars to reach it. The factors controlling top speed are the net power at driving wheels, aerodynamic drag and rolling resistance.

Lastly, the controllability and response of the car are a consequence of the compromises resulting from the combination of the different systems of the vehicle. The car must be driven by a pilot, and the easier it is to handle, the better the lap time will be. Almost all factors affect the controllability and response of a race car, the most important ones include centre of gravity height, load transfer characteristics, suspension geometry, amongst others.

In the last few years, electric cars have made an important step into racing/motorsport environments. With the development of electric traction systems technology and the external pressure to adopt environmentally friendly technologies, the electric race car has increased its visibility. The most well-known motorsport competition, Formula 1, has adapted their cars to integrate a hybrid system composed of an internal combustion engine with an electric motor (and the associated inverters and batteries) in order to increase the car dynamics, especially during the starts and after curves (when most power is needed). Formula Electric was created in 2014 and is considered to be the F1 competition for electric vehicles. During the first season, all the cars were equal, but in the 2015-2016 season, the teams were allowed to pick their own powertrain system. Also the Le Mans Series adapted their cars (in the Le Mans Prototype category one LMP1) to hybrid powertrains to increase the power and dynamic behavior of the car.

The development of electric motive technology for race cars provides a significant opportunity to test and validate state of art technology, allowing integration into road cars in future years.

2.2.1 Formula Student

Formula Student is an international competition for engineering students organized by Society of Automotive Engineers (SAE). Several individual competitions take place in different countries and circuits each year, which brings different challenges. In Europe, the biggest competitions are Formula Student Germany (FSG), Formula Student United Kingdom (FSUK) and Formula Student Spain (FSSpain). Other important competitions in Europe are FS East, FS Czech and FS Italy.

In each competition, students are challenged to design, build and test a single-seat race car according to the Formula SAE specific regulations.

Students can compete in three different concepts in each competition: combustion car, electric car

and driverless car (currently only at FSG). The goal of the competition is to offer future engineers experience with:

- Engineering design;
- Cost and Manufacturing;
- Running a small business;
- Working in an international environment;
- Working with tight deadlines.

All competing cars are prototypes and are judged by automotive engineers on static aspects and by proving its performance in four dynamic events concerning:

- Acceleration - from stand-still on a 75 m straight (75 pt);
- Skid Pad - measuring cornering speed (75 pt);
- Autocross - racing one standing lap on a 1 km track (100 pt);
- Efficiency - measuring energy consumption (100 pt);
- Endurance - 22 km long endurance race (325 pt).

2.2.2 FST 07e car

The FST 07e prototype car is the fourth electric car fully designed and manufactured by the FST Lisboa team. FST 07e is a 4-wheel drive, and weighs approximately 220 kg. Being the first 4-wheel drive powertrain designed by the team, it provides the opportunity to develop self-made electric traction motors as the size, power, torque and cost of this system are easier to manage.

Figure 2.1 presents a schematic of the powertrain of the FST 07e car. It is composed of four electric motors, each controlled by one inverter (which includes the motor controller for each motor). All the inverters are connected to the battery pack inside the accumulator container indicated in Figure 2.1. The total voltage of the battery is 600 V at maximum charge and 460V when discharged. The battery pack is composed by 144 cells in series with 2 in parallel.

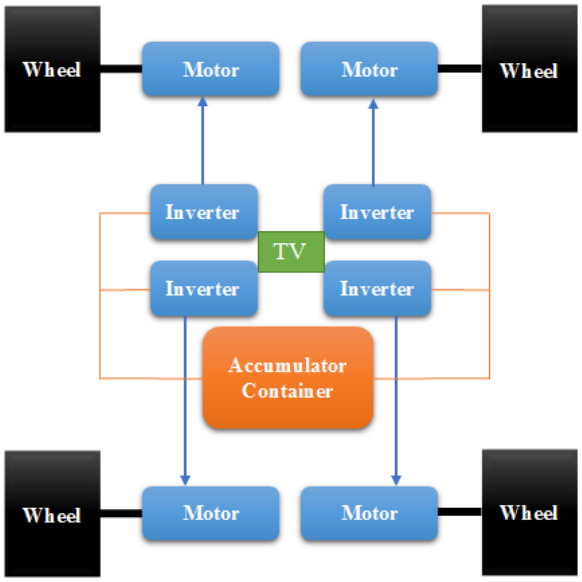

Figure 2.1: FST 07e powertrain schematic, with one motor and controller per wheel, torque-vectoring system and accumulator container.

The inverters are responsible for converting the Direct-Current DC of the batteries to the Alternating-Current AC feeding the motors. The power flowing of each inverter to the motor is managed by a self-developed system made by the team, called Torque Vectoring. This system defines a set-point of torque and velocity to each motor independently according to the driving situation, i.e. in the case of a corner, the outer wheels must have higher rotational speed when compared with the inside wheels, working as an electric differential [3].

Figure 2.2 shows a solid model of the drivetrain of the car. It is divided into the motor which is connected to the transmission box that is attached to the upright of the suspension system.

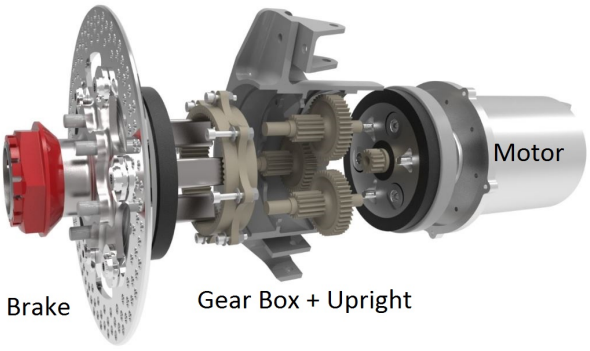

Figure 2.2: FST 07e motor, transmission box, upright and brake integration from right to left.

The transmission box, optimized for the AMK motors integrated in this car (Appendix A) has a gear ratio of 1:15 and is composed by two stages of spur gears having a theoretical efficiency of 97.6% and a mass of about 1.5 kg.

As the goal is to test the next version of the electric motor designed in this thesis in the FST 07e car, some constraints to the motor design were set, as for example, the weight, the volume and the outer diameter. These constraints will be further analysed in the next chapter.

2.3 Electric machine design: methodologies and approaches

The design of an electric machine is a multidisciplinary task and different specialization knowledge and physics must be considered, namely for developing electromagnetic, thermal, mechanical and electronic analyses. Electric machine development includes the definition of the design requirements, operating conditions, and requires the selection of materials, manufacture of the prototype as well as testing. Two design approaches are possible: i) top-down design and ii) bottom-up design [4].

In the first approach - top-down design - the development of the motor is carried out working in parallel within the different physical principles in a systemic manner. This is only possible when the knowledge of the overall system is established. The problem is solved optimizing the overall multi-physics system, requiring a high knowledge of boundaries inter-relations.

In the second approach – bottom-up design – the development of the electric machine is carried out by initially working at component level followed by integration on the overall system. This approach can be easier and faster to implement whilst the knowledge of the overall system is not needed for those working outside their expertise areas.

For the electric machine proposed in this thesis, the bottom-up design was chosen not only because it is the first electric motor to be developed by the FST Lisboa team, but also because there is a lack of experience about this type of traction system.

Designing an electric machine is also an iterative task. The machine can be improved as time and knowledge invested in its development increases. Hence, it is very common to iterate the project many times, namely in two critical periods of the electric machine development: the beginning of the project and whenever, within the bottom-up design approach, a component is optimized taking into account the coupling between two or more physical principles (eg: thermo-electric, electro-mechanic).

2.4 Electric motor components

Notice that an electric machine can work both as a motor or a generator depending on the direction of the current, a generator creates electric power when receiving mechanic power. A motor has the opposite process. So in conclusion, throughout this thesis the MJF machine will be refereed as a motor since it will be used on the car mainly in this configuration (it will work as a generator only when the brake regeneration is active).

The main motor components designed within the scope of this thesis, and later manufactured, include the shaft, the motor housing, the stator core, the coils (and their distribution) and the rotor.

The shaft is used in the electric motor to transmit torque and power to an external load. This component is subjected to various combined mechanical effects of tension, compression, bending and torsion during operation. Therefore, shafts are typically designed for maximum stiffness and rigidity and minimum deflection, in order to maintain the shaft stress/strain within the allowable limits, under different loading and operating conditions.

The motor housing is composed of covers responsible for guaranteeing the structure of the motor

and also to protect its components against the insertion of undesirable materials such as dust or water.

The stator core is normally the stationary piece that holds the windings in the inner surface slots. This component is responsible for creating a rotating magnetic field in the air-gap as alternating currents pass by. Normally, the stator is the outer piece, being its core made by several laminated electrical steel pieces that are stacked together and separated by isolating glue.

The rotor is the rotating component that accommodates the Permanent Magnets (PM) (in the case of PMSM) and that follows the rotational magnetic field created by the stator windings, producing mechanical power.

2.5 Types of electric machines

Figure 2.3 summarizes the most important types of electric motors. Electric machines/motors can be divided into two major types: DC motors (with brushed or brushless solutions) and AC motors (with induction or synchronous solutions).

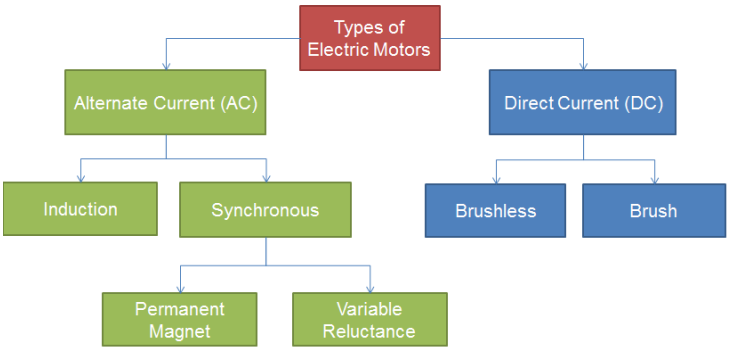

Figure 2.3: Main types of electric machines/motors.

The overall performance of a FS car depends on light weight and compact solutions, including for the electric motor. This first main design decision has taken into account the main advantages and disadvantages of Synchronous motors, as indicated in Figure 2.4.

These motors are nowadays more expensive because of the PM. They are also more sensitive to high temperatures and mechanical vibrations, since the PM can be partially or fully demagnetized with the increase of temperature or as a result of crack formation, which also leads to decreasing the available motor power and a unbalanced magnetomotive force.

On the other hand, electric motors using PM made by rare earth materials as NdFeB are still currently the most appropriate ones for high performance electric cars as they have higher torque/weight and power/weight ratios. They also have faster dynamics and are normally more energy efficient.

Furthermore, this type of motor does not present some of the disadvantages of others types, namely [5]:

- brush wear and the high inertia moment, typical of the DC motors;
- Joule losses on the rotor bars, decreasing the efficiency and requiring higher refrigeration power;

- higher weight and volume, typical of induction motors, for the same power;
- higher electrical and mechanical time constants.

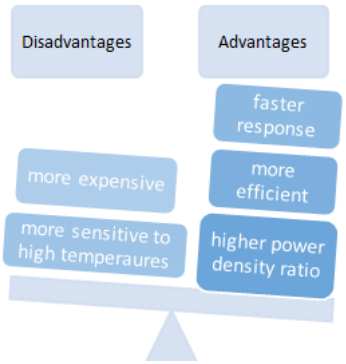

Figure 2.4: Main advantages and disadvantages of PM synchronous motors.

2.6 Synchronous machine overview

Synchronous machines rotate with a velocity proportional to the frequency of the current in the armature, under steady-state conditions. In other words, the rotating magnetic field produced by the armature currents is synchronous with the magnetic field on the rotor. This magnetic field on the rotor can be produced either by PM or windings [6]. The first one is known as PMSM, the second one, where the field on the rotor is produced by windings, is known as Salient-Pole Synchronous Machines (SPSM).

The SPSM have the advantage of enabling the adjustment of the rotor field, increasing the efficiency at higher velocities [7]. However, this topology needs a DC source to supply the rotor coils and slip rigs responsible for connecting the source to the coils, increasing the project complexity. The slip rigs do not reverse the current as the commutator in a DC machine, maintaining the north and south poles static. As one goal of the project is to reduce the complexity at the beginning to decrease the risks of not having a functional prototype, this topology will be discarded.

There are two main forces responsible for rotating the rotor. The Lorentz force and the reluctance force. The Lorentz force is a combination of both magnetic and electric forces. The principle says that a particle of charge moving with a velocity in the presence of an electric and magnetic field is subjected to a force. A variation of this principle is known as Laplace force and specifies the magnetic force produced by a current flowing through a wire. In other words, one can say that whenever a current is flowing through the windings of the stator, it has created an electromagnet by the creation of a magnetic field. This magnetic field rotates according to the current flowing from one coil to another over time. The magnetic field produced in the rotor by the PM is attracted to the rotating magnetic field of the stator, producing a rotation of the rotor [8].

The reluctance force is created between the blocks of iron and the PM or electromagnets, contributing also to the rotor rotation. So it is possible to see that the rotating magnetic field of the stator attracts both the PM and the iron rotor. These forces are normally equally strong, depending on the design, and

work together increasing with the angle between the stator field and the rotor field. A maximum value is obtained at 90 degrees between both, in case of a machine with 1 pair of poles. This is how the machine creates mechanical power. [7]

Figure 2.5 shows the ideal power, induced voltage and torque of a synchronous motor. It is possible to see that the torque value is constant from zero speed to the base speed. At this speed, the Back Electromotive Force Voltage (BEMF), induced in the stator coils by the rotation of the rotor, is the same as the voltage being fed to the motor. At that moment, there is no current flowing through the motor and it is only possible to increase the speed by decreasing the rotor magnetic field; this method will be presented further and it is known as field-weakening. At the base speed, the power value is maximum, being constant for higher speeds as the torque value decreases.

The torque value is limited by thermal phenomena as higher torques require higher currents and higher losses are produced. The speed value is limited by the feeding voltage and the BEMF characteristic of the motor. The motor design will take these parameters highly into account, as they limit the performance of the machine.

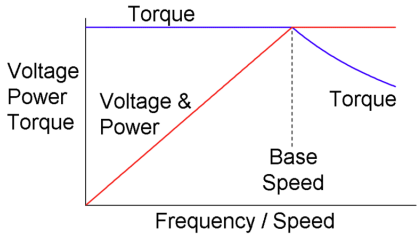

Figure 2.5: Ideal characteristic of a synchronous motor: Blue - Torque curve, Red - Voltage and Power curves [9].

The differences between peak torque and nominal torque (and power, as these parameters are proportional when the speed is the same) are dependent on the motor thermal characteristics. Peak torque is the torque value the motor can withstand during short periods of time (defined by the manufacturer) without reaching the temperature limit of the materials (normally limited by the windings insulation). Nominal torque is the value at which the motor can work when the thermal stabilization is reached. The maximum torque values, as described earlier, decrease for speeds higher than the base speed, due to field-weakening, to maintain the output power.

2.6.1 Rotor Geometry

In PMSM, the PM can be arranged in many different ways. Machines with the two main following configurations shown in Figure 2.6 are commonly used: on the left the Surface Mounted Permanent Magnet (SMPM) machines and on the right the Interior Permanent Magnet (IPM) machines [10].

The SMPM machine is the classic non-salient pole. Despite of its simplicity and lower construction cost compared to other Brushless Permanent Magnet (BPM) machines, the PM are very exposed to demagnetization fields and internal heat produced by Joule losses, as they are on the rotor surface and thus in the magnetic air-gap. Furthermore, the PM are subjected to centrifugal forces, that can cause

their detachment from the rotor, usually requiring a carbon strap that will increase the motor's magnetic air-gap.

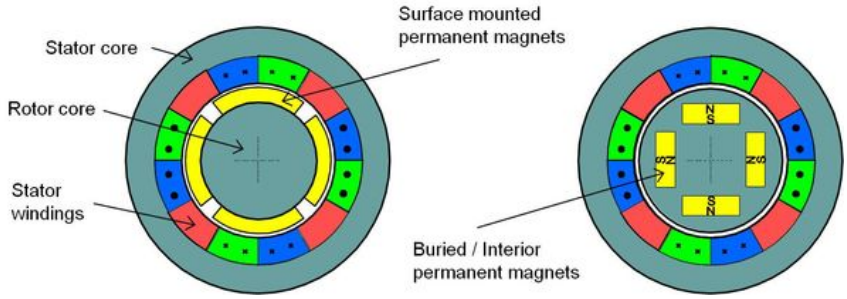

Figure 2.6: Rotor surface mounted permanent magnet topology (left) and the interior rotor permanent magnets topology(right) [11].

The general advantages of IPM machines is the possibility to concentrate the magnetic flux generated by the PM in the rotor and thus achieving higher air gap flux densities, which is important for increasing the motor electromagnetic torque. Moreover, the PM are well protected against demagnetization and mechanical vibrations.

Taking into account the manufacturing, financial and time limitations for this project within the FST team, a topology that allowed manufacturing and assembling using conventional machining (including waterjet or laser-cutting) had to be chosen. Furthermore, a topology where the PM are mounted before having a magnetic remanent field (requiring subsequent magnetization), was not an option, as it would not be possible in the time available. Solutions were the PM must be made according to specific dimensions, where moulds are required, are out of this scope due to high costs.

The *spoke* topology (Figure 3.6) met all the requirements stated. Using rectangular PM, it was easier (and cheaper) to order standard ones. Furthermore, it was a significant opportunity to optimize the geometry as a lot of different dimensions were possible. In this topology, the air-gap flux density increases due to the flux concentration principle. Two magnetic poles with the same density pointing each other will produce a magnetic flux through the air-gap composed by the sum of both (if the magnetic permeability of the shaft is near zero). Also, the magnet surface area is greater than the rotor surface area, contributing to an increase in the flux concentration and torque production.

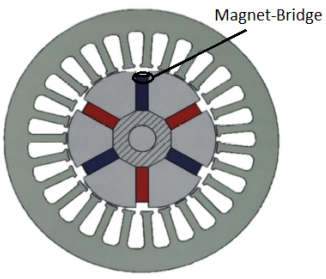

Figure 2.7: *Spoke* motor topology [12].

Magnets-bridges must be avoided to prevent the flux from moving inside the rotor from one magnet pole to the other, decreasing the air-gap flux and torque generation. Furthermore, the shaft must be

made of a non-ferromagnetic material to prevent a large portion of flux generated by the PM to leak through it.

2.7 Motor Materials

The final mechanical output power of the motor can be limited by three factors: i) saturation of the magnetic field, which limits torque, ii) mechanical quality of the project and iii) materials that limit velocity and motor temperature.

The saturation of the magnetic core depends highly on the geometry and on the material selected. According to the geometry, optimization algorithms can be used to assist within the design phase to avoid areas where the saturation can appear. Concerning the materials, their specifications are different according to the place and to function that they have in the motor. The materials will be divided according to the following: the core material, the PM, the shaft, the housing and motor windings and, finally, the insulation.

Regarding the speed limit, the goal was to achieve a mechanical project of the shaft and of the rotor in a way that the materials can withstand high centrifugal forces.

Finally, the motor temperature is highly influenced by the production of heat coming from the different types of losses in the motor and of the capability of the cooling system to remove this heat. The cooling system was developed in a previous master's thesis [13]. Concerning the temperature, the capability of the PM and copper windings to withstand higher values of this parameter is also a crucial factor. In fact, the higher the temperature they can resist (and for a longer period of time), the higher will be the peak and continuous torque (without saturation) and power. One can say that the peak and continuous power and torque values are highly dependent on the motor thermal behavior.

2.7.1 Core material

The core material that composes the rotor and stator can be defined as a key part of all the magnetic systems. These are known as soft magnetic materials: they do not retain the magnetic field but are easy to magnetize and demagnetize. They also present a low remanent magnetization, a small area enclosed by the hysteresis loop (low losses), low coercivity and high initial permeability. Some of the most important parameters to take into account when selecting the material for the core are the saturation point, the permeability, the specific losses and the density. The first two characteristics have high influence in the maximum torque the motor is capable of generating; the third influences the overall efficiency of the motor as well as the motor heat and the density, since the core is the motor part that has more volume and hence has the higher influence on the motor final weight [14].

The core material is divided into sheets that are stacked together. The thickness of the sheets is also a very important parameter: the thinner they are, the lower will be the Foucault losses. This happens because the quadrature currents (axis z) produced by the magnetic flux density moving in axis x-y will face a higher resistive path as thinner the magnetic sheets are, decreasing the current amplitude and

Table 2.1: Properties of the materials for the motor core.

	M250-50A	NO20	Hiperco50
Magnetic Saturation [T]	1.8	1.8	2.4
End of linear zone [T]	1.2-1.5	1.2-1.5	1.9-2.1
Losses at 50 Hz with 1T [W/Kg]	1.07	1.09	1.01
Losses at 400 Hz with 1.4T [W/Kg]	24.1	12.3	11.0
Ultimate Tensile Strength [MPa]	585	505	814
Density [Kg/m^3]	7600	7650	8 110

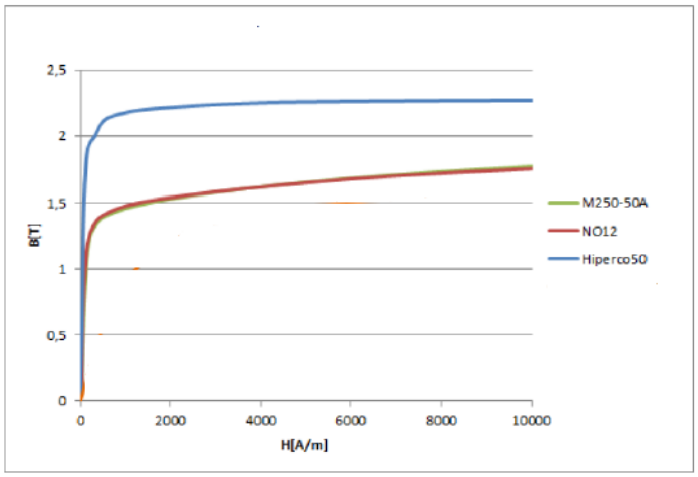

Figure 2.8: B-H graph for different core materials - M250-50A (green), NO12 (red) and Hiperco 50 (blue) [14].

losses.

The most important materials properties are shown in Table 2.1.

The higher magnetic saturation value of the Hiperco, when compared to the other materials, is evident. Iron-cobalt alloys were invented in 1912 by Weiss, suffering some chemical changes until Wahl added to the composition vanadium, in 1932, to make it easier to cold work [15]. The process of manufacturing was very expensive, and the applications where it was used were few. During the early 70s, National Aeronautics and Space Administration (NASA) started to use it to perform some tests regarding the development of magnetic materials capable of operating in very high temperatures ranges [16]. In the beginning of the millennium, with the introduction of Cobalt production, the price of Hiperco decreased and it became possible for use it in more common applications, including high power/weight electric motors. Nevertheless, despite being cheaper, the price can be volatile, increasing to up to 200 EUR per Kilogram.

Figure 2.8 shows the comparison between BH curves of M250-50A, NO12 and Hiperco 50. Notice that the B-H graph of NO12 is the same as the one of the material being analysed, NO20, because their compositions are identical. The only difference is the thickness, which increases from 0.12 mm to 0.20 mm.

Analysing Table 2.1 and Figure 2.8 it is clear the evidence of the advantages of using Hiperco. With the increment of the magnetic saturation value it is possible to improve the power and torque up to 30 % [17].

2.7.2 Permanent Magnets (PM)

The PM belong to the materials classified as hard magnetic materials. In contrary to the soft magnetic materials shown before, these materials are capable of retaining their magnetism, being difficult to demagnetize, even when they are removed from the applied magnetic field. They have high remanent magnetization, large hysteresis loop which represent higher losses, low permeability and high coercivity. Furthermore, they also have high magnetic energy stored [14].

By having high losses (hysteresis loop and Eddy current) and low capability to withstand high temperatures without losing their magnetic properties (Curie temperature) - the selection of the PM is crucial. Moreover, it is very difficult to remove heat from the rotor, as it is separated by the air-gap (which works as a thermal resistance). A list of the most relevant parameters of PM suitable for this kind of application is show in Table 2.2 [18] and [19]. Notice that although Curie temperature is highly related to maximum working temperature, they are not the same. The first one is the temperature at which the PM loose all the capability to be magnetized, the second one is the temperature at which the PM begins to lose its strength if heated continuously [20].

Table 2.2: Properties of the materials for the PM.

	Alnico	SmCo	NdFeB
Remanence [T]	0.6-1.4	0.9-1.15	1-1.4
Coercivity [kA/m]	275	450-1300	750-2000
Energy product $(BH)_{max}$ [kJ/m^3]	10-88	150-240	200-440
Maximum Curie Temperature [$^\circ$C]	700-860	800	310-400
Saturation H [kA/m]	280	$>$3200	$>$2400
Density [Kg/m3]	7300	8200	7400

The defined magnet material for this motor was the Neodymium Iron Boron (NdFeB). This rare-earth material provides the best design properties as it has a higher energetic product and remanent magnetic field. As a disadvantage it does have a low Curie temperature when compare with the one most frequently used samarium cobalt (SmCo).

2.7.3 Shaft material

The shaft is probably the most complex mechanical part in the motor design. This component must be capable of withstanding the very high centrifugal forces produced by the rotor rotating at speeds as high as 20 000 RPM. To prevent failure in case of an overspeed fault, a speed interval must be set between the maximum motor speed (12 000 RPM) in normal working conditions and burst motor speed in faulty conditions (20 000 RPM). Furthermore, the shaft material, in the case of *Spoke* geometry, must be a non-ferromagnetic material as pointed out before [12]. Additionally, it has also to withstand the forces produced by the generation of the motor torque as the shaft is responsible for transmitting the torque (and power) to the load. So, a non-magnetic material with high tensile strength and low losses was chosen.

Table 2.3 shows the properties of the non-magnetic materials suitable for a shaft in this application.

Table 2.3: Properties of the materials for the shaft [21]

	Aluminium 7075	Stainless steel AISI 316	Titanium Grade 5
Density [Kg/m^3]	2810	8000	4430
Yield Tensile Strength [MPa]	503	290	880
Ultimate Tensile Strength [MPa]	572	580	950
Electrical Resistivity [$\mu\Omega$.cm]	5.15	75	178
Thermal Conductivity [W/(m.K)]	130	16.2	6.7
Magnetic Relative Permeability	1.000022	1.0008	1.00005

From Table 2.3 it is possible to conclude that selecting a material is not an easy task, as a lot of trade-offs must accepted. Regarding the strength of the materials, titanium is the one that can withstand higher forces, but it has a very low thermal conductivity and is very expensive. Regarding Aluminum, it has low density, and high thermal conductivity but a lower electrical resistivity than Stainless Steel, which means that it is more vulnerable to temperature increase due to induced currents.

Ultimately, the material selected was stainless steel, as it has high electrical resistivity and an higher ultimate tensile strength than aluminum, allowing it to withstand higher forces.

2.7.4 Housing material

The motor housing is composed of covers/jackets responsible for guaranteeing the motor structure as well as to protect the motor components against the ingress of undesirable materials, such as dust or water [4]. It is important that the motor jacket has high thermal conductivity, as most of the motor heat will be removed through it, but it also must be non-ferromagnetic to reduce the losses during the time the motor is working with high saturation and some magnetic flux escapes from the stator. It also needs to be made out of a lightweight material, as it is a large piece, and to have considerable structural strength to withstand the forces generated on the motor attachments. Finally, it must have an high corrosion resistance and be easier to machine.

The material selected that met all the written requirements and was available in quantity to manufacture the motor housings was Aluminum 7075-T6.

2.7.5 Motor windings and insulation

The windings are responsible for conducting the current that is fed to the motor. So, the most important parameter is the electrical conductivity that must be high to reduce Joule Losses. Working temperatures and tarnish ability must also be considered as this will be the part working at higher temperatures and its shape must be changed to fit in the stator slots. The wire diameter is a parameter to be considered as it has high influence in the motor costs through tarnish ability and man-hours and also in the winding fill factor, as shorter diameters lead to less air between the wires.

Two most common materials, copper and aluminum, are considered in the Table 2.4. Silver is also suitable for this kind of applications, but due to the high cost it was not considered [22].

As it is possible to see in Table 2.4, the copper has less resistivity, which means that, for the same value of conductance, the aluminum requires higher cross-section. Although, weight is a very impor-

Table 2.4: Properties of the materials for the windings.

	Copper	Aluminum
Resistivity (wire) [$\mu\Omega$.cm]	1.72	2.83
Temperature coefficient of resitivity [ppm/K]	4027	4308
Thermal conductivity [W(m.K)]	398	210
Density [kg/m^3]	8920	2700

tant parameter and the weight reduction using aluminum is considerable, in this application, the area available for the windings is reduced and the heat production must be kept as low as possible which makes this solution unfeasible. Furthermore, it is important to say that aluminum oxidizes much faster than others metals, requiring special care when making the connections, terminals and soldering of the motor phases.

The windings are coated with insulation materials to prevent the formation of electrical short circuits when they are in contact with each other. This coatings/enamels are chosen mainly according to the motor working voltages, currents and temperatures [23].

Additionally, where there is a difference of electrical potential between two electric conductors, there must exist an electrical insulation material. For example, in electrical motors, between the windings and the stator there should be a material, normally insulation paper to prevent the current of escaping through the stator and housing that is grounded. This paper, in order to have high electrical resistance, normally also has low thermal conductivity that prevents the windings heat of being dissipated through the stator and the cooling system. Therefore, there should be a compromise between electrical resistance and thermal conductivity. The insulation of the windings (the windings being the component of the motor that normally heats more and are the first to overheat when a peak torque is produced during long periods of time) required special consideration, as they are exposed to damage due to thermal and mechanical (and also electrical but less aggressive) stresses. This limits the peak power and torque of the motor. This happens because during the peak of torque production, the majority of the heat is produced in the windings and it takes time to reach the rotor, not affecting in such short time the other significant part of the motor to high temperature, the PM.

Figure 2.9 shows the influence of the windings temperature to the insulation lifespan, according to the insulation class. It can be seen and stated in [4] that each 10 ^{o}C rising above the rating temperature, the motor lifetime decreases by half.

In the FST team, the cars and its more critical pieces are designed to withstand 300 working hours, this is beyond the maximum time a car will do in its life. The motor temperature can be increased on purpose, in this way the motor can work at its best performance inside the 300 hours range. A study of this process was not analysed in this work, although it is highly recommended for the future work within this project.

Nowadays, new materials having high electrical resistance and high thermal conductivity are being developed and used mainly in electronics to be inserted between power transistors or processors and heat sinks. The application in electric motors is yet to be made, but can be a good solution for the future.

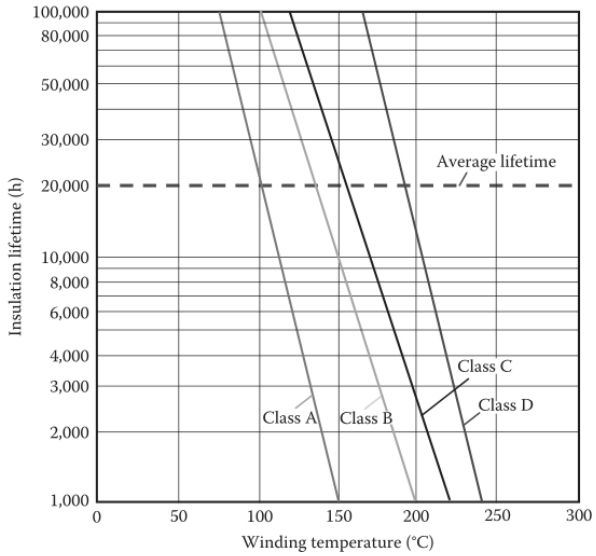

Figure 2.9: Influence of temperature in the lifespan of the windings insulation [4].

Annealed copper wire AWG 26 with a H class of isolation, holding up to 180°C was selected for the MJF prototype motor.

2.8 Processes of electric motor manufacturing

The manufacturing process of electric motors requires processes to cut the magnetic steel sheets to the required design and stacking them to assemble all the different sheets in one piece, forming the stator and the rotor. In each of these, the final result can be obtained using different types of technologies which have different advantages and disadvantages. They will be presented on the next sub-chapters.

2.8.1 Cutting Processes

Cutting technologies are necessary to manufacture both the stator and the rotor parts of the FST 08e prototype motor.

The cutting processes involving the non-oriented electrical sheets of the electric machines have an impact on their overall efficiency. The machining stress caused on the electrical steel increases the iron losses. A treatment called Stress Relief Annealing (SRA) can be made in order to relieve the strain and stress of the material, recovering their magnetic properties and improving the efficiency of the machine [24].

The most common cutting technologies are punching, laser cutting and Wire Electric Discharge Machining (WEDM). Other methods involve the use of technologies such as guillotine, water-jet cutting, wire electric discharge machining or photo corrosion. Figure 2.10 shows the influence of the different cutting processes on the B-H and permeability characteristics of the electric steel. It is also possible to notice that the materials characteristics are almost reestablished after the SRA treatment. These experiments were conducted in a 35W270 high-grade non-oriented electrical steel sheets.

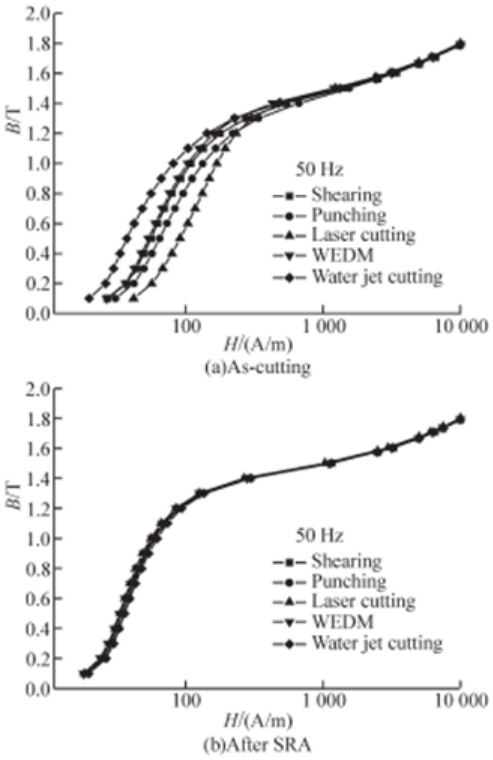

(a) Different cutting process B-H graph a) before SRA; b) after SRA

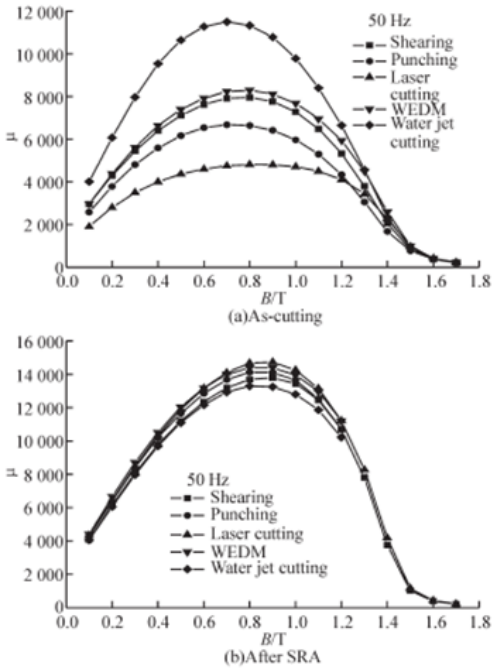

(b) Different cutting process permeability graph a) before SRA; b) after SRA

Figure 2.10: Influence of cutting processes on magnetic material properties [24].

In fact, the best magnetic properties are obtained through mechanical cutting techniques. However, as just one prototype was to be initially manufactured by the FST team, those techniques were excluded as the cost of moulds is very high. So the cutting techniques analysed within this work were laser cutting and water-jet cutting.

Laser cutting causes a thermal effect in the area near the cut. This thermal effect leads to changes on the material microstructure that decrease its magnetic properties as the material magnetic permeability and also increases its coercive field and the total material Joule losses. In the other hand, laser cutting does not create shearing deformation at cutting edges, does not generate burr and, with a SRA, increases the magnetic properties of the material, as shown in Figure 2.10 [25].

Water-jet cutting has less precision on the cut and creates small mechanical deformations [26]. The advantage of this technology is that it has low influence on the deterioration of the magnetic properties because it does not create thermal stresses or plastic deformation. This technology also presents the lowest total material losses in the cutting area and, additionally, does not need annealed treatment that would certainly increase the final cost. Bearing in mind these enunciated advantages, this technology was the first one selected to manufacture the stator and the rotor of the FST 08e motor prototype. Nevertheless, another technology, laser cutting, was adopted as in reality it was the only one available on the manufacturer.

2.8.2 Stacking processes

A stator stack is formed by stacking silicon steel laminations into one piece. Therefore, clamping technologies were analysed as they were necessary to manufacture the stator of the FST08e prototype motor. The stacking processes influence the overall motor efficiency as they contribute for the iron losses and the mechanical structure of the rotor and stator.

There are several technologies to assemble stack laminations into cores. These are presented, as well as their main advantages and disadvantages, as follows [4]:

1. **Welding** (Figure 2.11)— Welding is the most common. It consists, as the name suggests, in welding all the sheets together. To do so, a slot normally on the stator outer face is made to facilitate the welding of the sheets without increasing the stator diameter. This method increases the stator and rotor iron losses, as it promotes the contact with the different sheets, decreasing their resistance and increasing the Eddy currents. It can also increase the motor cogging torque in case of improper design.

Figure 2.11: Stator welding as a stacking method [4].

2. **Bonding with adhesive materials**— In this method, a thin film of adhesive material is placed on the lamination surfaces. It is more common to order the electric steel sheets with this coating material already placed. The stack is subjected to pressure and to heat cycles to cure the adhesive material. A mould is normally necessary. In this process, the efficiency is improved as it does not increase Eddy currents. On the other hand, this method provides low mechanical strength of the stack.

3. **Riveting/Bolting**— This method is very economical and easy to do. It consists in holding all the sheets with a rivet or bolt which creates an axial compression between them. However, the heads of the rivets and bolts obstruct the stator end windings. To prevent this, instead of rivets or bolts, it is possible to use pins.

4. **Self-cleating** (Figure 2.12)— This method is very common. It consists in placing V-shaped strips in specific dovetail slots and then flattening them at the outer diameter face of the stator or rotor laminations.

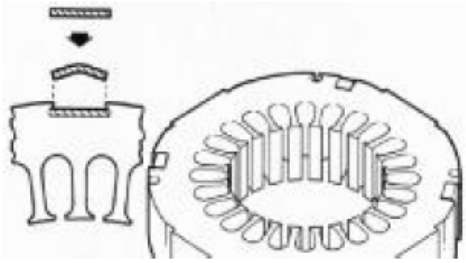

Figure 2.12: Self-cleating schematic [4].

5. **Using thin sleeves** — This method is used in machines that need to withstand large forces as the sleeves, normally made from metal, have high strength. Losses due to induced currents must be studied and taken into account as they highly influence the motor efficiency.

After analysing the advantages and disadvantages of the different clamping technologies, the FST 08e stator stack prototype was assembled by bonding laminations with adhesive materials.

2.9 Electric motor control

The AC motors integrated in powertrains of electric vehicles are fed by inverters. These components are normally also responsible for controlling the motors. This control is made by modulating the current waveform feeding the motors. Nowadays, in road electric vehicles, there are numerous algorithms defining the way the current waveform is modulated, according to the specifications and requirements of each application. For instance, the current waveform can be modulated to decrease the noise, to increase the system efficiency, or to increase performance or even lifespan. It is a state of the art subject, being developed by universities and automotive companies.

In FS, the larger teams, with high budgets and sponsorships, are doing this as they are also developing their own inverter and motor controller systems. Like the development of motor for the specific application in a FS car, the development of a motor controller system has many benefits. The team started this project this current year.

Regarding motor control, as the motor must be designed taking into account the inputs of the inverter/motor controller, a brief explanation will be made. The design of the electric motor must be a closed loop between the inputs of the inverters going to the motor and the outputs of the motor going to the inverter. This happens as the waveform created by the inverter suffers modifications depending on the motor state.

A vector control of the three-phase AC Machines was considered using maximum torque per ampere methods. Evidence suggests this method used by the team works for the inverter. In this method, the current responsible of producing torque is always the maximum to a set-point of torque and the angle between the rotor magnetic field and the rotating field produced by the stator is always the angle that

maximizes torque. This means that the current amplitude is proportional to the motor torque if no saturation occurs [27].

The three phase sinusoidal waves are summarized for complex vectors which are represented in the Cartesian coordinate system. A current vector $\mathbf{i}_s(t)$ (Equation 2.1) that can be defined as the resultant current circulating in the stator with a frequency of f_s, can be defined as a combination of the three stator currents [28]:

$$\mathbf{i}_s = \frac{2}{3}.[i_{su}(t) + i_{sv}(t).e^{j\gamma} + i_{sw}(t).e^{j2\gamma}], \gamma = 2\pi/3 \tag{2.1}$$

Following the logic, the complex vectors of stator and rotor voltages and flux are obtained respectively $\mathbf{u}_s$, $\mathbf{u}_r$, $\boldsymbol{\psi}_s$ and $\boldsymbol{\psi}_r$.

Lets consider now a new Cartesian coordinate system with named dq axis that is rotating synchronously with the vector defined above and define the vectors relatively to this new coordinates (Equation 2.2):

$$\mathbf{i}_s = i_{sd} + ji_{sq} \tag{2.2}$$

All the others vectors follow the same logic.

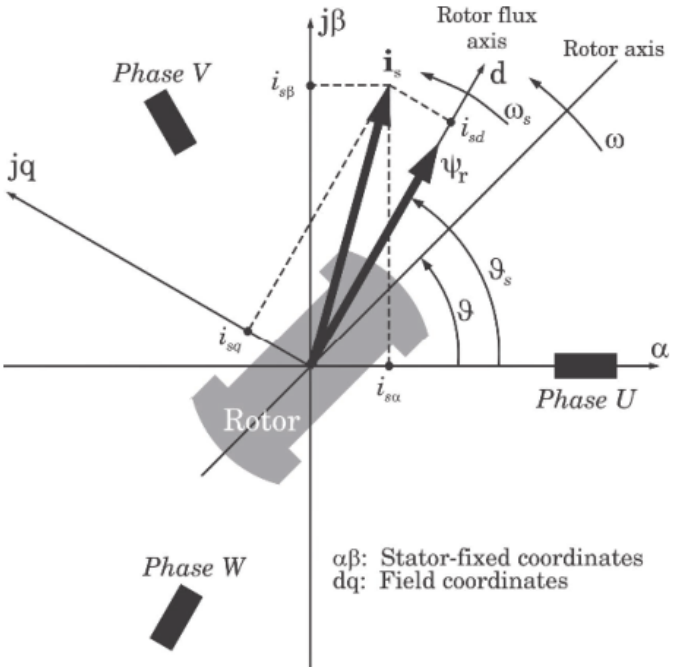

Figure 2.13: Control vectors relative to stator and field (rotor) coordinates [28].

Figure 2.13 represents the stator and field coordinate systems relatively to the vectors introduced above in induction machines. In case of PMSM, the rotor flux axis is aligned with the rotor axis and with real axis *d*, so the quadrature component *q* of the flux is null $\psi_r = \psi_{rd}$. This means that in PMSM, the torque (T) is created in almost all cases by the component referent to axis *d* (in more complex algorithms and in the case of field weakening, the quadrature component is not null). Equation 2.3

shows the relations for this case, where n_{pp} represents the number of pair poles. Notice that in PMSM ψ_r is constant, so torque can be controlled only by i_{sq}.

$$T_e = \frac{3}{2}.n_{pp}.\psi_r.i_{sq} \tag{2.3}$$

After, a new Cartesian coordinate system $\alpha\beta$, where the real axis *d* is the same as one of the three phases, a stator-fixed coordinate system come, and a transformation of three winding system to two winding can be described as Equation 2.4.

$$\begin{cases} i_{s\alpha} = i_{su} \\ i_{s\beta} = \frac{1}{\sqrt{(3)}}.(i_{su} + 2i_{sv}) \end{cases} \tag{2.4}$$

$i_{s\alpha}$ is zero because of the open neutral-point of the motor. The difference of Cartesian coordinate system dq and $\alpha\beta$ is that the first one rotates with the angular speed of the rotor $w_s = d\theta_s/dt$ and the second one is fixed.

Figure 2.14 represents the measurement of the currents to be used by different control algorithms that will not be further analysed under the scope of this thesis.

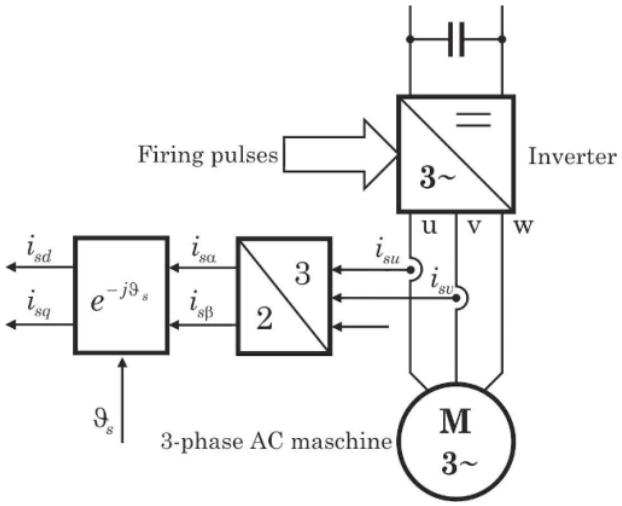

Figure 2.14: Acquisition of the field synchronous current components [28]

It is possible to verify that with the uncoupling into two vectors, i_d and i_q, it is also possible to separate the control of flux field current and the torque current. This makes the utilization of the PMSM possible in more working ranges and with different behaviors, equivalent to the simpler way of how DC motors are controlled. Knowing the exact position of the rotor, the motor controller defines the firing pulses of the IGBTs current feeding the motor and consequently creating a rotation of the rotor. Defining the amplitude and frequency of the signal feeding the motor, parameters as speed and torque (and power) change.

Further research will be not conducted as this is out of the scope of this thesis but, before finishing this subject, one last operation of control must be analysed which is crucial in a high performance PMSM rotating at elevated speeds: field-weakening.

In this, a negative current i_d is fed to reduce the field strength. With this, the BEMF reduces and, as a consequence, the current flowing through the windings increases, rising the speed even more. Consequently, from the moment the motor enters the field-weakening velocity, the torque will continuously decrease to zero with the velocity increment. Also, working in this area for long periods of time can damage the PM, as their magnetic field is being subject to another field generated in the opposite direction.

2.10 Derating Strategies

Derating is a protection control method where performance of the electric machine decreases when it is working under fault conditions (outside the normal working operation limits) to prevent major failures. It is made at the inverter software level and it limits the currents and voltage values feeding the motor in case of an overtemperature, overspeed or overvoltage on the motor. Using this method it is possible to gradually decrease the machine performance without a sudden stop. Furthermore, as some derating strategies have a loop impact on the motor fault conditions, it is possible that when applying it, the machine returns to a normal working condition without the need of a stop. In the case of temperature derating strategy, a non-linear optimal control of the output availability of torque with temperature profile can be developed to assure that the machine can decrease its temperature without losing too much performance. This strategy was suggested as a subject for another work.

Chapter 3

Motor design

3.1 Introduction

This chapter presents the analysis carried out to define the initial design parameters of the prototype electric motor for the FST 08e car. The mechanical and the electromagnetic analyses as well as the Genetic Algorithm (GA) used to optimize the requirements, are presented. There is special emphasis regarding the slots and the tooth lips of the stator as well as the shaft and the core design. Figure 3.1 summarizes the design process used in this work.

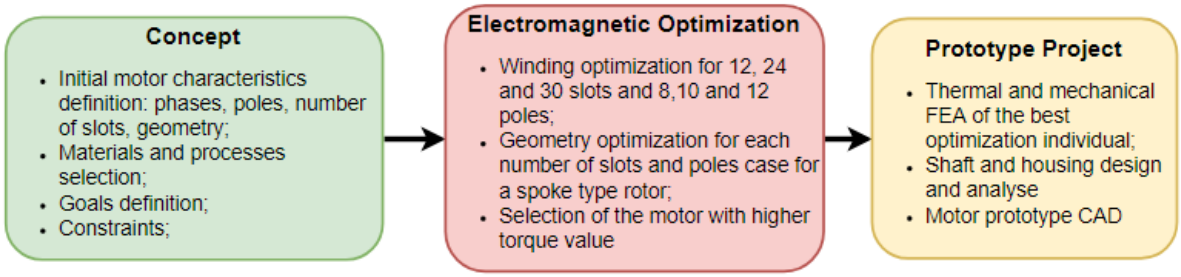

Figure 3.1: Design process of the MJF prototype motor.

3.2 Motor design parameters

The requirements of the electric motor prototype were decided taking into account the characteristics of some of the racing circuits of the FS competitions. In these competitions, the cars need to have a high acceleration, as the overall tracks of those racing circuits have many more curves than straight lines. The racing cars also need to be able to perform those curves at the highest possible velocity, which is assured by increasing the traction to the ground. To achieve these goals, the weight of the car is a crucial parameter. Also beneficial is the use of four electric motors, one in each wheel, which allows the independent control of each motor and thus increasing the car traction. Besides, the competitions have a very demanding regulation that limits some parameters. For example, the maximum power of the car is limited to 80 kW.

Having those conditions in mind, the FST Lisboa team decided, as a starting condition, that the FST 08e car will have four electric motors. Furthermore, it was decided that each one of them will be fixed on the wheels suspension system, so requiring a more limited volume and weight. The voltage and current values feeding the motors are imposed by the inverters.

Succeeding this, the main design challenge was to define a compact motor solution for the four electric motors, which would assure the adaptability and stability of the car, not conditioning its dynamics. To optimize the performance, the following specific goals were also taken into account:

- to maximize the torque;
- to minimize, as much as possible, the weight.

The approach to establish the initial design parameters consisted in performing a set of vehicle simulations, considering the racing circuits of some of the FS dynamic events. Figure 3.2 presents one of the simulations carried out for the racing circuit of Barcelona, as well as the results obtained in what concerns the electric power and the engine torque.

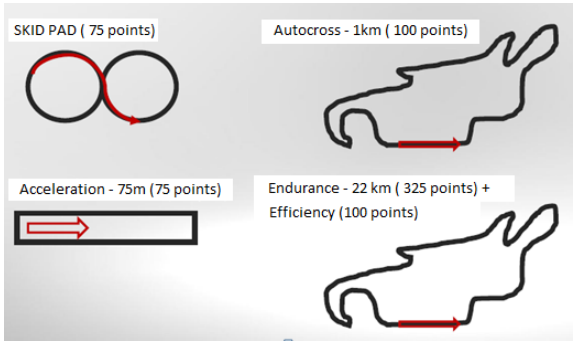

(a) Dynamic events of Formula Student competitions

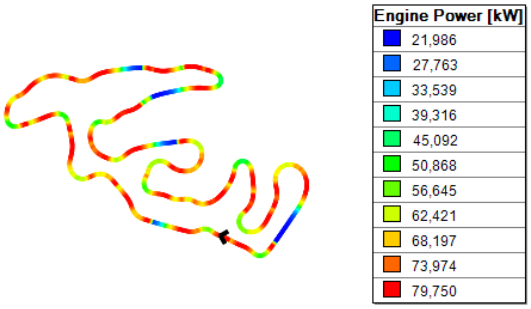

(b) Formula Student track power simulation

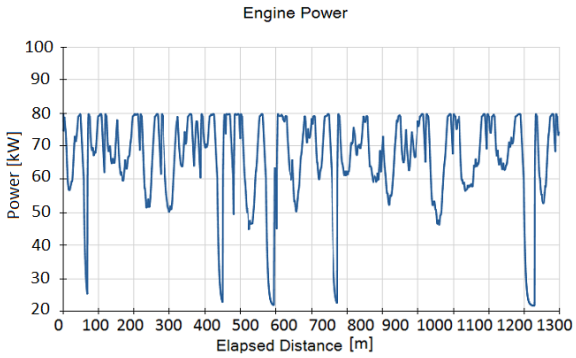

(c) Electric power during the track time

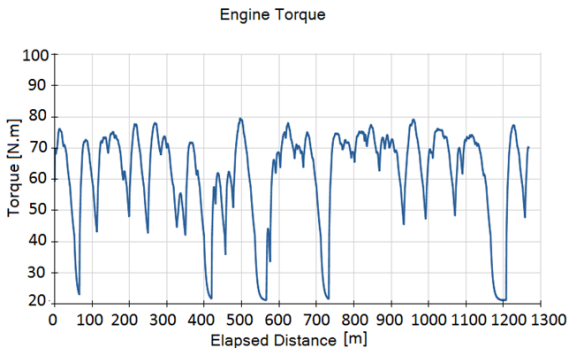

(d) Torque during the track time

Figure 3.2: Dynamic parameters simulation over the Barcelona FS track using Optimum Lap Software.

An analysis of the results of the different simulations, namely in what concerns the cars performance, was undertaken. To minimize the risks of not having a fully manufactured and tested version of the motor ready to compete, some parameters as the external attachments (mounting points) of the motor and its volume, were kept equal to the commercial AMK motors that could be used instead; information about this system is presented in Appendix A. This is an option to reduce the associated risks of manufacturing using a new system to compete for the first time. If something goes wrong during the delivery of the MJF

motor or some major failure is detected after the critical period that would compromise the competitions, the AMK motors will replace the MJF motors. In the end, the design parameters of the motor also took this into account, constraining the project in some aspects.

This analysis, together with a cost-benefit evaluation, allowed the definition of the requirements for the electric motors prototype version (Table 3.1). This prototype will be improved in a next version to integrate the FST 08e car.

Table 3.1: Requirements of the motor prototype.

Parameter	Value
Maximum Power	20 kW
Maximum Torque	20 Nm
Maximum Weight	5 kg
Maximum Speed	12 000 RPM
Transmission Relation	1:15
Maximum Voltage	380 Vac
Maximum Current	100 A
Phases	3
Cost per motor	2000 EUR

3.3 Winding Optimization

An algorithm was used independently to optimize the windings layout. The method consists in combining a generalized harmonic winding analysis together with a genetic multi-objective optimization algorithm. The algorithm receives as inputs the following design variables: i) number of stator slots, ii) number of poles, iii) number of phases, and iv) single or double layer winding. Using an optimization algorithm, a solution (or solutions) of winding arrangements is provided [29].

The fitness function of the multi-objective optimization for this case has as objectives: i) to maximize the fundamental magnetomotive force (mmf) per ampere (current), ii) to minimize the sum of harmonic mmf/amp, and iii) to make a balanced winding.

The mmf is the sum or net total field intensity that moves flux through a material [19]. It has high impact on the motor torque production as it defines the quantity of flux moving between the rotor and the stator. The mmf is highly dependent of the winding arrangement and effective air-gap length.

The harmonics included in the mmf are an undesired consequence of the magnetic interaction of the phase windings that in addition to decreasing motor efficiency, create vibration on the motor that can lead to a decrease of the lifespan. This action can be mitigated by minimizing the sum of the harmonics. The higher the number of slots per pole per phase, the more sinusoidal the final mmf will be, and consequently, the motor will present a lower torque ripple and higher efficiency since it will have low harmonics content [29].

The called balancing winding condition is related to the fluidity that the rotating air-gap magnetic waves move, without producing “forwards” and “backwards” forces on the rotor.

Only stators having 12, 24 and 30 slots were considered in order to reduce the computation time. As the number of poles that meet the velocity requirement for the motor are 8, 10 or 12, the three

values selected for the number of slots fit better with the number of poles as they show higher winding factors (the ratio of flux linked by an actual winding to flux that would have been linked by a fully-pitched concentrated winding with the same number of turns) and thus increase the final mmf. Furthermore, with a combination of slots per pole superior to 3 it is possible to manipulate the winding factors, in order to maximize the first harmonic and eliminate the others [12]. All slots were considered having in mind that only a single layer winding will be used.

Simulations were carried out to determine the best configuration for the winding. The results are shown in Table 3.2.

Table 3.2: Motor winding layout results.

Study	Fundamental	Sum Harmonics	Balanced
12 slots / 6 poles	0.574	1.79	Yes
12 slots / 8 poles	0.414	1.169	Yes
12 slots / 10 poles	0.369	2.137	No
24 slots / 6 poles	0.979	2.512	Yes
24 slots / 8 poles	0.956	0.414	Yes
24 slots / 10 poles	0.732	2.394	Yes
30 slots / 6 poles	1.501	2.630	No
30 slots / 8 poles	1.12	3.576	No
30 slots / 10 poles	0.902	2.097	No

Taking the previous into account, the number of slots that maximize the fundamental winding factor was found to be 30 (with 6 poles), once it has the highest fundamental mmf per amp. However, it has high sum of harmonics, which will increase the heat production and do not has a balanced condition. Winding with 24 slots and 8 poles with 0.956 fundamental mmf per amp, 0,414 sum of harmonics and balanced condition was the selected, one as it has the best commitment between the fundamental mmf and harmonic losses and has balanced condition. The adopted winding configuration is shown in Figure 3.3.

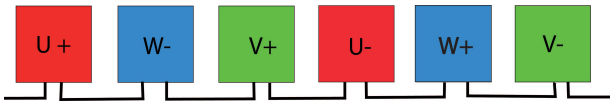

Figure 3.3: Winding configuration.

In Figure 3.4, the associated harmonics of this winding layout are presented. The harmonics only present odd numbers due to the fact of being an integer slot winding, where the number of stator slots is equal to the number of phases multiplied by the number of rotor poles.

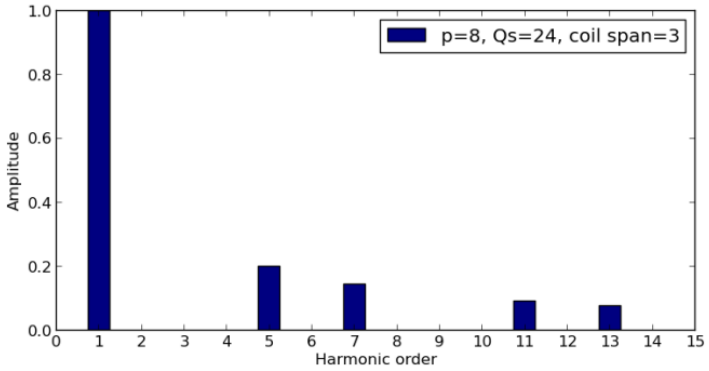

Figure 3.4: Amplitude of the harmonics for the chosen configuration [30].

To finish the windings project, the number of turns per coil must be defined. To perform this calculation, the magnetic flux per coil, which is highly dependent on the rotor and stator geometry, must be known. As a consequence, this topic will be analysed only after the selection of the electromagnetic best individual.

3.4 Electromagnetic Optimization

"The best solution for a certain machine should be given by its ability to fit the constraints predefined by the designer" [31]. Electromagnetic, thermal and mechanical phenomena are strongly interdependent by non-linear relations and a modification in one dimension can lead to changes on the specifications of the motor. In the past, motors were designed according to tables built within years of experience. Nowadays, with the increasing of the computational resources and with the development of finite element analysis tools, it is possible to calculate, with low error, the power, the torque, the losses and other motor's parameters. The optimization algorithm used to assist the motor design in this research was a single objective GA.

The optimization process is shown in Figure 3.5. According to this figure, the GA works together with a Finite Element Analysis tool to produce the optimum solutions [32] and [33]. In the latter software, the motor geometry is modeled and electromagnetic analyses are carried out. The maximum torque value obtained is returned to the optimization algorithm and a score is defined based on the constraints and on the torque results. The best results of each generation moves to the next iteration, depending on the user definitions (elite count).

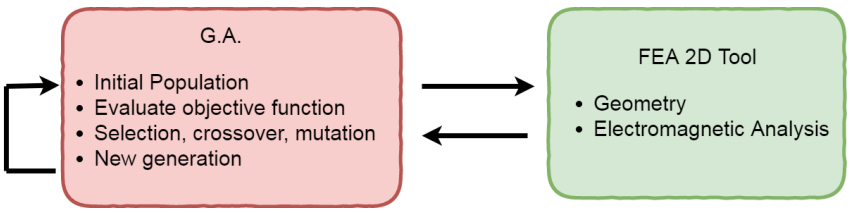

Figure 3.5: Algorithm process.

3.4.1 Genetic Algorithm (GA)

The GA is a type of optimization algorithm based on natural selection (as the biological evolution and genetics). Each problem is solved taking into account the constrained and unconstrained space, where a random set of individuals for the current population is created. Current set of individuals can progress from generation to generation: parents are used to create children for the next generations. These children can suffer changes on their genome (input decision variables), essentially by: i) mutation (random changes to the individual genome), ii) crossover (combination of the genome of two parents, normally the ones with higher ability to continue to the next generation). This method creates diversity, assuring that different areas of the entire problem are taken into account and avoiding the convergence to the same local minimum value over time. The population evolves gradually, from generation to generation, to a minimum value or optimal solution (defined by the objective function). All individuals are rated according to the fitness score assigned to each solution. This score will define the ability of an individual to progress to the next generation. The population space is limited by the constraints that rate an individual with a low value to prevent it to propagate over generations [29].

This algorithm is usually applied to problems in which the objective function is discontinuous, non-differentiable, highly non-linear or even to black-box functions.

GA was chosen because it is one of the most robust when compared with other optimization algorithms, especially when new inputs are changed. Also, it is easy to understand and it always returns an output that can improve over time. On the other hand, the main disadvantages are the following: i) GA does not guarantee the finding of the global maximum; ii) it can take more time to converge than other optimization algorithms.

Objective Function

The objective function of the algorithm consists in minimizing the negative value of the maximum motor torque (f(1))- Equation 3.1). It is considered that the maximum torque will be produced at the maximum feeding current available from the inverter, without saturating the magnetic core.

$$\min_{x \in \Omega} \quad F(x) \equiv (-f_1(x)) \tag{3.1}$$

Decision Variables

The motor geometry is created according to the seven decision variables presented in Table 3.3. These variables are discrete with a step of 1 mm because very high manufacturing tolerances are not expected to be adopted and also to decrease the entire population space in order to converge more rapidly.

Table 3.3: Motor decision variables.

Design Parameter	Variable	Range
Rotor radius	RR	20-40 mm
Magnet width	MW	1-7 mm
Magnet length	MT	5-15 mm
Teeth width	TW	1-10
Length of teeth	LT	7-20 mm
Air-gap size	AS	1-5 mm
Shaft radius	SR	5-30 mm

These decision variables define the 2D geometry of the motor; a representation is shown in Figure 3.6.

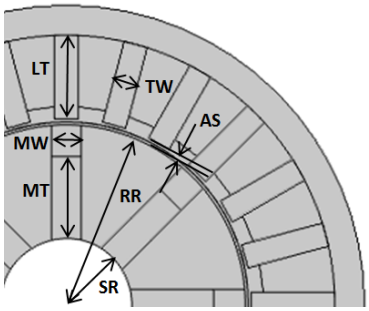

Figure 3.6: Cross-section of *spoke* geometry with the geometric parameters.

Constraints

Table 3.4 presents the constraints values that physically limit the motor manufacturing. Some others constraints must also be considered, for instance, the weight and the magnetic flux density which must also be limited. The first limit is imposed by the user according to the requirements and the second one is defined by the magnetic saturation value in the magnetic core materials. Therefore, the material chosen for the magnetic material is NO20, which has a saturation value of 1.9 T (Appendix B [34]).

Table 3.4: Design constraints for the traction motor.

	Design Constraint	Constraint value
Geometrical	Weight	$<$5Kg
	Stator outer radius	50 mm
	Stack length of the motor	80 mm
Inverter	Peak current	100 A
Thermal	Copper winding temperature	180 ^{o}C
	Permanent magnet temperature	120 ^{o}C
Magnetic	Magnetic flux density	$<$1.9 T

3.4.2 Finite Element Analysis Software

Geometry

The first thing to define is, according to the FEA software, the geometry, which can be imported from a Computer-aided design (CAD) software in many formats, and in 2 or 3 dimensions. In the present work,

and regarding the optimization algorithm, the various geometries were designed in a Matlab script, with different dimensions according to the decision variables [35].

After the geometry is defined, a control check is conducted to assure that it has physical coherency, without parts overlapping or being outside the dimensions limits.

Material properties

The materials are later selected for each domain according to the part of the motor in which each domain is inserted. NO20 non-oriented steel was selected for the rotor and stator domains. The characteristics of this material, which can be seen in Table 2.1, had to be inserted in the script. For the coils, the entire domain is selected as standard copper, with the characteristics shown is Table 2.4. NdFeB is defined for the PM domains (Table 2.2). At last, for the remaining domains, as the shaft domain and air-gap, all are selected as air.

Boundary conditions

The boundary conditions are defined for each domain according to the following: i) the magnetic insulation is set for the outer diameter of the stator; ii) an initial value of 0 Wb/m is applied to all the domains of the motor; iii) stator and rotor core are selected with a constitutive relation defined by its B-H curve; iv) PM with a constitutive relation defined by the remanent magnetic flux density, perpendicular to the magnet radial axis, with 1.3 T and with the same magnetic poles facing two consecutive magnets; v) the coils domains are selected having a sinusoidal external current density with an amplitude of 10A/mm^2, with a phase difference of one third the period between each phase and with a frequency of 400Hz (the winding layout previously studied is inserted on the script depending on the number of windings). The current density was defined taking into consideration that 10A/mm^2 is the boundary between an high efficient heat removal fan cooling system and a non-efficient heat removal liquid cooled system (that can increase to 30A/mm^2 for high efficient systems) [12]. Once the cooling system had never been developed and tested before, a conservative value for the current density was chosen. 400Hz was defined based on the average speed the car does (which is proportional to motor speed), during an endurance race.

Mesh and simulation

Mesh resolution and its quality are important aspects to consider when validating the Finite element model, as low mesh resolution can lead to inaccurate results. Furthermore, it can create inverted mesh elements and high condition numbers for the Jacobians, which can cause convergence issues while running the simulation [36]. The used FEA software has default mesh settings that can be selected. In the script, as the geometries change between different individuals, it is hard to define a mesh with specific properties. Furthermore, the selection of any of the default meshes available facilitates the script. Therefore, a simulation was made to analyse the convergence properties of the different meshes, to select the best one for this case (Table 3.5 and Figure 3.7).

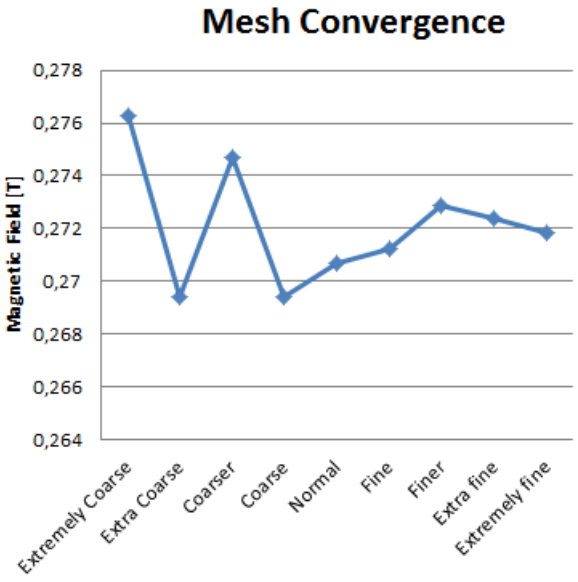

Figure 3.7: Default FEA software mesh convergence analysis.

Table 3.5: Different default meshes parameters.

Element size	Domain Elements	Average Quality	Study Time [s]
Extremely Coarse	8934	0.6390	12
Extra Coarse	20766	0.7027	18
Coarser	32548	0.2932	32
Coarse	41670	0.7783	35
Normal	81768	0.7554	77
Fine	85982	0.7994	83
Finer	219724	0.8169	224
Extra Fine	349952	0.8258	332
Extremely Fine	1192362	0.8436	1381 (23 min)

According to Figure 3.7, the initial geometry, from where all the individuals are changed, was used to conduct the mesh convergence analysis. A singular point, where the magnetic flux density is calculated, is set in the middle of one stator tooth, in a place, where it is not influenced by the mesh size, and distant from singularities that can also disturb the final result. The magnetic flux density in that singular point is analysed because it is the parameter that FEA software calculates in the electromagnetic problem using Maxwell equations [35], and also because it is from this one that all the other parameters are calculated, therefore errors associated to calculations can be minimized. By tracing a graph of the magnetic flux density for each different mesh, it is possible to see a convergence of the values (Figure 3.7). The meshes from normal to extremely fine are more suitable according to the convergence graph. Additional data of the different meshes is added in Table 3.5.

From Table 3.5, it can be seen that the computation time is acceptable from extremely coarse to fine meshes. It starts to increase considerably from the finer mesh to the extremely fine. Furthermore, this time does not include the time to build the mesh which, for extra and extremely fine meshes is not negligible, as it can take up to 120 seconds, further adding to the total time. The average quality is a control parameter available from the FEA software that rates the mesh elements from 0 to 1 (being 0 a

degenerated/deformed element and 1 a perfectly regular element) [37].

The selected default mesh is the normal, once it falls inside the convergence area, has a good average quality and takes acceptable time to run. This last parameter is the most relevant one, once that more than hundreds of individuals will be analysed during the optimization.

A parametric study is selected to determine the maximum motor torque, where the angle of the magnetic flux density produced by the stator coils rotates while the rotor is fixed. For each individual, the study is performed during a quarter of rotation and with a step of 1/40 of the revolution.

The FEA software solves the Maxwell's equations to certain boundary conditions, which were shown before [35].

The values exported from the FEA software, relevant for this analysis, are the shaft axial torque and the magnetic flux density on the 2D plane.

There are many methods in the literature that can be applied to calculate torque in FEA. The most well known are specified on the list bellow [38]:

- **Maxwell Stress Tensor** - it is possible to obtain the force integrating the Maxwell stress tensor (MST) along a surface. This method is simple to apply and needs small calculation time, although it can be less accurate, since it is very sensible to the selection of the integration line of the contour [39]. For two-dimensional electromagnetic models, the relation is show in Equation 3.2 where T_e is the electromagnetic torque, L is the active length of the machine, r is the radius closed surface in the motor air-gap, B_r and B_θ are the radial and tangential components of the flux density. The integral is performed from 0 to 2π, taking into consideration the periodicity of electrical machines. The result must be multiplied by the number of pole pairs.

$$T_e = \frac{L}{\mu_0} \int_0^{2\pi} r^2 B_r B_\theta d\theta \tag{3.2}$$

- **Arkkio's Method** - this method is a variant of the MST method, where the whole air-gap volume is comprised between the layers of radius r_r and r_s (middle of air-gap until rotor perimeter). This method is less sensitive to mesh size and can cancel some part of the ripple caused by the differentiation on the MST method. The expression of the Arkkio's method is shown in Equation 3.3,

$$T_e = \frac{L}{\mu_0 (r_s - r_r)} \int_S r B_r B_\theta dS \tag{3.3}$$

  where dS represents the differential surface area in cylindrical coordinates.

- **Method of Magnetic Coenergy Derivation** - this method consists in deriving the magnetic coenergy $W_{Coenergy}$, maintaining the current constant with a displacement angle θ in order to calculate the torque. In this method, the time calculation is higher because the magnetic flux density must be solved twice to get an energy difference. The expression is shown in Equation 3.4

$$T_e = \left. \frac{\Delta W_{Coenergy}}{\Delta \theta} \right|_{i=constant} \tag{3.4}$$

The torque method selected was the MST method, which the FEA software calculated using Equation 3.5 [35]:

$$\mathbf{n_1}T_e = -\frac{1}{2}\mathbf{n_1}(\mathbf{H} \bullet \mathbf{B}) + (\mathbf{n_1} \bullet \mathbf{H})\mathbf{B^T} \tag{3.5}$$

Integrated on the surface to obtain the force, where $\mathbf{n}_1$ is the outward normal from the object, T_2 is the torque **E** is the electric field, **D** the electric displacement, **H** the magnetic field, **B** the magnetic flux density. Although this method is less accurate than the Arkkios method, it is easier to define when programing the FEA software as it is available in the software. Arkkio's method takes more time and needs to be manually defined on the software. The Magnetic Coenergy Derivation Method requires a manual selection of the data to be derived, and as the objective is to develop the algorithm to work automatically, this method was also left aside.

3.4.3 Optimized Results

More than 50 analyses were made, with a total computing time of 1135 hours. These analyses were divided into 4 categories: the "preliminary tests" (where the algorithm was tuned to work without errors) and the "12 slots", "24 slots" and "30 slots" according to the number of slots of the motor - Table 3.6. In each category, geometries varying from 4 to 10 magnetic poles were also studied.

Single layer coils were selected, aiming at a manufacturing process as less complex as possible. In fact, at this stage, the objective was to build a motor prototype to validate the theoretical simulations. With that aim, it will be possible to reduce errors associated with the motor's construction.

Due to the FEA simulation times, the population size and number of generations were set to 10 and 50, respectively. A total of 47h40m were required to perform the optimization.

The best torque results from the performed optimization are shown in Table 3.7 and the optimized geometry of the best individual is presented in Figure 3.8.

The geometry with 24 slots was selected as it presented the highest torque value. Further analyses were conducted to the adopted geometry, magnetic flux density and torque value along time, namely for a sinusoidal current wave feeding the motor terminals, as shown in Figure 3.9.

It is possible to see in Figure 3.9(b) that the maximum torque is about 25 Nm with an angle of the rotor to the stator axis (theta) of 51 degrees and at this value there is not magnetic saturation in the core, as the maximum registered value is 1.8 T (Figure 3.9(a)). This result is higher than the defined value as objective which gives a margin to the iterations of the mechanical and thermal model to be done. It

Table 3.6: Number of population elements and generations tested during the first version of the optimization.

Study	Number of Studies	Time of Studies [h]
Preliminary tests	24	181
12 slots	16	429
24 slots	5	170
30 slots	8	355
Total	53	1135

Table 3.7: Algorithm best results for each category.

Study	Torque [Nm]	Weight [Kg]
12 slots	15.27	5.0
24 slots	25.50	4.49
30 slots	14.47	4.86

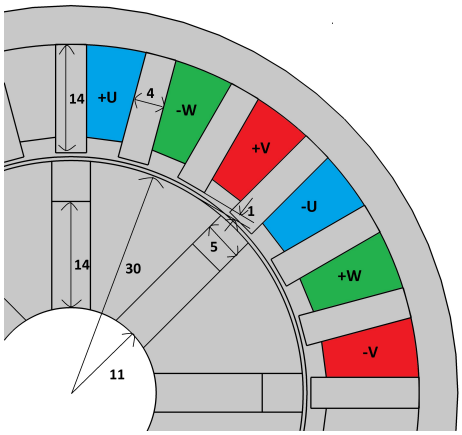

Figure 3.8: Motor optimization best result selected.

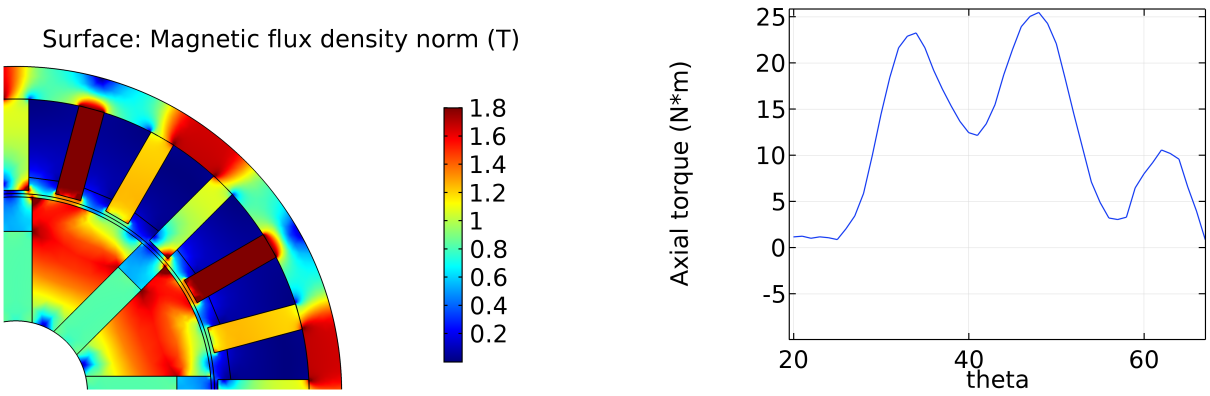

(a) 2D magnetic flux density of the result with 24 slots.

(b) Simulated prototype torque.

Figure 3.9: FEA Result with 24 slots.

is expected to lose some torque when doing those iterations, as the goal is to assure the mechanical and thermal functionality of the motor rather than improve torque. The mesh used for these analyses is shown in Appendix C.

The complete table of results with all the individuals obtained during this version of the GA is shown in Appendix D.

3.4.4 Tooth lips of the stator

The tooth lips of the stator were analysed too (Figure 3.10). They support the copper windings on the slots and prevent them from falling to the air-gap with the vibrations of the motor and the electromagnetic forces caused by the currents and magnetic flux density in the wire.

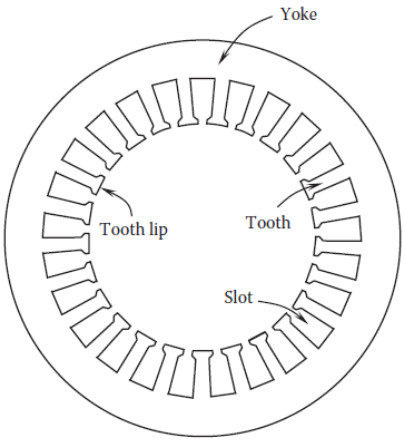

Figure 3.10: Stator with tooth lips.

Simulations were made to the electromagnetic geometry considering two different cases: a stator without lips and a stator with lips. These simulations showed a decrease of about 15% of the output torque. Although the ripple is expected to decrease considerably, the difference of torque in this motor when using lips in the stator slots is large enough to continue with the first solution (without lips). This solution will complicate the work of winding the motor and can raise problems as retaining the windings in the slots, preventing them from going to the air-gap. The solution found to overcome this problem was to add a special coating of epoxy to fix the windings.

3.5 Improvement of the Electromagnetic Optimization

3.5.1 First Improvement (GA V1)

After ending the prototype design, an extensive set of tests was carried out to analyse the prototype behavior and performance (see Chapter 5). According to the results obtained, several improvements were carried out.

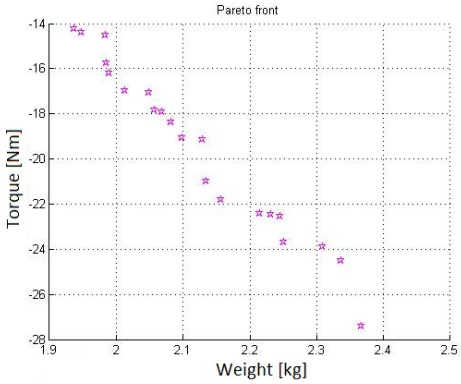

Figure 3.11: Pareto Front from GA-V1.

First, the electromagnetic optimization algorithm was modified: the objective changed from a single to a multi (double) objective. Second, as minimizing the motor weight was very important, instead of constraining this variable as it was done in the prototype MJF_V0 version, the weight was also considered as an objective (added to torque). With this, it was possible to select an individual of the Pareto Front (Figure 3.11) worst in one objective but better regarding another. For example, between two individuals, one with 20 Nm and 5 kg and other with 19.9 Nm and 4 kg, it is possible to visually select the second. A Pareto Front represents the dominant individuals considered equally good when assessing both objectives (torque and weight). These non-dominant individuals cannot be improved in value without degrading the other objective value [40].

With the validation and testing of the motor manufactured, it was also possible to be more demanding with the tolerances, for example, decreasing the air-gap.

Other improvements were made, regarding the magnetic curve of the material, which was changed to HiperCo in the FEA Software and the saturation of the material that was also changed to 2.1 T with an allowed maximum of 2.3 T in some specific points that will saturate first, such as magnet-bridges. The current density per slot was changed from a fixed 10 A/mm^2 to 18 A/mm^2 as it was evident during the tests that the inverter was able to deliver more current. The stacking of the motor decreased from 80mm to 65mm to reduce the overall length of the motor and to facilitate its attachment to the upright of the car.

During this version, 43 different optimization studies were conducted performing a total of 532 hours of computation. The best result had a torque of 27.4 Nm and a weight of 2.37 kg (11.6 Nm/kg) representing an increment of 70% in relation to the best individual from the previous version.

The complete table of results with all the individuals obtained during this version of the GA is shown in Appendix D.

3.5.2 Second Improvement (GA V2)

During the simulations of GA_V1, some aspects were identified as parameters to be improved. To begin with, when choosing the best individuals of the Pareto Front, it was noticed that it would make more sense to optimize the ratio torque/weight, changing the problem to a single-objective (Figure 3.12). The

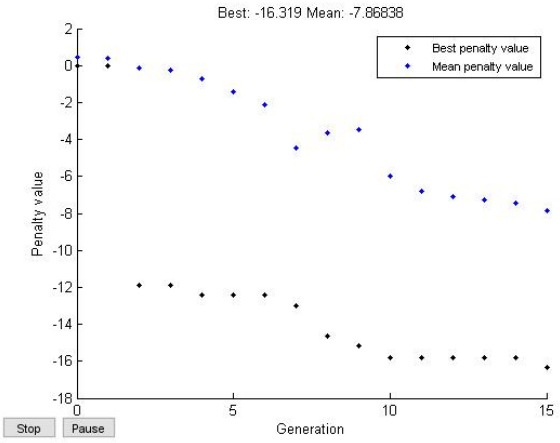

Figure 3.12: Best individual from GA-V2.

difference to the first version is that now the objective to optimize is the ratio torque/weight, instead of optimizing torque by limiting weight. The prototype was built as a proof of concept to be only tested in a test-bench, but for a solution to integrated in a car, where weight is crucial, it must also be optimized. Furthermore, the lessons learned with the prototype enabled to increase the credibility on the theoretical models, to be more rigorous in the manufacturing and to increase the budget available to the versions which followed, allowing to develop newer versions more robust and with higher performance. By selecting the individual with higher torque/weight ratio, it was possible to change the torque value, decreasing (or increasing) the stack length with the certainty that this will be the best individual for this optimization.

Furthermore, it was possible to change the coils current, defining the current crossing each coil instead of defining the slot current density. With this, and considering the maximum fill factor of 50%, according to the manufacturing experience acquired during the prototype manufacturing, a new decision variable was set: the number of turns per coil.

In Figure 3.12 it is possible to see the best result so far of this version. It shows a ratio torque/weight around 16.3 Nm/kg. Comparing it to the first version best individual (26Nm and 3.8kg) with a ratio of 6.84 Nm/kg, the ratio improved by 138%. It is, in fact, astonishing but it is unfair to compare without notice that big changes regarding the use of Hiperco, the reduction of the air-gap to half and the increment of the current density 3 times influenced a lot more than the changes in the geometry optimized throughout the different versions.

The complete table of results with all the individuals obtained during this version of the GA is shown in Appendix D.

3.6 Mechanical analysis

The mechanical project of the electric motors is as important as the electromagnetic. Ideally the optimization software should include the parameters and results of the mechanical analysis, but to include that on the script would require a lot more time and knowledge. Manual iterations were carried out after the electromagnetic optimization to assure the design requirements of the MJF motor. The motor must

be able to perform 20000 RPM to prevent damage in case of a overspeed fault; to perform that, the rotor needs to support and sustain the different pieces and also needs to be able to withstand 20 Nm of peak torque generation.

To start, the analysis of the shaft to assure that the motor could handle the centrifugal forces in case of overspeed, dictated some modifications on the rotor. Further analysis regarding the magnets mechanical behavior were also done. The stator practically did not changed during the process: the only alteration performed was regarding a key, that was added on the stator outer diameter to assure that it would not spin in relation to the motor housing. This was done because one of the motor requirements is to have the capacity of being totally disassembled: this requirement made impossible to assure the stator is constrained by applying the ideal mechanical tight fit.

Analytical study was performed with FEA simulations to calculate the stress distribution. The assumption of an uniform distribution of stress was considered during this analysis to simplify the calculations [41]. Special attention was given to the following load cases: i) centrifugal force due to rotor rotation on the magnets; ii) centrifugal force due to rotor rotation on the shaft fins; iii) the maximum torque generation.

For the case i), shear stress equation defines the stresses the magnet surface is subjected and, comparing with the yield tensile stress of the glue, it is possible to determine if the glue is capable of holding the magnets in place when the velocity is 20 000 RPM. Shear stress occurs when a parallel force to the surface being studied causes deformation, where a displacement relative to the bottom face of the object can occur, in case the stresses are higher than the material properties.

First, the velocity (Equation 3.6) and acceleration (Equation 3.7) at the rotor outer diameter are calculated :

$$v = w \times r \tag{3.6}$$

1. a_c Acceleration
2. v Velocity
3. r radius $= 25mm$
4. w angular velocity $= 2095rad/s (20000$ RPM)

$$a_c = \frac{v^2}{r} = 110000m/s^2 \tag{3.7}$$

The shear stress will be assessed in the surface between each magnet and the glue, being $0.046kg$ the mass of one magnet. Knowing the acceleration and the mass, it becomes possible to determine the forces involved in that surface (Equation 3.8):

$$F = 0.046kg \times 110000m/s^2 = 5060N \tag{3.8}$$

The contact area of the magnets with the rotor steel defines the glue contact area, being 1135 mm^2 (given by SolidWorks (SW) software), so the shear stress is shown in Equation 3.9:

$$\tau = \frac{F}{A} = \frac{5060N}{1135mm^2} \approx 4.5MPa \tag{3.9}$$

The shear stress applied on the magnets is 4.5 MPa. The glue 3M DP490 has 30 MPa of shear strength, so it can hold the magnets in place. Furthermore, magnet-bridges (Figure 3.13) were added to reinforce, due to the high level of uncertainty associated with bonded solutions with glue, where the manufacturer strength value is only achieved under ideal bonding conditions, such as, extremely clean assembly rooms, surface cleaning, glue curing cycles without temperature variation, etc.

Considering the thickness of the magnet-bridge A_{bridge}= 0.5 mm and the motor stack length of 80 mm, the area perpendicular to the load case is defined by Equation 3.10, the acceleration is given by Equation 3.7 and the forces acting in that area are shown in Equation 3.8.

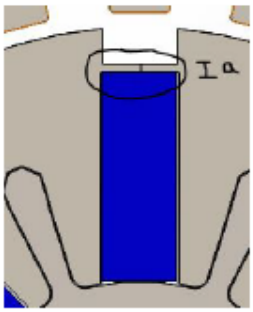

Figure 3.13: Magnet-bridge.

$$A_{bridge} = 0.5mm^2 \times 80mm^2 = 40mm^2 \tag{3.10}$$

The tensile stress is given by Equation 3.11:

$$\tau = \frac{5060N}{40mm^2} = 126.MPa \tag{3.11}$$

The shear stress induced in the magnet-bridge produced my the magnet acceleration is 126.5 MPa, which is lower than the NO20 yield stress of 400 MPa, assuring that no failure will take place.

For the case ii), tensile stress equation defines if the stainless steel material is capable of holding the rotor directly attached at a speed of 20 000 RPM. Tensile stress occurs when a perpendicular force to the surface being studied compress or decompresses the object. This force causes a deformation of the material and if it is higher than the yield tensile strength it can lead to material failure.

Considering the fin base of 1.5 mm, as shown in the Figure 3.14, and the stack rotor length of 80 mm, the forces that will act in that area are given by Equation 3.12:

$$A_{fin} = 1.5mm^2 \times 80mm^2 = 120mm^2 \tag{3.12}$$

The mass of one magnet is $0.046kg$ and the mass of one piece of the rotor is $0.104kg$, so the total

mass that one fin must hold is $0.15kg$ (Equation 3.13).

$$m_{total} = 0.15kg \tag{3.13}$$

The forces are given by Equation 3.14

$$F = 110000m/s^2 \times 0.15kg \approx 17000N \tag{3.14}$$

So, the tensile stress is given by Equation 3.15:

$$\sigma = \frac{F}{A} = \frac{17000N}{120mm^2} = 141.6MPa \tag{3.15}$$

As a conclusion, the tensile stress induced in the shaft fin is 141.6 MPa, with a base thickness of 1.5 mm. The AISI 316 stainless steel ordered has an yield stress of 290 MPa, thus accomplishing the defined requirements.

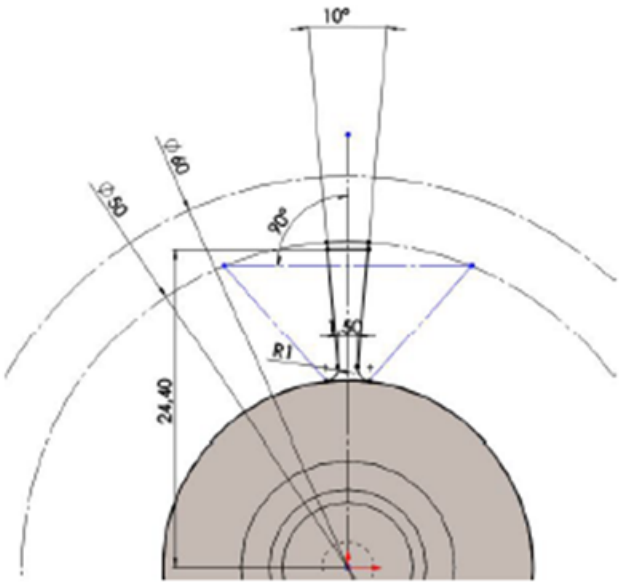

Figure 3.14: Drawing of one shaft fin.

After conducting the analytical calculations previously shown, a FEA of the shaft was done in SW software to verify the credibility of the results for case i) and ii) (Figure 3.15) and to study and analyse case iii) (Figure 3.16). It is important to refer that SW software is not the best software to perform FEA, but once the material is considered isotropic, this software is accurate enough and was considered to undertake this kind of simulation.

Regarding the forces produced by the rotation of the rotor, the shaft geometry was used and the constraints were selected on the bearings diameter surface to simulate the real radial constraint that the bearings produce on the shaft (Figure 3.15(a)). The forces corresponding to 17 000N (centrifugal forces at 20000 RPM) were applied radially to the shaft fin.

To analyse if the shaft with AISI 316 stainless steel can withstand the force produced by the torque generation (case iii)), another simulation was carried out with SW software (Figure 3.15(b)). The shaft geometry was selected with the material properties shown in the Chapter 2. A fixed area corresponding to the shaft output coupler was selected to simulate the worst case scenario: the shaft being blocked but the motor generating the maximum torque. A load torque of 20 Nm was defined perpendicular to the shaft splines axial axis.

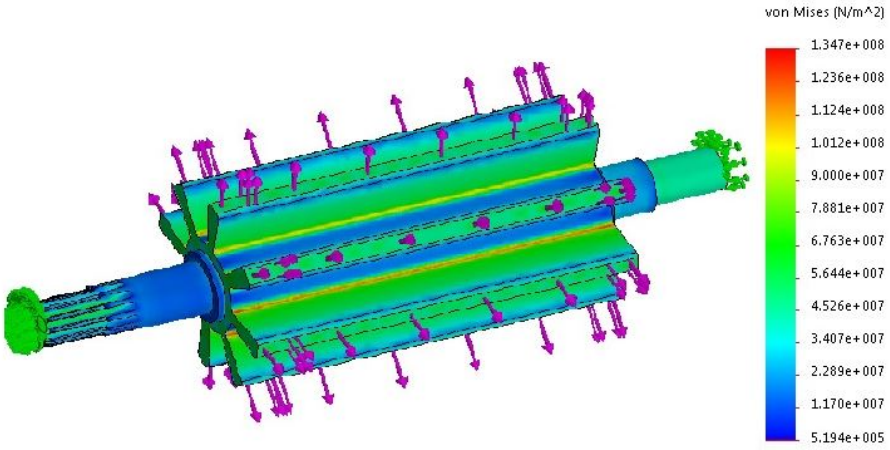

(a) Simulation of the fins when rotating at 20 000 RPM.

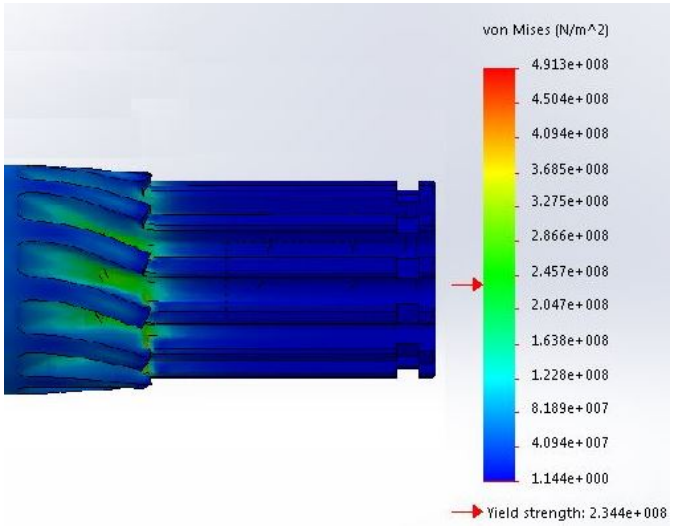

(b) 20Nm torque load on spline.

Figure 3.15: Mechanical analysis using FEM software.

Results in Figure 3.15(a) proved as expected, that the fins base is the most sensible area due to its short thickness. Also, and as the calculations carried out previously showed, the material can withstand the forces with a mechanical Factor of Safety (FoS) of 2.15, which means this piece can support up to 2.15 times the design load without failing. It is relevant also to say that the FEA result was 134.7 MPa, near to 141.6 MPa obtained on the analytical analysis.

Regarding the torque generation, the most sensible area is the shaft splines of the copulation. As it is possible to see in Figure 3.15(b), the splines cannot withstand the stress produced by the torque generation, where the stress is up to 491.3 MPa (higher than the 290 MPa yield tensile strength of the

material selected). That part shows an area of stress concentrations where the spline diameter changes abruptly. A singularity was also created, which leads to higher calculation errors in the software.

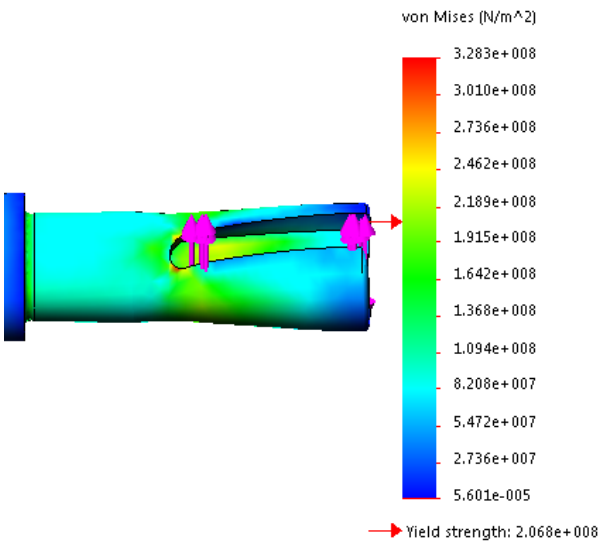

Figure 3.16: Shaft keyseat analyse.

A softer transition should be applied instead. But the prototype does not require this kind of coupling, as it will be not used with the car gear box. Therefore, another design was envisaged (Figure 3.16).

In Figure 3.16 it is possible to see that the maximum stress produced is 328.3 MPa. Although it happens in a very specific and short area, where a chamfer do exists, this, together with the visualization of the stresses that are considerably less in the surrounding area, suggest that it is a singularity. So, it was assumed that the shaft could hold the forces created when the motor is generating the maximum torque with a FoS of 1. Some displacement is expected, but as the value is within the ultimate tensile strength of 580 MPa, the material will not fail. A thermal treatment for the shaft material will be required to increase the value of its surface yield strength.

3.6.1 Material: Aluminum versus Stainless steel

The study of a shaft made of aluminum 7075, with higher yield strength was carried out, after having the results regarding the ability of the stainless steel shaft to withstand 20 Nm of torque.

This time, as the aluminum has mechanical advantages, not only analyses regarding the mechanical behavior were done, but an assessment of the losses due to induced currents was also performed. Figure 3.17 shows the mechanical and temperature analyses for the 7075 Aluminum and the AISI 316 Stainless steel materials.

It is possible to conclude that the disadvantage of using aluminum instead of steel is that the induced currents in the shaft of the motor are near 50 % higher, in the first material, leading to higher losses and less efficiency. FEA shows that for Stainless steel, the total resistive loss is 1183 W/m^3 and with aluminum it reaches 26 827 W/m^3. In what concerns the temperature, the resistive energy dissipated in

the shaft can increase its temperature approximately 20 °C after 30 minutes (Figure 3.17(c) and Figure 3.17(d)).

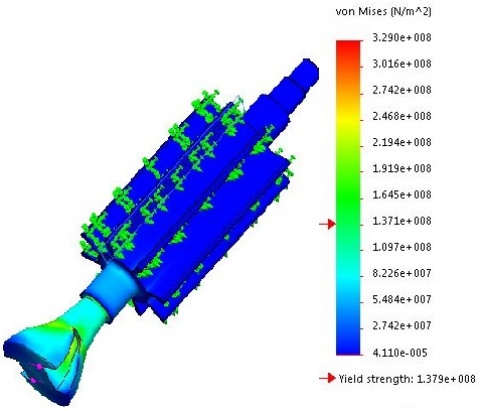

(a) Simulation using aluminum.

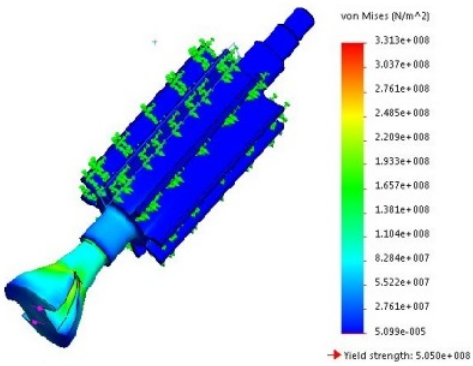

(b) Simulation using stainless steel.

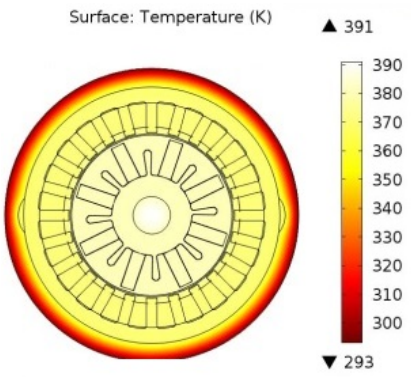

(c) Temperatures simulation when using aluminum.

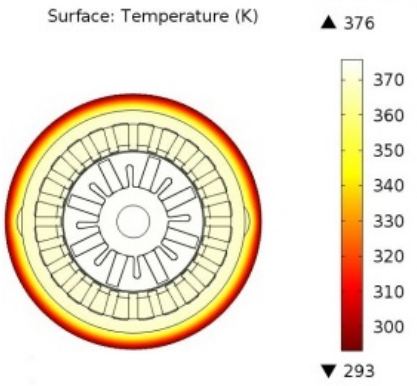

(d) Temperatures simulation when using stainless steel.

Figure 3.17: Comparison of the effects when using aluminum or stainless steel on the shaft.

Finally, and because heat removal from the rotor is a crucial parameter, the decision was to use stainless steel. Furthermore, as stated before, a thermal treatment of this material can be done to increase the value of yield tensile strength.

3.6.2 Clearance fits

Clearance fits are used during the design phase when dimensioning and defining tolerances for a geometric part. It defines the clearance between two mating parts, described as ‘shaft‘ and ‘hole‘, determining if the parts can move independently from each other, or are temporarily or permanently joined. The different methods to use when assembling two parts depend on the fit category (and class inside each category): clearance, transition and interference (Figure 3.18). The meanings and in what situations each class shall be used is shown in Appendix E.

For the shaft and rotor, a clearance fit H7/h6 was defined because, in one hand, the intention is to disassemble them without damaging the parts, but on the other hand, some interference is needed to assure the rotor does not slip in relation to the shaft.

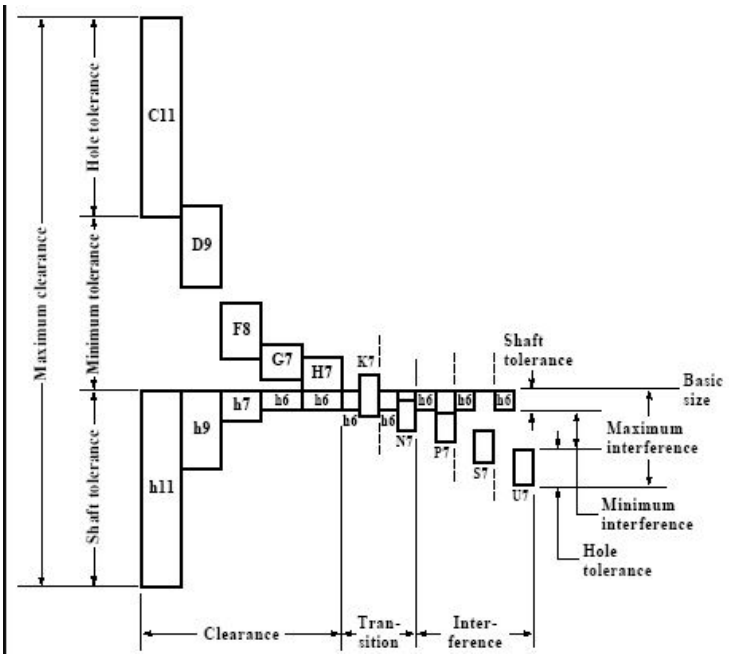

Figure 3.18: Clearance fit between shaft and hole.

Regarding the bearing and shaft, an interference fit H7/n6 was set, because they are supposed to be assembled using a hammer to prevent them to slip in relation to the shaft without applying high forces.

For the bearings and the motor housing caps interfaces, a transition fit H7/k6 was chosen because the bearings should handle the high vibrations and speeds without slip through the caps but also because they should be able to disassemble.

In the boundary between magnets and rotor, a clearance fit H11/c11 was selected because it is necessary to insert them without breaking or damaging. Furthermore, a clearance for glue was added.

Finally, a transition fit H7/k6 was defined between the jacket housing and the caps to assure that a radial movement between them, that would produce vibrations, is constrained but, at the same time, assuring that it is possible to disassemble them to open the motor.

3.7 Thermal Analysis

At last, a thermal analysis of the motor was conducted. It is probably fair to state that this is the most important analysis to take into account because, although the motor design is a result of the aggregation of the electromagnetic, mechanical and thermal analysis, at the end, the power and torque parameters are limited by thermal behavior of the motor [4]. With the same design, a motor can have higher power just by increasing the heat removal from its key components. This is not an easy task and requires a lot of knowledge in this field. Furthermore, thermal behavior is highly influenced by the manufacturing quality of the overall motor, ensuring that there are no small gaps between materials.

2D simulations were conducted under the scope of this work, to assure that the thermal limits of the motor are not reached when maximum power is provided (Figure 3.19). A more detailed analysis of the motor thermal behavior (Figure 3.20) and of the cooling system design and study (Figure 3.21) were

done in 3D, by another FST Lisboa team member, who was responsible for the car cooling system [13]. Those simulations were conducted taking into account the nominal torque (and power) instead of the peak values, as the cooling system is designed to assure that the motor does not overheat during one endurance race using the average power that the car needs.

2D thermal analysis carried out under the scope of this work has shown that the motor can withstand the currents involved in the generation of the maximum torque determined in the electromagnetic simulations, during a short period of time. The initial temperature set on the simulation was 30 °C. The total losses of the motor in the peak power situation, with a torque of 20 Nm at 9500 RPM, are the following in the thermal simulation: i) 4500 W in the coils; ii) 80.6 W in the magnets, iii) 46.6 W in the rotor core; iv) 65.6 W in the stator yoke core; v) 76.6 W in the stator teeth core.

The losses in the coils were calculated assuming only the contribution of the Joule losses (Equation 3.16) with a phase resistance of 0.3 Ω (calculated knowing the total length of each phase cable) and a peak current of 70.7 A_{RMS}.

$$P_{Joule} = 3R.I_{RMS}^2 \tag{3.16}$$

The iron losses in rotor and stator are a sum of: i) Eddy losses; ii) hysteresis losses; iii) excitation losses. In Equation 3.17, P_{Iron} are the losses in the iron by the Eddy phenomenon, K_{hyst} is the hysteresis constant of the material, B is the magnetic flux density [T],f the electric frequency [Hz] and K_{Eddy} is the Eddy constant.Their respective constants are shown in Equation 3.18 [42] [43].

$$P_{Iron} = K_{hyst}B^2 f + K_{Eddy} \times (B\ f)^2 + K_{exc}(B \times f)^{1,5} \tag{3.17}$$

$$\begin{aligned} K_{hyst} &= 0,0166 \\ K_{Eddy} &= 1,174E-5 \\ K_{exc} &= 6,112E-4 \end{aligned} \tag{3.18}$$

The losses on the magnets were determined applying Equation 3.19, where J_z is the induced current density in the z axis extracted from the FEA and σ_{Neod} is the electric conductivity of Neodymium magnets at 20 °C (1.375 $\times$ 10^6 [S/m]), l_m, h_m and b_m are the magnets height, width and length respectively:

$$P_{mag} = l_m \int_0^{h_m} \int_0^{b_m} \frac{J_z^2(x,y)}{\sigma_{Neod}} \tag{3.19}$$

The first approach in the 2D (instead of 3D) thermal FEA simulation was considered, in order to simplify the problem and therefore reduce the computation time. The outer diameter of the stator was defined as a boundary condition having a heat transfer coefficient of 10 W/(m^2K), the same used by [13] and the common value assumed natural convention heat transfer. The thermal simulation shown that the MJF motor can withstand up to 18 seconds the peak torque, considering an initial temperature of 30°C, without cooling system. At 18 seconds the windings will reach their maximum temperature (180°C), and since this is a short period of time, the rotor PM will not reach temperatures over 37°C.

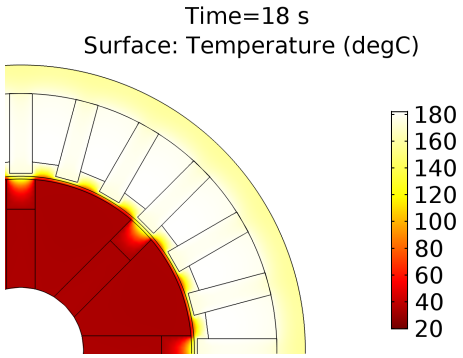

Figure 3.19: Thermal Simulation 2D.

In the simulation developed by Pedro Fontes [13], the geometry of the cooling jacket of the motor was optimized so that the maximum temperature of the magnets would not exceed 120°C. The initial temperature of the water was set at 30°C and the total power losses were considered as follows: i) 2200 W in the windings by Joules Losses; 20.6 W in the rotor; 61.5 W in the stator by iron losses. These values correspond to the losses at the a nominal power of the motor approximately 12 kW. Although, cheaper PM with a maximum working temperature of 80°C were used on the prototype, where a decrease of the nominal power is expected to be higher than 4 kW. Further simulations were not carried out, as the time required to perform this FEA would take more than one week and it is outside the scope of this thesis.

Figure 3.20 shows that the maximum simulated temperature in the magnets is 116.3°C, which is within the defined requirements for maximum temperature during one endurance race.

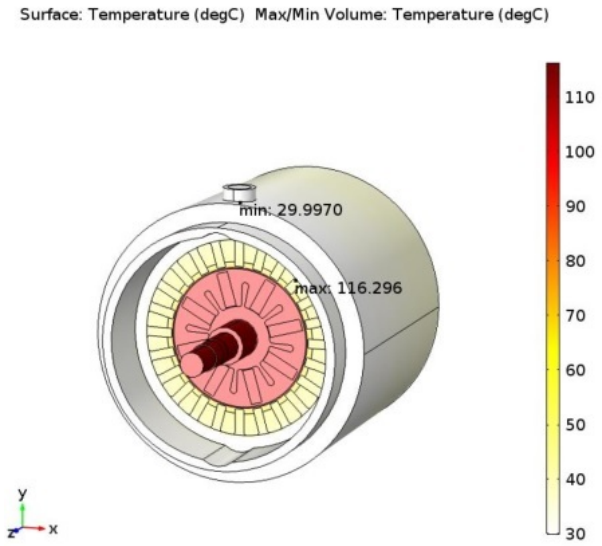

Figure 3.20: Motor temperature simulation when using the optimized cooling system [13].

Figure 3.21 shows the water temperature variation when dissipating around 2300 W of power losses. This result is relevant as the cooling system of the car has other components in series that receive the water coming from the motors.

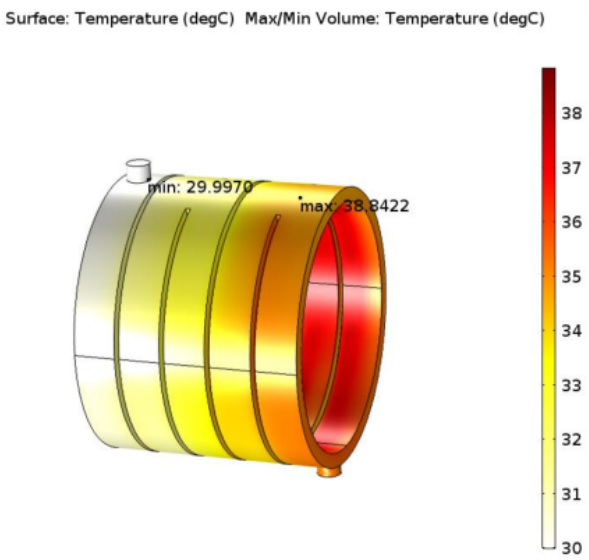

Figure 3.21: Water temperature when dissipation 2300 W [13].

3.8 MJF iterations

3.8.1 Shaft

The project of the shaft suffered several iterations over the time (Figure 3.22). Initially, the shaft was designed as being a simple cylinder with different diameters according to the bearings and encoder that were copulated in it.

In a second approach, the rotor was changed to eight equal separated pieces instead of one. With this configuration, the shaft is responsible of maintaining the structure of the all rotor and so fins were added to sustain the pieces. The spline to copulate the shaft to the gearbox was also added.

In a third approach, some optimization using electromagnetic simulations were made and the glue contact area was increased. Furthermore, the space available to copper windings was increased. So the width of the main fins was reduced and the length of the shaft increased.

In the final version, because of the difficulty of manufacturing the splines within the available time, it was decided to change the spline to two keyseat slots.

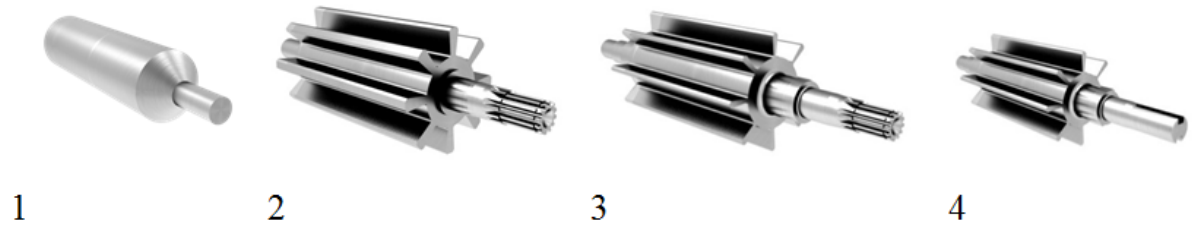

Figure 3.22: Shaft optimization design.

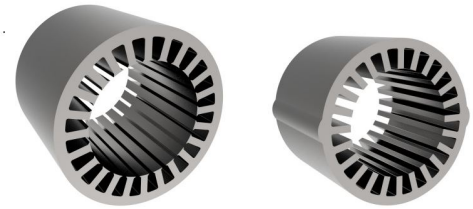

(a) 1^{st} (b) 2^{nd}

Figure 3.23: Stator optimization design.

3.8.2 Stator

The geometry and dimensions of the stator are a result of the optimization algorithm and did not change over the time. The only thing that was independently studied was the use of larger teeth to sustain the windings easily (Figure 3.23). This configuration showed a decrease on the final torque, so it was abandoned, as described before.

In the final version, a keyway was added to fix the stator to the jacket and guarantee the maintenance of axial and radial positions together with the bearings.

3.8.3 Rotor

The rotor design also suffered several iterations (Figure 3.24).

The first version of the rotor was the result of the electromagnetic optimization. All the dimensions and geometries come from the optimization without taking into account complex mechanical or thermal analyses.

In the second version, the mechanical analysis of the torque transmitted by the rotor to the shaft was considered and it was necessary to add fins in the shaft of the rotor, as already said.

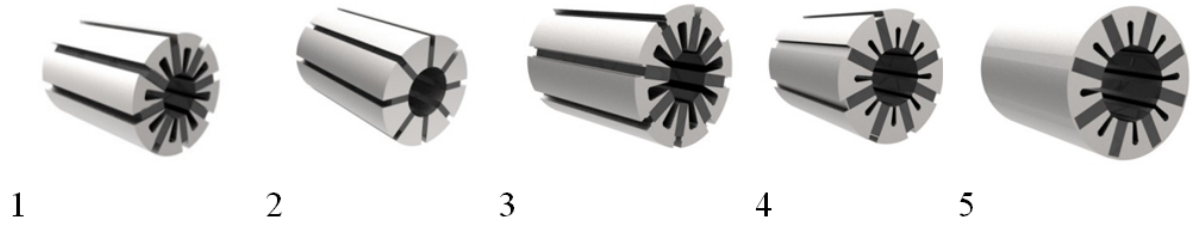

Figure 3.24: Rotor optimization design.

In the third version, bridges to the magnets were added in the rotor. As further analyses shown, it was noticed that the area available to glue the magnets was not enough to fix them at the maximum rotational speed. Therefore, a house to retain the magnets was added.

After having discussed this subject with the manufacturer it was decided to join the eight different rotor pieces to decrease the manufacturing costs, so the fourth version of the rotor had the bridges of the magnets joined.

3.9 Final Model Electromagnetic Simulation

The motor torque decreased, after having done the changes in the best result of the optimization that was presented in the previous sub-chapter. Those modifications were performed in the magnetic circuit to make possible the fabrication of the machine's prototype. The changes that influenced more the torque generation were in the rotor: fins were added to the shaft to withstand the high forces, bridges were provided to the magnets and the integration of all the 8 parts of the rotor in just one was considered (Figure 3.25).

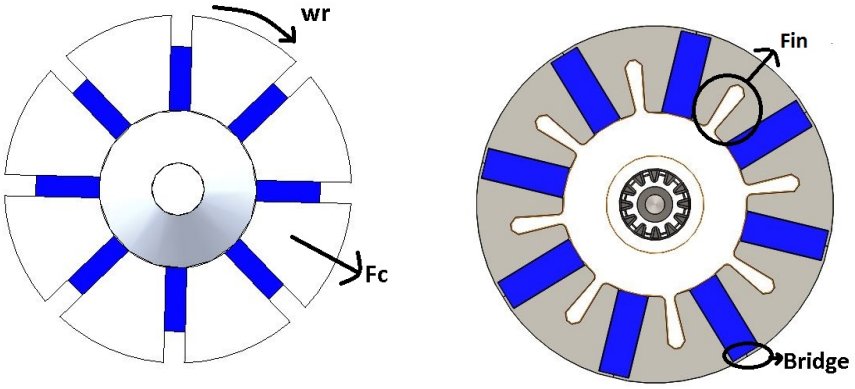

(a) Initial rotor geometry result. (b) Final geometry iteration.

Figure 3.25: Rotor geometry.

The simulations of the magnetic flux density and of the torque output with an angle variation between the rotor and stator, after the modifications, are shown in Figure 3.26. The mesh used for these analyses is shown in Appendix C.

Analysing Figure 3.26(b) and comparing with Figure 3.9(b), it can be observed that these iterations lead to about 20% decrease of the motor maximum torque (from 25.5 Nm to 20.7 Nm). This effect is mainly due to the existence of the rotor bridges on the top of the magnets, which decrease the magnetic flux between the rotor and the stator, decreasing the torque production; they also increase the bridges saturation and contribute to the increase of the losses at that area. Moreover, the shaft diameter was increased in order to withstand the rotor forces and the material used in this simulation (NO20) is different from the material considered in the optimization algorithm (Standard magnetic iron). Nevertheless, this lower torque value is sufficient to continue with the motor manufacturing, as it is considered that this torque decrease percentage would be about the same value in others optimization results that had initially less torque. Figure 3.26(a) shows that no magnetic-saturation occur once the maximum registered value was around 1.7 T. Is also important to notice that this geometry is capable of withstanding the temperatures generated at peak torque with a duration up to 16 seconds (Figure 3.26(c)). The initial condition and boundaries conditions were the same used in section 3.7.

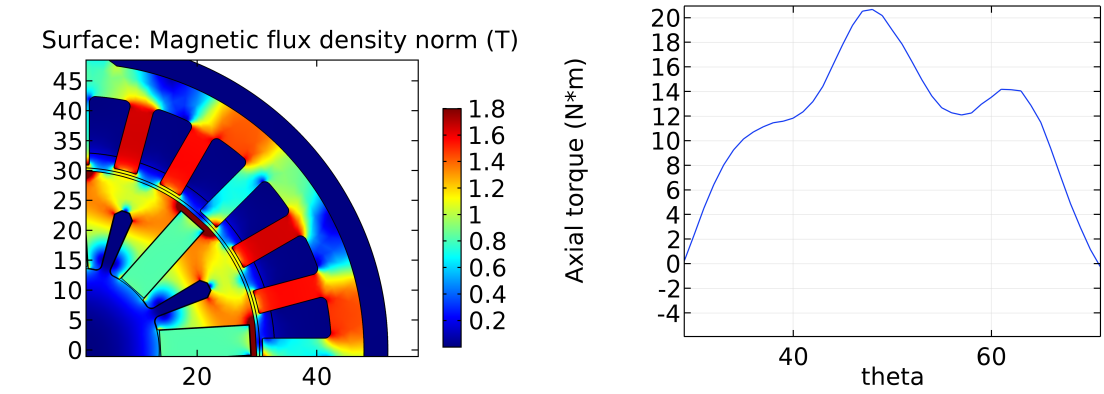

(a) 2D magnetic flux density of the final result with 24 slots.

(b) Simulated prototype torque.

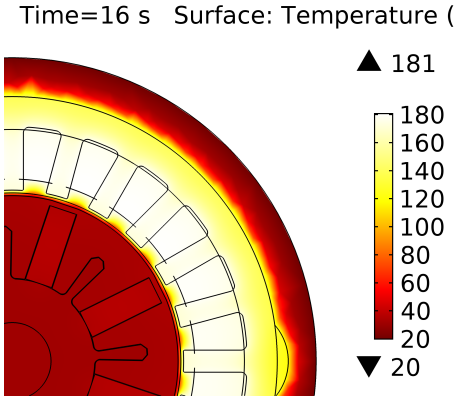

(c) Thermal simulation 2D.

Figure 3.26: FEA Result of the final version with 24 slots.

3.9.1 Number of turns per coil

After the winding configuration was selected and the motor geometry was set, the number of turns of each coil was analysed. The goal was to have a voltage constant (k_e) similar to the AMK motor - 18.8 V/kRPM (Appendix A). This BEMF was calculated according to Equation 3.20, where ϵ is the Electromotive force voltage [V], w is the mechanical frequency of the rotor [rad/s], pp is the number of pole pair, N_T is the number of turns of each coil and ϕ_{coil} is the flux of each coil [Wb] taken from FEA simulations ($\phi_{coil} = 0.0016Wb$). The results obtained, considering the latter equation are shown in Figure 3.27 for 4, 10 and 20 turns per coil.

$$\bar{\epsilon} = jw \times pp \times N_T \times \bar{\phi}_{coil} \tag{3.20}$$

It is important to refer that this theoretical graph does not take into consideration possible non-linear phenomena as core flux saturation. Nevertheless, without load, these would only happen at speeds higher than 12 000 RPM. The selected solution was to adopt coils with 20 turns, as this configuration (with a k_e of 22 V/kRPM) is closer to the k_e AMK value. Additionally, with 20 turns it is expected that the peak current to generate the maximum torque will be lower, as it decreases with the number of turns per coil.

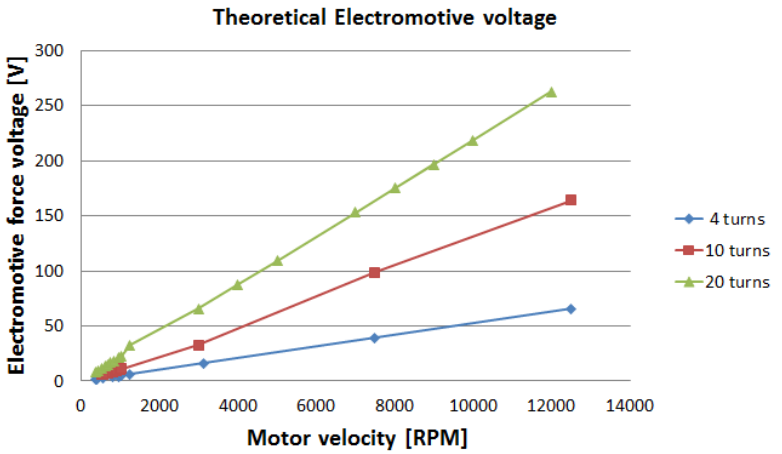

Figure 3.27: Variation of the theoretic BEMF peak voltage with the coils number of turns.

3.10 MJF performance characteristic

To draw the torque-speed and power-speed of the MJF motor (Figure 3.28), some considerations need to be taken into account:

1. The maximum torque simulated in Figure 3.26 is 20.682 Nm;
2. The speed where the BEMF is equivalent to the maximum voltage of the inverter (base speed) is 9000 RPM;
3. The maximum power of the motor happens at maximum torque when the motor is at base speed;
4. The power should be kept constant for higher speeds, where the torque decrease due to field-weakening to enable the motor to reach maximum speed - 12 000 RPM.

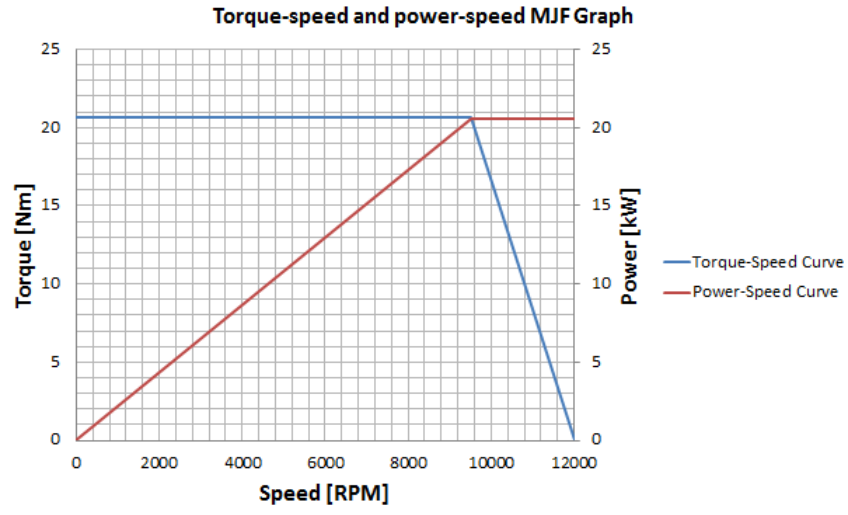

Figure 3.28: Torque-speed and power-speed theoretical curve.

Figure 3.28 shows the characteristic of the MJF motor that meet all the design requirements (20Nm, 20kW, 12000 RPM).

3.11 Motor efficiencies

The efficiency of electric machines is the relation between input and output powers. In a machine, during the conversion of electrical to mechanical energy, the energy losses represent the difference between the input and output.

As pointed out, there are different types of losses produced by distinct phenomena in the machine and those are influenced by various parameters. For example, Joule losses are highly influenced by torque; Eddy losses are highly influenced by frequency of the voltage waveform that is related to motor speed. The contribution of the different losses changes during the different working ranges of the motor. The efficiency map translates these contributions during all the working range of the motor. By measuring the input electric power and output mechanical power at different torque and speed points, it is possible to determine the efficiency in each state of the machine.

The overall efficiency of the machine takes a fundamental part in its thermal behavior, as lower efficiencies mean that the machine has higher losses and is producing more heat that needs to be removed. Furthermore, in case of a machine integrated in a car, where weight is a crucial parameter, the efficiency determines the amount of batteries (the capacity of the battery) the car requires. So a more efficient machine requires less battery capacity (and less battery weight) to have the same autonomy. In FS cars this aspect is even more crucial, because, when competing, all parameters can make a difference in the final result.

Efficiencies were calculated using Equation 3.16, Equation 3.17, Equation 3.18, Equation 3.21 and Equation 3.22. The total losses P_{total} take into consideration the Joule losses -P_{Joule}, Iron losses - P_{Iron}, and magnet losses - P_{Neod}, to calculate the efficiency - ϵ (Equation 3.22). The mechanical power - P_{mech} is the product of the torque in Nm times the rotation speed of the rotor in rad/s [42].

$$P_{total} = P_{Joule} + P_{Iron} + P_{Neod} \tag{3.21}$$

$$\epsilon = \frac{P_{mech}}{P_{mech} + P_{total}} \tag{3.22}$$

Figure 3.29 shows the efficiency map of the motor; it was drawn assuming a range of torque varying from 0 Nm to 20 Nm and the velocity varying from 0 RPM to 12 000 RPM.

As expected, the motor shows high efficiencies for higher velocities at nominal torque, around 5/6 Nm (Figure 3.29). At that region the constant losses, as for example mechanical friction, are less relevant as the mechanical power of the motor is high due to higher loads. It is also relevant to notice that for higher loads than the nominal torque, the efficiency begins to decrease, as the Joule losses become more relevant. The maximum theoretic efficiency is about 94.2 % at 9 000 RPM and 8 Nm. This efficiency map does not take into account the field-weakening and neither the power limitation, so some points with a velocity higher than 9 000 RPM will have less efficiency during the tests (field-weakening area), and working points higher than 20 kW will not be reachable (power limitation area).

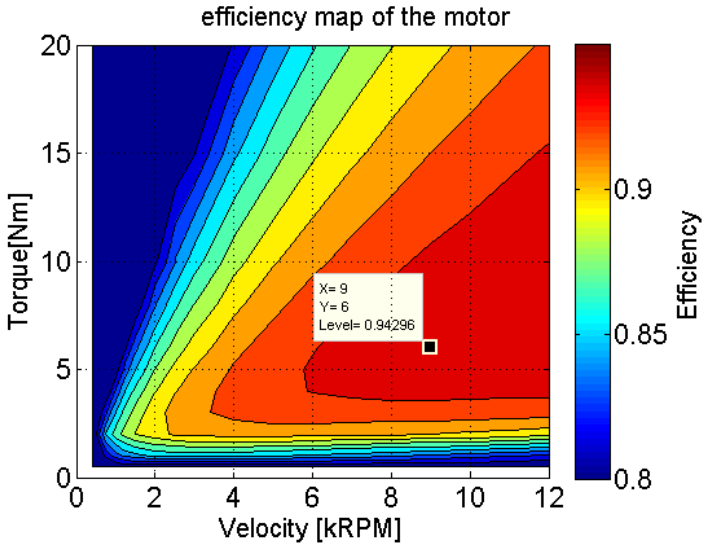

Figure 3.29: Predicted efficiency map of the motor.

3.12 Other motor components

3.12.1 Bearings

The bearings are responsible for maintaining the shaft and the rotor in the same radial and axial position, so that the air-gap between the rotor and stator does not change.

One of the main causes of motor failure happens because of bearings failures, so it is very important to analyse the bearing life, specially under load condition which is easily guaranteed when bearings have good dynamic operating characteristics over a wide range of speeds as well as low noise and vibration levels, minimized friction, high fatigue strength, less maintenance and long service lifetime.

A lot of different types of bearings are available in the market. In the past years, a new model of bearings started to be marketed by SKF, specific for high performance and efficiency electric machines. These bearing are made of ceramic, instead of the regular steel, which prevents spikes formation between the rotor and grounding, due to voltages potential different from zero. Furthermore, they are not influenced by induced currents created under high frequency and, as they work as electrical insulators, they prevent a DC current path through the rolling elements. These aspects also help increasing their own durability. In terms of mechanical properties, hybrid bearings (name for ceramic bearings) have higher grease life and create less friction. The hybrid solution was set as the first choice, but, due to a sponsorship setback, another solution was chosen.

In fact, to limit the cost, a standard ball bearing was selected. Several issues were taken into account: the high rotational speed it must handle, the high radial forces produced by the attraction between the magnets and the iron core, with grease sealed cap, and the guarantee of the geometrical limits of the caps.

For the motor prototype, the bearings selected were SKF 6201 with the specifications described in Appendix B.

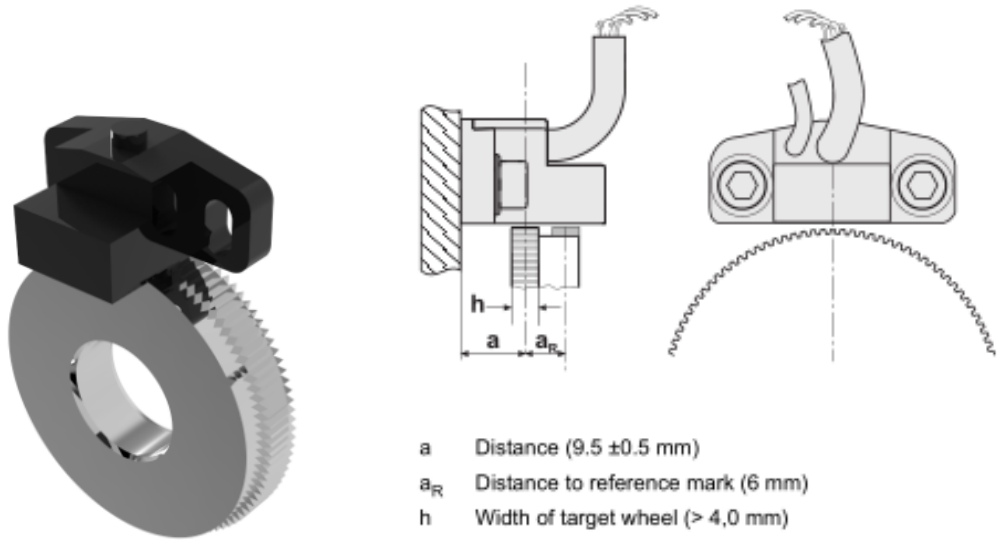

(a) Render of the MJF encoder.

(b) Schematic of the encoder [44]

Figure 3.30: Encoder that will be used in the MJF motor.

3.12.2 Encoder

The encoder is composed by a magnetic sensor and a spur gear attached to the shaft responsible for determining the position and velocity of the rotor to closed-loop controller. For the prototype, the encoder selected is the one used in the previous FST 05e car because it could work in very high speed (up to 40 000 RPM) and it was available in our stock (Appendix B).

3.12.3 Inverters and motor controllers

As it was said in the Technical Overview chapter, the inverter is not only responsible for inverting current DC to AC, but it is also responsible for controlling the motor. Therefore, the decision to continue to use a Synchronous permanent magnet motor, required the use of a proper control unit, capable of implementing field weakening or frequency control techniques, in order to achieve the best possible traction dynamic.

The requirements set for the motor and its design, depend highly on the selection of the inverter. For this prototype two inverters were taken into account, sharing many similarities as the final application was the same: Siemens and AMK inverters (Figure 3.31).

Siemens inverter was used during the tests. It was also used in the previous cars and it was available. The AMK inverter will be the one to be used in the car, as selected by the FST Lisboa team. The BEMFs, currents and frequency of the motor are defined according to the feeding ability of the inverters. The inverter's modulation is also important to consider as it affects the quality of the waveforms of the voltages and currents feeding the motor and its general performance.

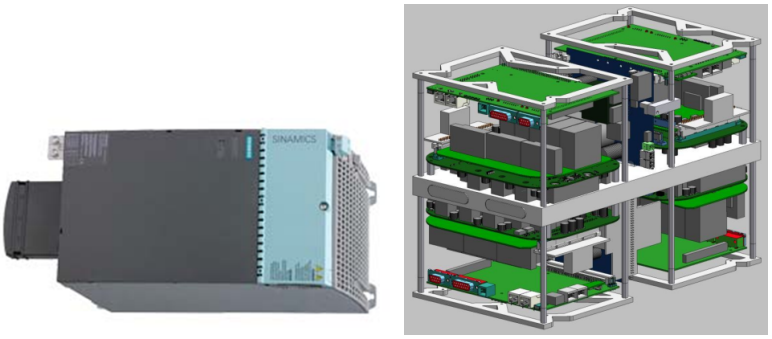

(a) Siemens inverter to be used during the tests.

(b) AMK inverter to be used in the FST 08e car.

Figure 3.31: Inverters to be used in different phases of the MJF motor.

3.13 Final Motor CAD

The final product of the motor prototype is presented as a CAD, after all the different design phases: materials and topology selection, manufacturing methods, requirements definition, winding optimization, electromagnetic optimization, mechanical and thermal analysis (Figure F.2). The CAD is a 3D picture of all the technical drawings and dimensions set for the motor, which means that, at this phase, it is possible to send all the pieces of the motor to be manufactured.

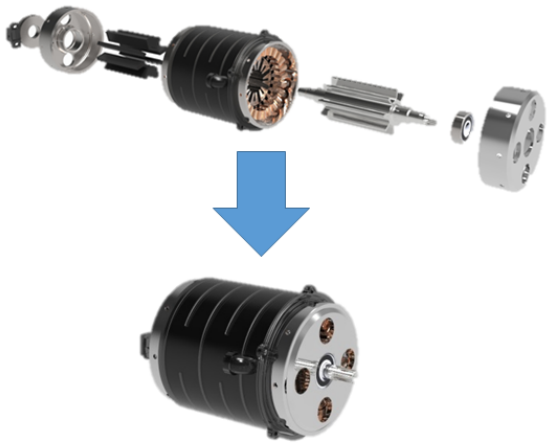

Figure 3.32: Render of the MJF motor CAD.

Chapter 4

Motor manufacturing

4.1 Initial Remarks

As stated, an electric motor is a system composed by many different pieces, each one with a specific task to fulfill. In the next chapter, the methods and approaches to fabricate these pieces are described.

The manufacturing process of the FST 08e motor prototype required hard working with the FST Lisboa team and involved some simplifications and high-tech approaches. In fact, in the fabrication of the prototype, the various machining operations needed to manufacture the motor components presented some difficulties and also demanded high degrees of accuracy.

The motor prototype version will work as a proof of concept to validate the most important manufacturing and assembling processes. So a more conservative approach was carried out. The main differences between the prototype and the motor final version will be the following:

- The core material used is Non-Oriented Silicon-Iron instead of HiperCo to reduce the price;
- Some simplifications in the machining processes were made in order to allow the manufacturing of the parts “in house”;
- Disassemble all the motor pieces must be possible in case of a problem, to visually analyse the working effects in all the components which lead to the failure; this design option caused to some decrease of the prototype’s performance.

The overall MJF motor costs are shown in Appendix F.

4.2 Motor Core

The material selected to the magnetic core of the stator and rotor was the NO20. This Non-oriented material, with 0.20 mm thickness, has already a special coating called BackLack on both sides. The material was cut with laser to the desired geometry. After that, the 400 laminations of the rotor and stator were assembled, with a stacking factor due to the varnish of 97%.

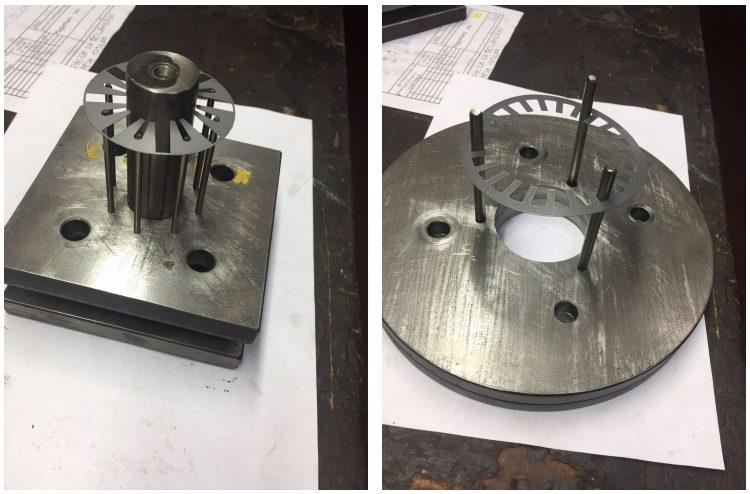

(a) Rotor Laminations. (b) Stator Laminations.

Figure 4.1: Magnetic core of the MJF motor.

Two moulds were used to construct the stacking (Figure 4.1). A tool was used to press the laminations together during the heat treatment in order to keep the pressure constant. Taking into account the most critical aspect of the shape, for example, in a stator the inner diameter, a guide between the slots was done to align the laminations. The outer diameter of the stator was grinded.

After stacking, both pieces were submitted to a heat treatment with stable pressure. A particular heat cycle, which reached approximately 200°C, was considered, in order to increase the magnetic properties of the material, which decreased during the cutting process, and also to fix all the laminations together. Figure 4.2(a) shows the stacking of the stator after the process. It is possible to notice that the stacking has some misalignment between the sheets, which difficults the assembly of the stator in the housing and, most importantly, worsens the contact between both, decreasing the efficiency of heat transfer and increasing the overall motor temperature. In this case, the stacking was not grinded but, in future versions, this can be made according to the manufacturer.

(a) Motor Stacking. (b) Rotor and stator stacking.

Figure 4.2: MJF motor stacking.

Figure 4.2(b) shows the stator and rotor stacking of the motor; their total weight is 2.394 kg, less 0.513 kg than those of the CAD motor. This 21% deviation is mainly due to the fact that in the CAD motor all the stacking is one entire piece, without varnish.

4.3 Motor housing

In this project, the motor housing is composed by three pieces, a main stator jacket and two covers to be attached by bolts to the jacket Figure 4.3(a). For a motor spinning at such high speeds as this one, the final tolerances between all the different parts is crucial, as a misalignment between the covers that support the bearings will lead to a shaft vibration and a potential failure. A housing with only a jacket as a cup and only one cover would be more recommended as it would be easier to assure the concentricity tolerance between the two pieces. Nevertheless, this solution would be very difficult to manufacture “in house”.

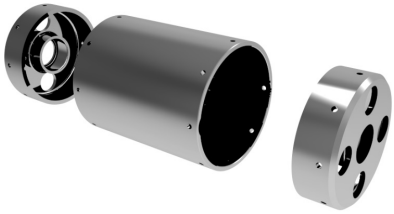

(a) Motor housing CAD.

(b) Jacket drilling.

(c) Jacket turning.

(d) Jacket after manufacturing.

Figure 4.3: Motor housing.

The stator jacket was the most challenging piece to manufacture. A method was developed using a drill to do the keyway to prevent the spinning of the stator inside the jacket (Figure 4.3(b)), and turning

to reduce the jacket diameter as well as to manufacture the interior of the jacket (Figure 4.3(c)). Figure 4.3(d) shows the final jacket; weighing 0.499 kg, it has 46 grams more than the motor CAD (10% deviation).

4.4 Winding

The winding process was developed to conduct the preliminary motor test. This process consisted on:

1. To stretch several copper wires (according to the number of wires in parallel) with the length of one phase (each phase has 4 coils)- Figure 4.4(a);
2. To curl the 4 coils, each one with 4, 10 or 20 turns, using the wood mould with the dimensions of the slot - Figure 4.4(b);
3. To insert the phases into the slots in the stator - Figure 4.4(c).

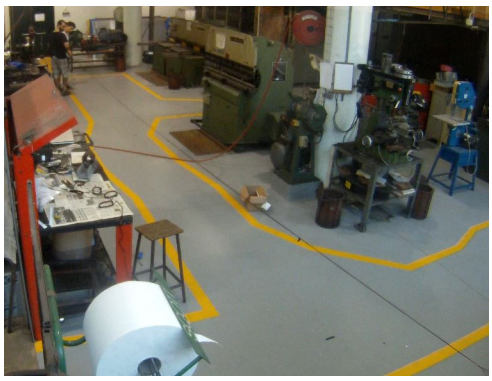

(a) Stretch of copper wires in parallel.

(b) Coils curl.

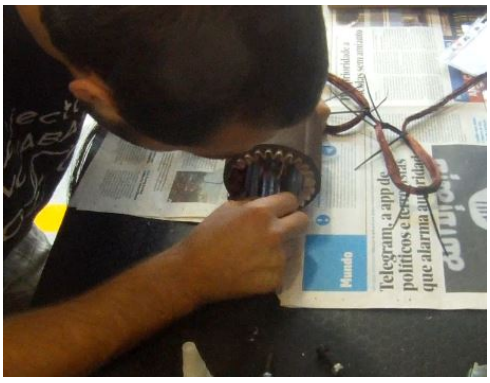

(c) Insertion of the phases.

Figure 4.4: Winding process of the MJF motor.

After the coil tests were done, the winding was carried out at a professional company called Lehmus (Figure 4.5).

Figure 4.5: Winding carried out by Lehmus.

4.4.1 Surge test

A surge test is a type of High potential test (Hipot) to verify electrical insulation. A voltage is applied during a very short period of time between two phases to compare both impedances. The shapes of the surges are superposed and if they are not identical it suggest an insulation fault due to turn to turn short circuit, coil to coil short circuit, phase to phase short circuit or phase to ground short circuit (Figure 4.6(a)).

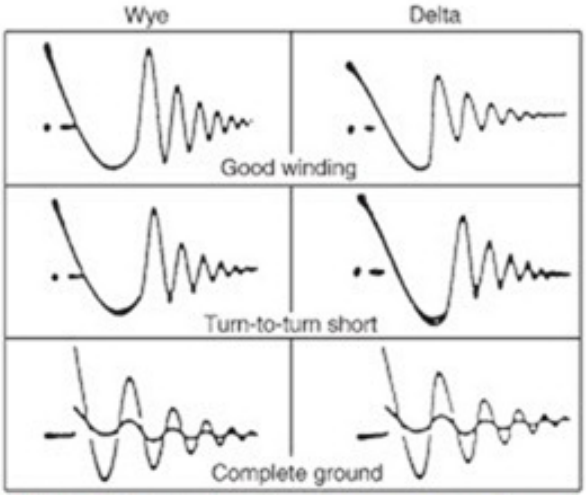

(a) Possible results in a surge test.

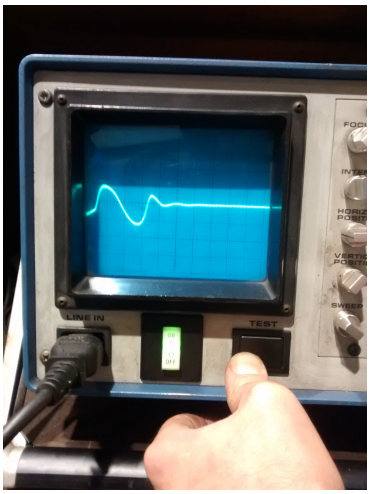

(b) Surge test done at Lehmus.

Figure 4.6: Surge Test.

This test was done in Lehmus after the motor winding to verify that no damage to the insulation was done during the process and to assure reliability (Figure 4.6(b)). This kind of test can also be done to prevent major failures from happening, as a preventative maintenance tool to detect insulation weakness that reduces dielectric strength due to aging.

4.5 Motor assembly

The motor assembly consists on the insertion of the rotor in the stator and on mounting all the bearings and housings of the motor. As the rotor of this motor has permanent magnets that generate high forces over the stator during the motor assembly, a special procedure was carried out. This procedure used a lathe in order to ensure the concentricity while the rotor is inserted in the stator and consists on:

1. Motor housing with back endplate holding in the chuck of the lathe (the bearing must be already on the endplate) - Figure 4.7(a);
2. Shaft, bearing and front endplate mounting plus holding in the tailstock - Figure 4.7(b);
3. Rotor insertion in the stator by moving the tailstock - Figure 4.7(c);
4. After the rotor is in the stator, disconnections of the shaft from the tailstock and of the motor from the chuck - Figure 4.7(d).

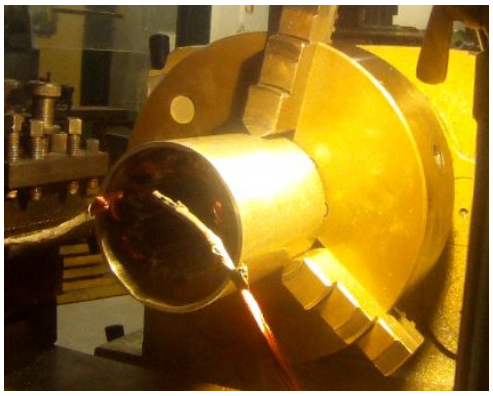

(a) Fixation of the motor housing in the chuck.

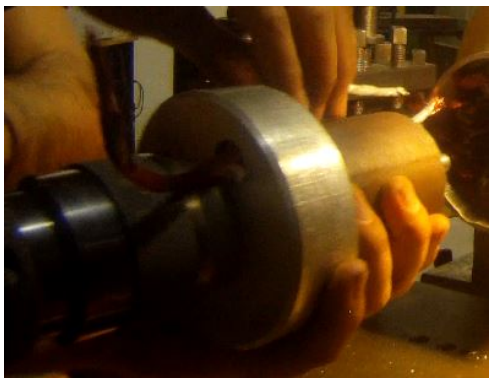

(b) Fixation of the shaft+bearing+front endplate in the tailstock.

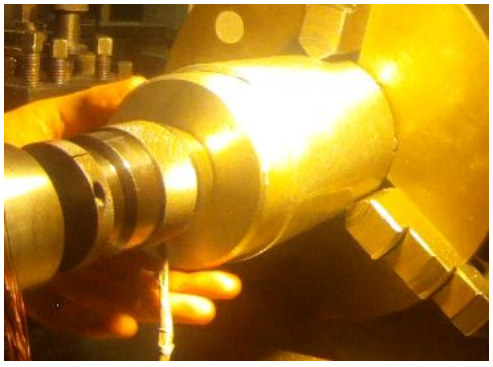

(c) Insertion of the rotor in the stator.

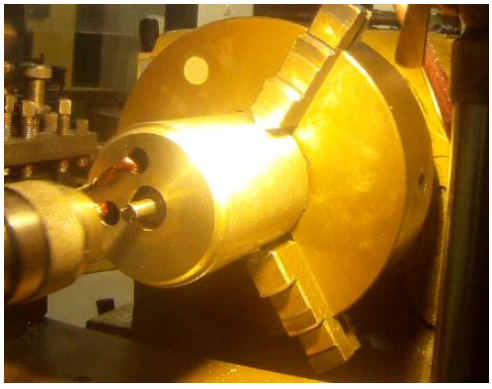

(d) Final detachment.

Figure 4.7: Motor assembly procedure.

4.6 Final Assembly

Figure 4.8 shows the motor prototype final winding assembly (made by Lehmus company), being the results of the overall procedure and motor testing shown in the next chapter.

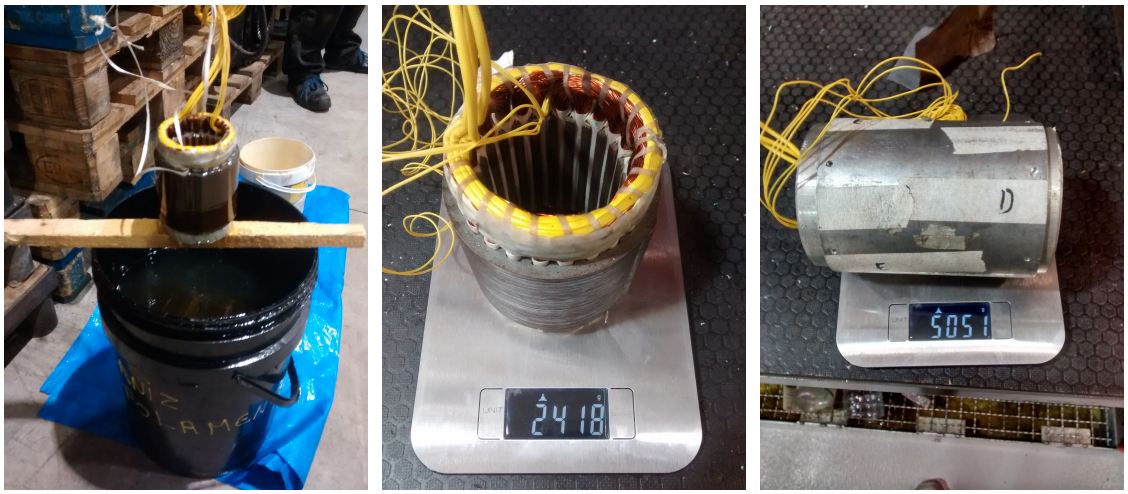

(a) Winding coating. (b) Stator weight. (c) Total motor weight.

Figure 4.8: Motor prototype - final assembly.

4.7 Test-bench design and manufacturing

In order to conduct the tests for the velocity, torque, power, efficiency and endurance, a test-bench was built. This test-bench was composed by two electric machines, the MJF motor and a Siemens motor used as a generator mechanically attached by two transmission boxes (one 4:1 and other 1:20, which gives an final ratio of 1:5). The generator was connected to a rectifier that was connected to a load. The motor was connected to a battery through an inverter. A schematic of the test-bench is represented in Figure 4.9.

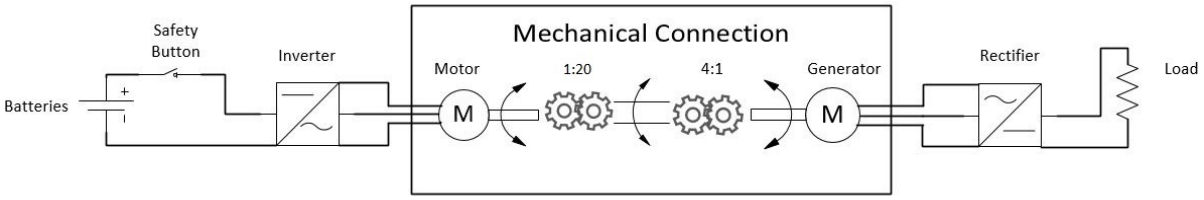

Figure 4.9: Schematic of the test-bench.

Figure 4.10 shows the diagram of the connections of the test-bench. A computer (PC1) is connected by Ethernet to a Control Unit (CU) which is responsible for managing the connections between the computer and all the other units, i.e., two motor controllers and one terminal module (TM). The first motor controller, connected to the MJF motor, is fed by a 600 V DC power supply and modulates the waves using IGBTs that makes the motor spin. The second motor controller, connected to the Siemens

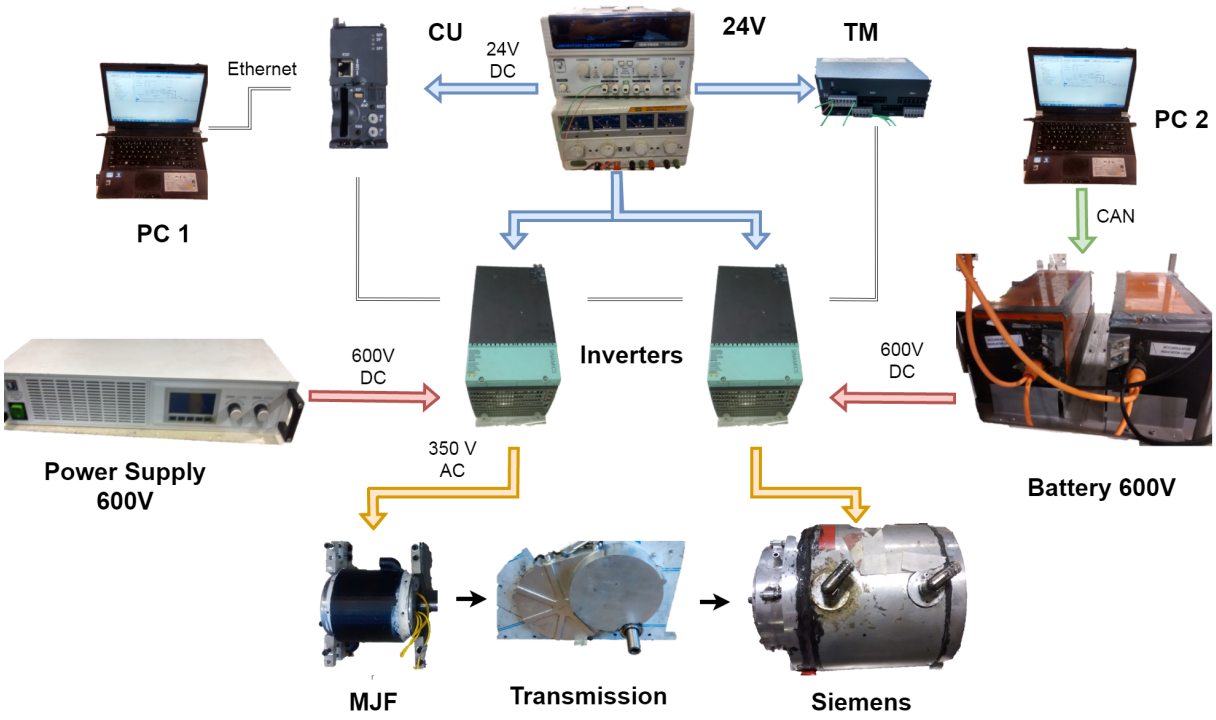

Figure 4.10: Test-bench diagram for the MJF tests.

generator, converts the waves coming from the generator to DC which feed and charge the batteries. The TM manages analogical and digital signals inputs. All these modules are fed with 24 V DC.

To ensure that the motor shafts are aligned, their supports as well as the gear transmission boxes supports were manufactured by waterjet cutting - Figure 4.11.

To connect the MJF motor to the transmission box, one coupler was developed and manufactured.

The test-bench design was iterated several times mainly because the pieces designed for the previous prototypes took more time to manufacture than the available. At the end, the design presented on Figure 4.12 was fully assembled.

(a) Support pieces after waterjet cutting.

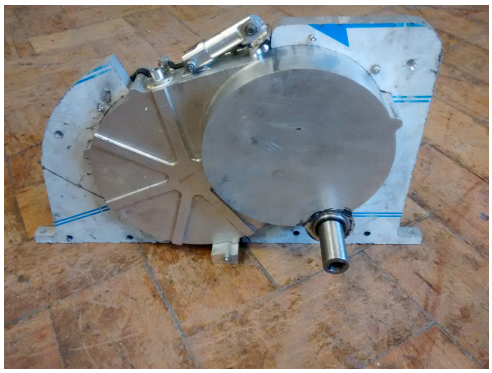

(b) Transmission box and supports.

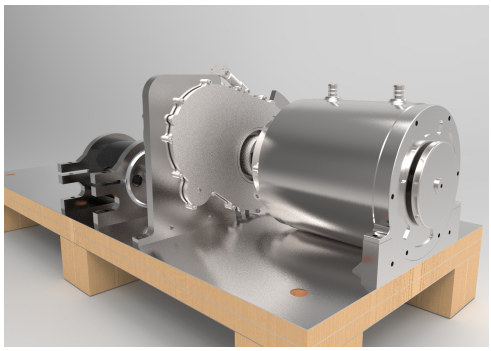

(c) Test-bench render.

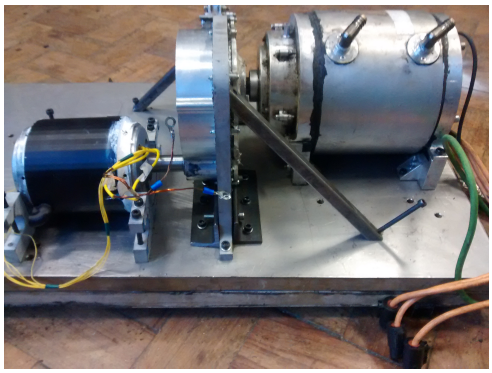

(d) Test-bench photograph.

Figure 4.11: Test-bench pieces.

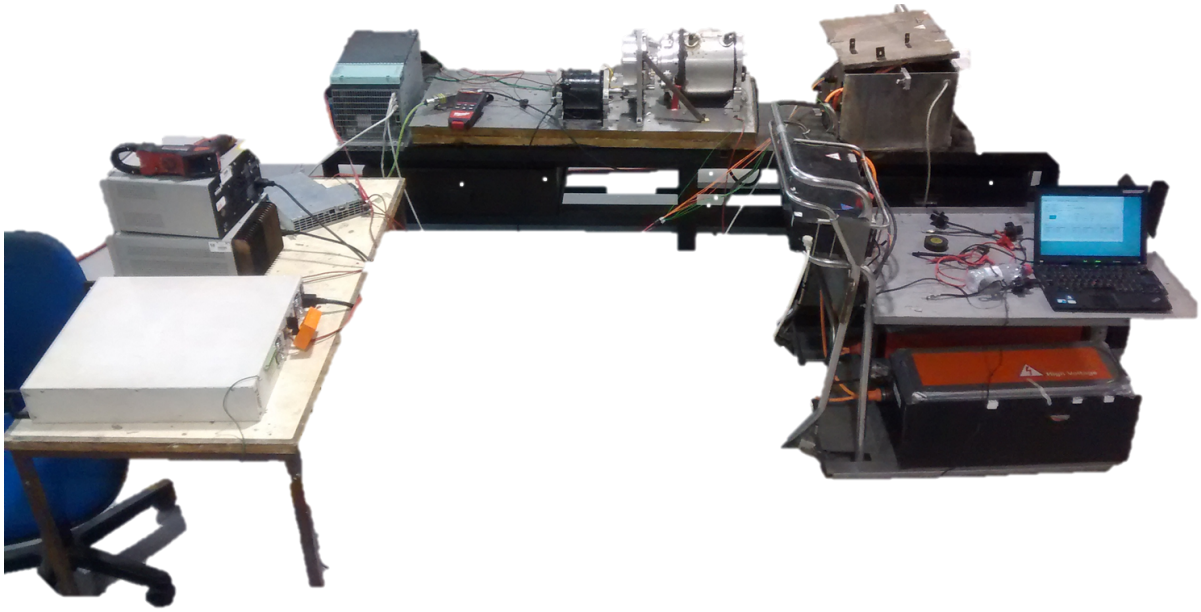

Figure 4.12: Final test-bench.

Chapter 5

Motor testing

5.1 Introduction

Physical tests are performed to validate the theoretical models, so that the accuracy of the defined requirements and specifications are proven. The theoretical models have associated errors and, additionally, the way of processing the calculations and the assumed simplifications also have an impact on the final product.

Furthermore, the characteristics of the final product change during the manufacturing process and the assembly of the machine is subjected to manual procedures that depend highly on the experience of the technician and manufacturer.

Tests in electric machines are intended to measure the final parameters in a test-bench, as for example: the nominal and maximum power, the torque, the speed, the current and voltages, the insulation resistance and the efficiency. To perform those tests, normally a dynamometer must be connected to the machine shaft by a coupling system; transmission boxes must be avoided to obviate interference with the results. Besides, many different test-benches must be used during the testing process as for example special rigs having temperature chambers, humidity chambers, destructive protection, vibration beds, etc, together with many different sensors to do the distinct measurements.

There are certifications that electric machines manufacturers must comply before selling their products and specific tests under pre-defined conditions have to be conducted. Some of those are very demanding and rigorous and could not be considered under the scope of this work: first, due to the facilities and the material limitations, and secondly, because in FS, the motor will not perform more than 1000 kilometers or 300 minutes of work during all its lifespan. Therefore, FS cars' motors, which work under this limited range of conditions, do not require some of the tests normally carried out.

A transmission box (in fact two of them) were used because a dynamometer was not available at the laboratories of FST Lisboa team. Also, an electric machine of the previous car was used as load. This set, proved to be able to successfully acquire most of the required data but it also showed some limitations. In fact, it revealed not to be the ideal solution to fully characterize the machine but it was the best solution given the available resources. Accordingly, as a recommendation, it is suggested to

conduct in the future more rigorous tests with a dynamometer instead of a transmission box and with more sensors to acquire data.

In this work, the most relevant tests to determine the defined motor parameters were: i) motor number of turns per coil, ii) maximum velocity, iii) maximum torque, iv) maximum power, v) nominal performance during endurance simulations and vi) efficiency.

The first test was done to validate the number of turns per coil that match the BEMF imposed by the inverter without exceeding the maximum temperature of the motor. The second test was done to see if the rotor could withstand the centrifugal forces at maximum velocity and also to analyse if the voltage induced in the phases of the motor matched the calculated BEMF. To validate the torque, a third test was conducted; during this test the goal was to see if the motor was capable of producing the designed torque, without saturating the core and without exceeding the maximum current of the inverters. Knowing the maximum velocity and torque, the next test was carried out to validate the maximum power of the motor without exceeding the maximum temperature of 80°C. Posteriorly, an endurance test at nominal performance was done to validate the working range parameters of the motor during 25 minutes and to validate the behavior of the cooling system. At last, a test was made to determine the efficiency of the motor at different speed and torque points.

5.2 Motor number of turns per coil

5.2.1 Introduction

During the construction of the motor, the coils distribution and parameters needed to be set. To do so, experimental tests were done with just one phase, in order to determine the BEMF created by different coil distributions and the thermal behavior of the system. The decision of testing just one phase at a time was chosen taking into account the time available to do all the tests with different distributions. In fact, with the results of the test using just one phase, it is possible to extrapolate, with low errors, the results for 3 phases.

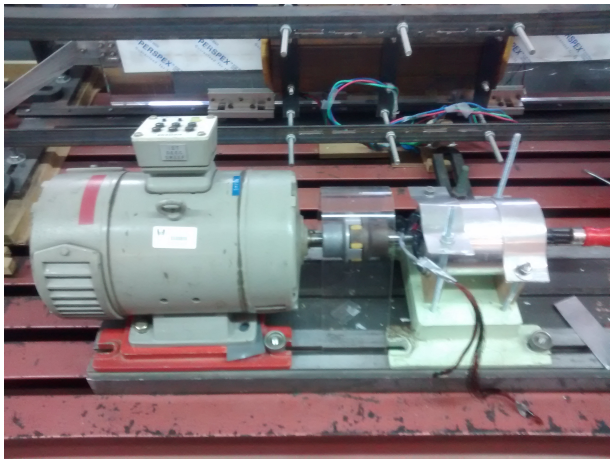

Figure 5.1: Experimental test-bench used to determine number of turns per coil BEMF.

To test the BEMF of the motor, a primary experimental test-bench was assembled (Figure 5.1), where the MJF machine worked as a generator attached to a DC motor responsible for making the MJF spin. Different speeds were selected and the BEMF voltage was registered (Figure 5.2(b)).

A graph of the BEMFs versus rotor speeds in RPM of the synchronous motor used in the previous car is shown in Figure 5.2(a). According to this graph, one can expect to have a maximum supply AC voltage on the motor terminals of 380 V peak, from base speed to the maximum motor speed, which, in that Siemens machine, is 6 500 RPM. The objective is to use the same inverter to feed the MJF motor during the tests, and so, the maximum voltage that the inverter can apply to the motor has an amplitude of 380 V peak. Supposing no saturation of the magnetic core, the graph of the MJF motor should have the same linear tendency, but with the line intersecting 380 V peak, at the base speed of the motor. The BEMF graph shows the linear relation between the voltage and speed, also known as the voltage constant (ke), when no load is applied.

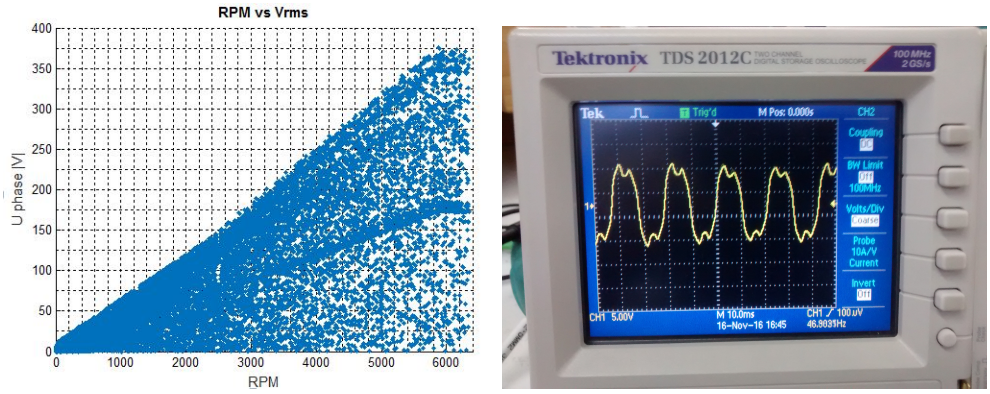

(a) BEMF Root Mean Square (RMS) voltage (or Ke graph) of the Siemens motor.

(b) BEMF voltage MJF characteristic.

Figure 5.2: Ke linear graphs.

Figure 5.2(b) shows the characteristic of the BEMF of the motor. As stated previously, it shows merely the content of odd harmonics. The Ke graph was primarily calculated based on theoretical equations and then verified experimentally. To do so, three different one phase winding configurations were tested: 4, 10 and 20 turns per coil.

The cable diameter used in all tests was the same as well as the number of coils and configuration between the coils, which were in series, changing only the number of turns per coils.

Increasing the number of turns per coil augments the BEMF or induced voltage of the motor, but it also increases the phase resistance and the temperature by Joule losses on the coils. The practical measured results are show in in Figure 5.3(a). After that, an extrapolated graph - Figure 5.3(b) - was made in order to determine the BEMF values at the maximum velocity of the MJF motor. This method was used as the velocity of the MJF is much higher than the DC motor and it was not possible to test higher velocities. The extrapolated graph is an approximation and does not take into account the saturation of the core material. The measured and extrapolated values of the induced voltage correspond to one phase, so, to get the values of three phases shown in Figure 5.3, the values in the represented graphs were multiplied by $\sqrt{3}$.

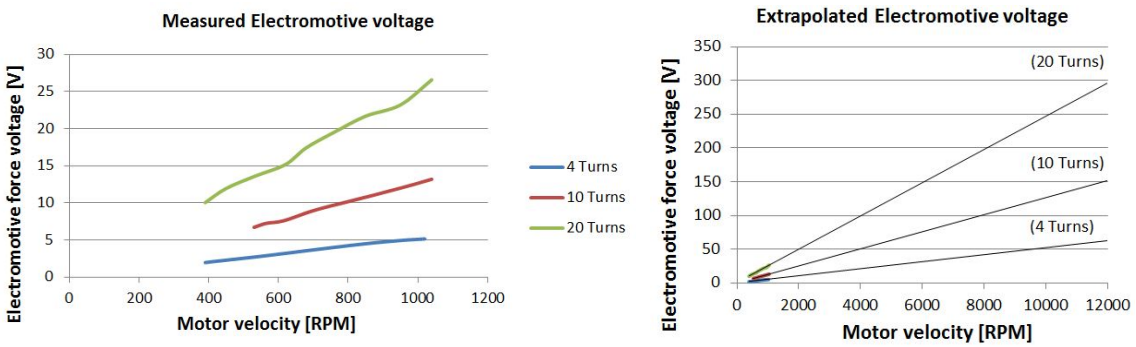

(a) Induced voltage measure.

(b) Induced voltage measure.

Figure 5.3: Induced voltage tests of one phase.

According to the graph presented in Figure 5.3(b), one can see that, for the nominal velocity of 9000 RPM, coils with 4 turns induce 50 V peak, coils with 10 turns induce 120 V peak and coils with 20 turns induce 220 V peak. All the solutions met the requirements as they do not exceed the 380 V peak the inverter is capable to delivering. However, the configuration that fits better the induced voltage requisites is the one with 20 turns, as it induces 230 V peak at 9000 RPM. Furthermore, this configuration presents a voltage constant (ke) more similar to the one of the AMK motor (18.8 V/kRPM) - Appendix A. Note that this voltages values are without load, so the terminal total induced voltage will be the BEMF seen here plus the voltage drop in the windings when a load is applied. 220 V peak is supposed to give enough room to ensure that the terminal induced voltage of 380 V peak will only be reached at full load and at base speed. The respective voltage constants are: 5.5 V/kRPM, 13.3 V/kRPM and 25.5 V/kRPM. Thermal tests to all these three solutions were conducted to validate the heat production of the MJF motor (see next sub-chapter).

5.2.2 Temperature Testing

In order to compare and validate the errors of the theoretical thermal simulations, some temperature tests - Figure 5.4(a) - were made using the one phase winding configuration shown in the last sub-chapter. In these tests, the rotor was blocked and the winding was fed with different amplitudes of sinusoidal currents, to assess the influence of the increment of Joules losses and its relation to the motor temperature. The amplitudes of the currents used on the tests were similar to the current values expected to produce nominal torque in the motor. Four sensors were placed in different points of the motor - Figure 5.4(b):

1. Sensor 1: In the middle of the coil, inside the slot;
2. Sensor 2: In the coil extremity;
3. Sensor 3: In the rotor periphery;
4. Sensor 4: In the exterior housing.

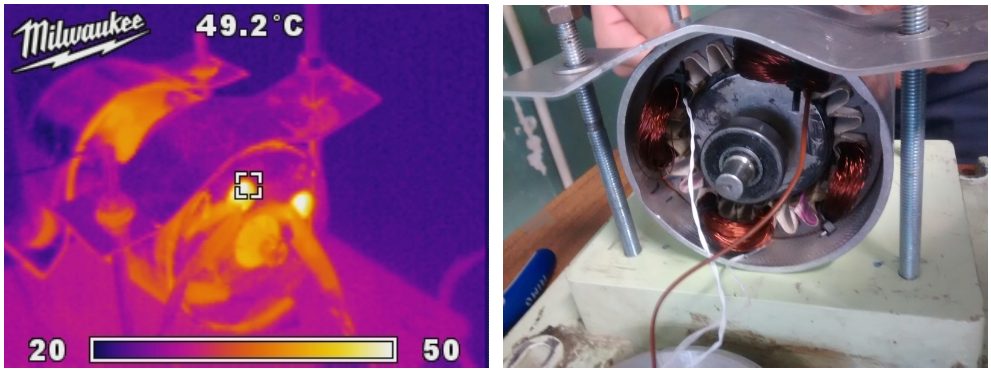

(a) Motor thermal photo in the end of the test with 10 turns at 15 A.

(b) Sensors location in the motor.

Figure 5.4: Thermal tests of the MJF motor.

Two models were developed to calculate the temperatures in different parts of the motor: one using excel, to calculate the winding temperature and the other, developed by Pedro Fontes [13] , to estimate the temperatures over time.

The maximum time of the test was 30 minutes because the motor is not supposed to continuously work more than this duration. In fact, this is the maximum time the battery can feed all the four motors of the car.

Four winding configurations were tested, with different current amplitudes:

- 30 copper conductors in parallel (10 turns per coil) with 15 Amperes;
- 15 copper conductors in parallel (20 turns per coil) with 10 Amperes;
- 15 copper conductors in parallel (20 turns per coil) with 15 Amperes;
- 15 copper conductors in parallel (20 turns per coil) with 20 Amperes;

Figure 5.5 and Figure 5.6 show the results of the temperature in the coil extremity and in the rotor of the tests carried out for the two first configurations (30 copper conductors in parallel with 15 Amperes and 15 copper conductors in parallel with 10 Amperes, respectively). The temperatures acquired with the sensors located in the centre of the winding and in the rotor are shown in Appendix G.

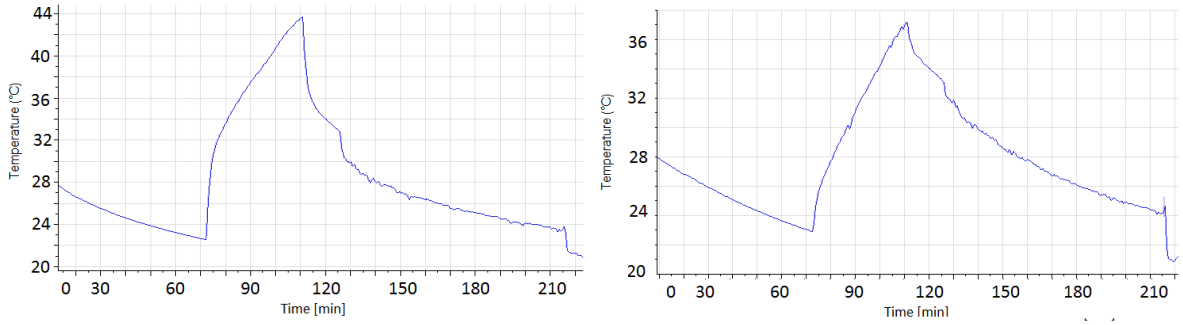

(a) Temperature in the coil extremity.

(b) Temperature in the rotor.

Figure 5.5: Thermal test of the motor with 10 turns at 15 amperes.

In Figure 5.5, the maximum temperature registered in the coil extremity was 44°C and 37°C in the rotor, after 30 minutes. The results are way below the maximum temperature limit of 80°C.

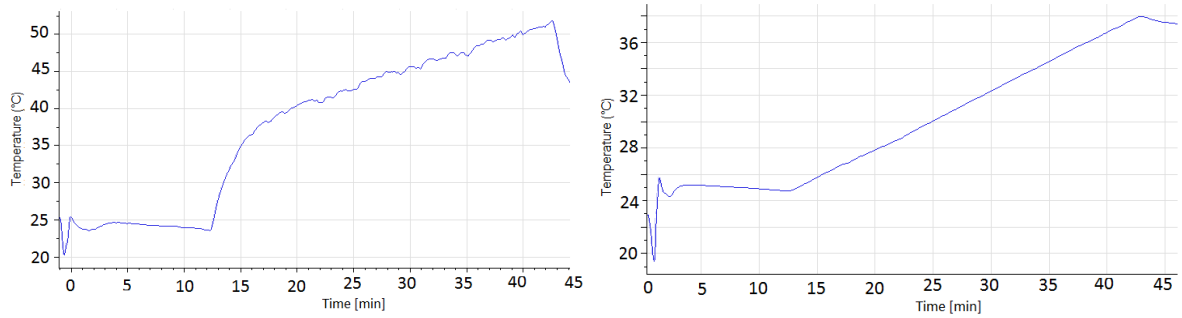

(a) Temperature in the coil extremity.

(b) Temperature in the rotor.

Figure 5.6: Thermal test of the motor with 20 turns at 10 amperes.

With a new winding configuration (coils with 20 turns), Figure 5.6 shows that the maximum temperature was 55 °C, in the coils extremity and 38°C, in the rotor, concluding that the motor can handle higher currents.

For the last two configurations, the approach carried out was: i) a first test was done, ensuring a current of 15 Amperes during 10 minutes (Figure 5.7), ii) a second test was carried out right after, in order to prevent cooling down, ensuring 20 Amperes.

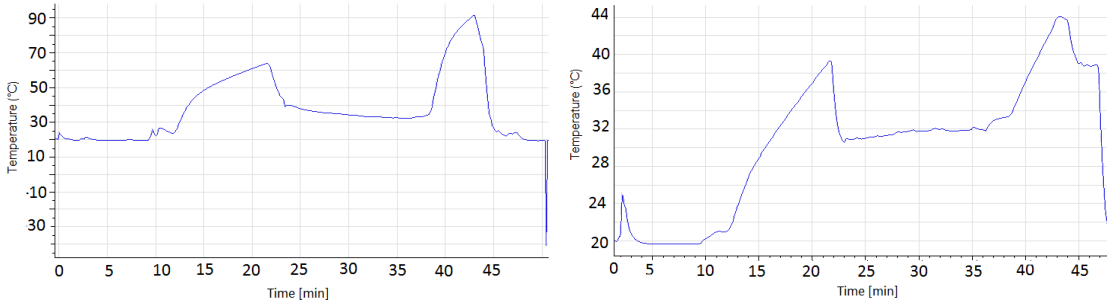

(a) Temperature in the coil extremity.

(b) Temperature in the rotor.

Figure 5.7: Thermal test of the motor with 20 turns at 15 and 20 amperes.

The test with 15 Amperes took about 11 minutes due to a supply problem, because the transformer fuse did not handle the current. Although, tracing the temperature tendency of the extremity of the coil and rotor, it is possible to say that the temperature was bellow 80°C at the end of 30 minutes.

During the test with 20 Amperes, at minute 5, the temperature of the coil in the center of the slot reached 120°C. This is the maximum temperature the sensors can measure and the test was shut down. The maximum temperature the motor can withstand is 180°C in the windings and 80°C on the rotor, although to prevent any demagnetization problem, the MJF maximum temperature, during continuous work, is set to be 80°C. So, it is possible to conclude that the motor cannot withstand 20 Amperes, without a cooling system.

Table 5.1 presents the results of the temperature tests carried out for the 5 configurations analysed. Note that the different FEA were made in stationary mode which means that the temperature results

refer to a much larger time than the 30 minutes. The errors of the Excel and the FEA were calculated in relation to the experimental tests values.

Table 5.1: Thermal results.

	Excel [°C]	FEA [°C]	Test [°C]		Error Excel [%]	Error FEA [%]
10 turns / 10 A	34,4	34,8	35,5		3,1	2,0
10 turns / 15 A	46,3	42,1	49		5,5	14,1
20 turns / 10 A	62,8	52,4	60		4,6	12,7
20 turns / 15 A	110,0	132,0	99,6*		—	—
20 turns / 20 A	176,1	220,0	120,7**		—	—

* test ended at minute 11 due to the energy supply problem

** test ended at minute 5 due to the high temperature of the sensors - 120 °C.

5.2.3 Extrapolation to 3 phases motor

After having validated the two thermal models shown previously for one phase, it was possible to extrapolate the temperature values to the same motor, but now with 3 phases (Table 5.2). These values were used only as a prediction of the temperatures to deal with, because it is not possible to know “apriori” the value of the associated errors.

Table 5.2: Maximum motor temperature when extrapolating to 3 phases.

	Excel [°C]	FEA [°C]	FEA with cooling system [°C]
5 A	53,3	46.5	—
10 A	138	98.5	—
20 A	478	304	66.3

The cooling system for the motor was studied and designed in Pedro Fontes’s thesis [13].

5.2.4 Coil test conclusions

With these preliminary tests it was concluded that the number of turns per coil should be 20. Even if the usable section of copper wire reduces, due to the increase of coil turns, the cooling system should be enough to dissipate the heat from the motor, assuring that, during the 30 minutes of continuous work, it will not reach 180°C, in the coils, and 80°C, in the magnets.

Based on the thermal models, it was also possible to prove that the power of the motor is around 5 kW without a cooling system, reaching 10 kW (nominal power) with the cooling system installed. It is important to say that these values are valid only if the motor works for periods no longer than 30 minutes, otherwise the nominal power will be inferior.

5.3 Maximum velocity testing

After the final configuration of the motor was selected and manufactured by professionals, a test regarding the motor maximum velocity was made. This test had two goals: i) to analyse if the motor’s rotor

could withstand the high centrifugal forces created by the high rotation speed of the rotor, ii) to validate the BEMF values and voltage constant (ke) without load.

The maximum velocity reached on the tests was 11750 RPM. Figure 5.8(a) shows the maximum velocity on the Siemens motor, which multiplied by the final transmission result, gives the MJF motor maximum velocity (Figure 5.8(b)). It was not possible to reach 12000 RPM because the Siemens Software has a security measure that prevents the motor of reaching the maximum velocity set by the user during the parameters configuration. Nevertheless, this result showed that the MJF motor is capable of performing the maximum velocity set in the design goals.

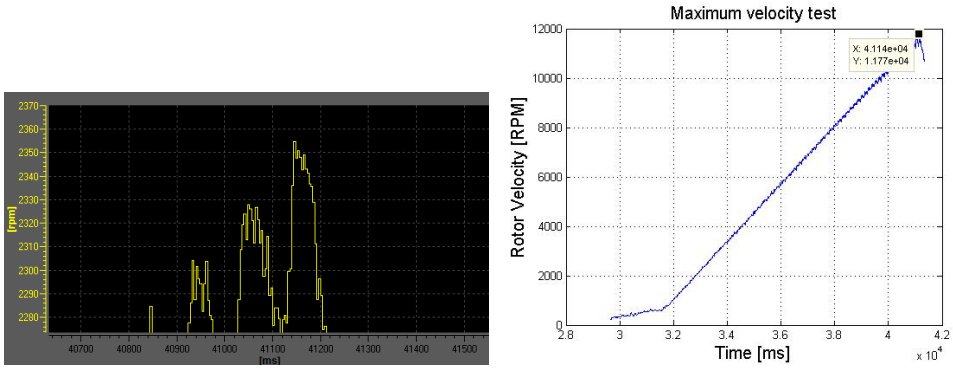

(a) Siemens generator output.

(b) MJF generator output.

Figure 5.8: Maximum velocity recorded during testing.

In this test it was also possible to evaluate the successful behavior of the motor at such a high speed, the temperatures due to Eddy losses, the control of the motor and the rotor balance - Figure 5.9.

With the same data of Figure 5.9, it was possible to determine the voltage constant Ke (Table 5.3).

Table 5.3: Voltage Constant Ke

Velocity [RPM]	Peak Voltage [V]	Ke [V/kRPM]
3000	70	23.3
6250	150	24
7000	170	24.3
10000	240	24

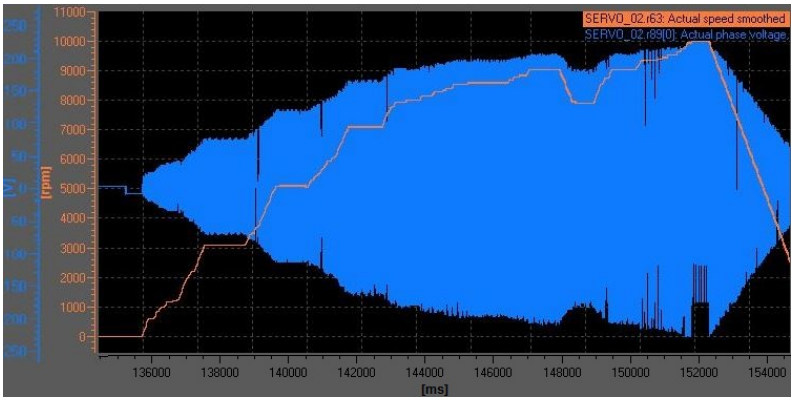

Figure 5.9: Voltage vs RPM during maximum velocity test without load, (orange - velocity [RPM] and blue - induced voltage [V].

As a conclusion, a value of 24 V/kRPM is defined for the voltage constant of the motor running without load.

The complete graph acquired during this test is shown in Appendix G.

5.4 Maximum torque testing

To measure the real torque of the MJF motor, it was decided to use the Siemens machine as load because this is well parameterized in the Siemens Software, ensuring that the measurements have fewer errors, especially regarding torque, which is estimated based on the field current, and torque constant [Nm/Arms]. However, this topology is subjected to other type of errors, namely regarding friction forces in the transmission. These forces oblige the MJF motor to do a little more torque which is not modulated. So, by considering the MJF torque equal to the Siemens generator motor divided by the transmission relation, one adopts a conservative approach in what concerns the maximum torque value. The velocities achieved during the test were 400 RPM, for the MJF motor, and 80 RPM, for the Siemens generator.

Figure 5.10 shows the torque measured in the Siemens machine. This torque is negative as it is set to contradict the MJF torque. Dividing the maximum value (around 100 Nm) by the total transmission ratio (1:5), the maximum torque value of the MJF motor will be around 20 Nm.

Due to the test-bench limitations regarding the maximum torque (for the Siemens machine this value is equal to 100 Nm, which, once divided by the gear ratio, limits the maximum value to 20Nm), it was not possible to further increase the torque. Nevertheless, one can say that the MJF motor will be able to generate more torque according to the results showed in Figure 5.10 as no saturation was noticed and no overheat was recorded.

It is now possible to calculate the torque constant of the motor. Figure 5.11 represents the phase current of the MJF motor during the test. When the motor is generating 20 Nm, the maximum current is about 50 A (the peaks are not considered as they represent noise), the Kt is 0.4 Nm/A, compared to

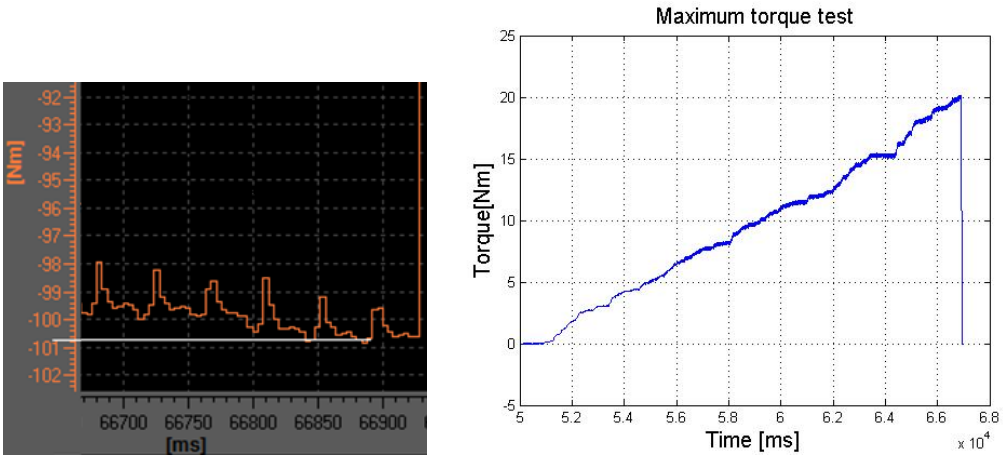

(a) Siemens generator output.

(b) MJF motor output.

Figure 5.10: Maximum torque recorded during tests.

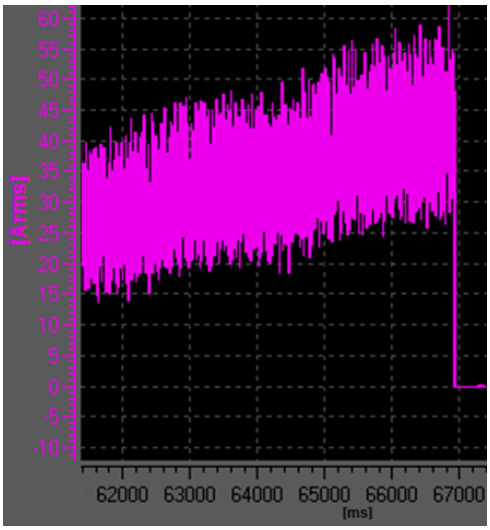

Figure 5.11: MJF motor torque generating current.

0.26Nm/A of the AMK motor - Appendix A. This means that less current is required to produce the same torque, so this is expected to reduce the Joule losses.

The complete graph acquired during this test is shown in Appendix G.

5.5 Maximum mechanical power testing

Maximum power test was performed during 30 seconds. Power estimated by the inverter (pink), torque (orange) and velocity graph (yellow) are shown in (Figure 5.12), note that torque and velocity were measured in the Siemens machine and must be multiplied and divided, respectively by the gear ratio 1:5. One can conclude from Figure 5.12 the following items:

1. The average value of maximum power was around 12.5 kW during 30 seconds;
2. The power graph, as expected, has a lot of oscillations from 8 kW to 22 kW. This phenomenon is a characteristic of spoke topology motors and happens due to the high reluctance variation of the rotor which produces torque ripple;
3. When the motor reached a velocity around 6000 RPM with 16 Nm, the inverter started working in field-weakening, so at that point, the induced voltage at the terminals was 380 V peak. This can be seen because the power graph does not have values from 5 kW to 7 kW, due to the incapacity of the inverter to determine that values during this state.
   The complete graph acquired during this test is shown in Appendix G.

As it will be pointed out in the Final Considerations chapter, to test the motor with more power, a new test-bench must be used (capable of feeding 20 kW) and the number of turns per coils must decrease to 10 (decreasing the voltage induced at the terminals and enabling the motor to reach higher speeds). Regarding the thermal behavior, the motor windings reached only 80°C at the end of 30 seconds, showing room to further increase the power of the motor, to the defined 16 seconds goal for 180°C. Notice that the motor was stopped after 30 seconds because the temperature in the rotor

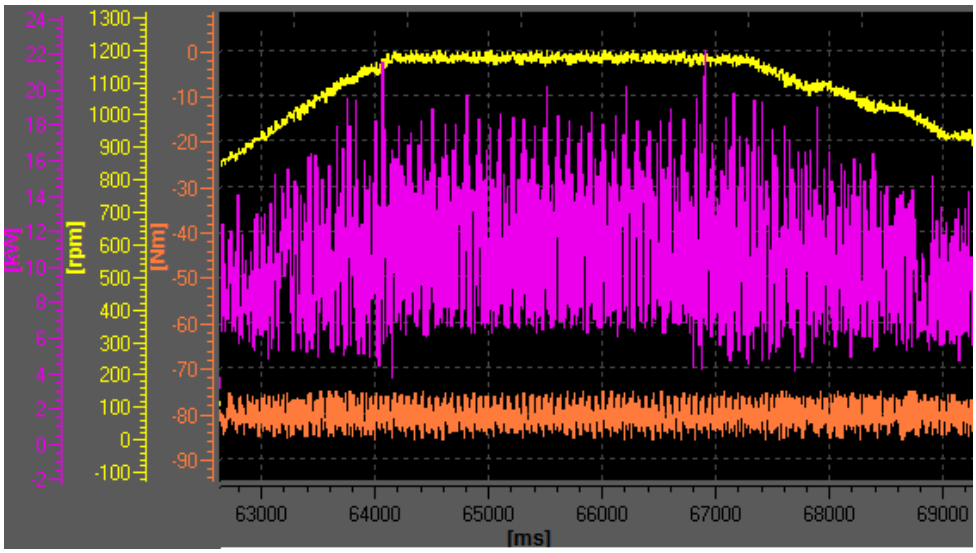

Figure 5.12: Maximum and nominal power determination test.

was unknown. Therefore, to assure that the temperature limit of the PM would be never reached, a maximum motor temperature of 80°C was set. PM with higher working temperature must be used to meet the values observed during the thermal analysis.

5.6 Efficiencies testing

To determine the practical efficiency of the MJF motor, a watt-meter was connected to each motor phase to measure voltage and current waveforms. With these measurements, the instant power can be calculated. The output mechanical power was measured in the Siemens machine side, so this value also includes the efficiency of the two transmission boxes that decrease the final efficiency value of the MJF motor.

Table 5.4 shows the MJF efficiency results. The efficiencies of the two transmission boxes are not considered on this table, as their real values are not known. In fact, looking at their mechanical tests, it is possible to see that the first has a theoretical efficiency of about 98% and the second of 96%. The repetition of this test with a proper test-bench, where the mechanical power is measured without the influence of a transmission box, is recommended to be performed in the future.

Table 5.4: MJF efficiency result test.

	Velocity[kRPM]												
Torque [Nm]	0,5	1	2	3	4	5	6	7	8	9	10	11	12
1	0,52	0,55	0,57	0,60	0,61	0,63	0,66	0,70	0,68	0,67	0,65	0,60	0,58
2	0,46	0,54	0,59	0,60	0,65	0,67	0,71	0,72	0,73	0,75	0,73	0,72	NaN
3	0,44	0,53	0,62	0,70	0,73	0,76	0,80	0,81	0,82	0,85	0,86	NaN	NaN
4	0,43	0,56	0,65	0,75	0,76	0,80	0,82	0,88	0,91	0,92	NaN	NaN	NaN
6	0,42	0,62	0,72	0,79	0,81	0,83	0,84	0,86	0,93	0,94	NaN	NaN	NaN
8	0,42	0,52	0,73	0,73	0,74	0,76	0,80	0,85	0,90	0,92	NaN	NaN	NaN
10	0,37	0,52	0,66	0,68	0,68	0,69	0,75	0,80	0,85	0,90	NaN	NaN	NaN
12	0,35	0,49	0,62	0,64	0,66	0,68	0,70	0,75	0,80	NaN	NaN	NaN	NaN
14	0,31	0,46	0,58	0,60	0,62	0,65	0,67	0,70	0,75	NaN	NaN	NaN	NaN

With all the pair of values presented in Table 5.4 and using a Matlab script, it is possible to draw the

efficiency map presented in Figure 5.13 . It can be concluded that the value of the maximum efficiency is high (around 94%), proving the characteristic of synchronous machines. The efficiency at low velocities and low torque are small due to constant losses predominance over the work done, as explained in the Chapter 3.

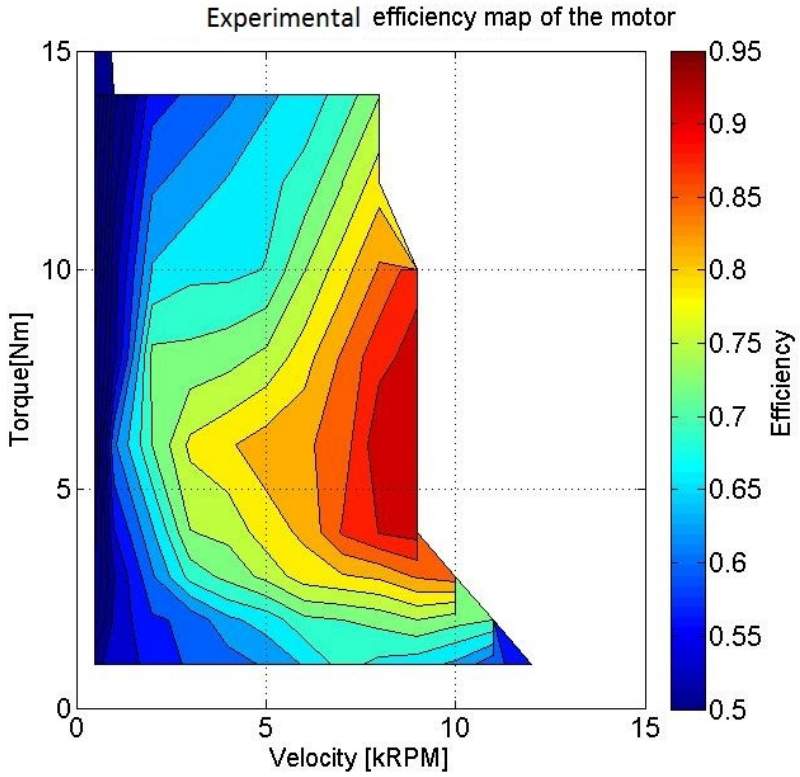

Figure 5.13: MJF efficiency map tested.

5.7 Endurance testing

A future version of the MJF prototype motor will be used on the FST 08e car and so reliability tests must be also done. The dynamic event of the competitions that test the overall reliability of the car, the endurance, consists of a 22 Km race. The average speed of the cars is about 60 Km/h and so normally it should not take longer than 25 minutes to finish the race. This test also validates the nominal power of the motor, as thermal stabilization is reached.

Two tests, 30 minutes long, were conducted in order to evaluate not only, reliability, but mainly, the temperatures of the motor with and without water refrigeration at the nominal torque and current that the car needs (6 Nm, 16 A). The initial temperatures of both tests were around 25°C and the flow rate of the cooling pump was 17 l/min. The temperature was measured in the three phase's windings, being its limit set to 80°C (instead of 180°C in the windings and 80°C in the rotor), because is no possible to measure the temperature of the motor - Figure 5.14. During the endurance simulations, the motor rotated with a torque of 6.5 Nm and a speed of 2000 RPM. These values were chosen because the power supply was limited to 3kW and because the nominal torque of the car during the endurance was the most important

parameter to test, as this variable is the one that most influences the motor temperature. The results obtained are shown Figure 5.14; in the latter, the green line (with cooling) increases initially faster than the red one (without cooling) due two factors: in the first case, the water had higher temperature at the beginning and in the second, the pump also dissipated some not negligible heat to the water.

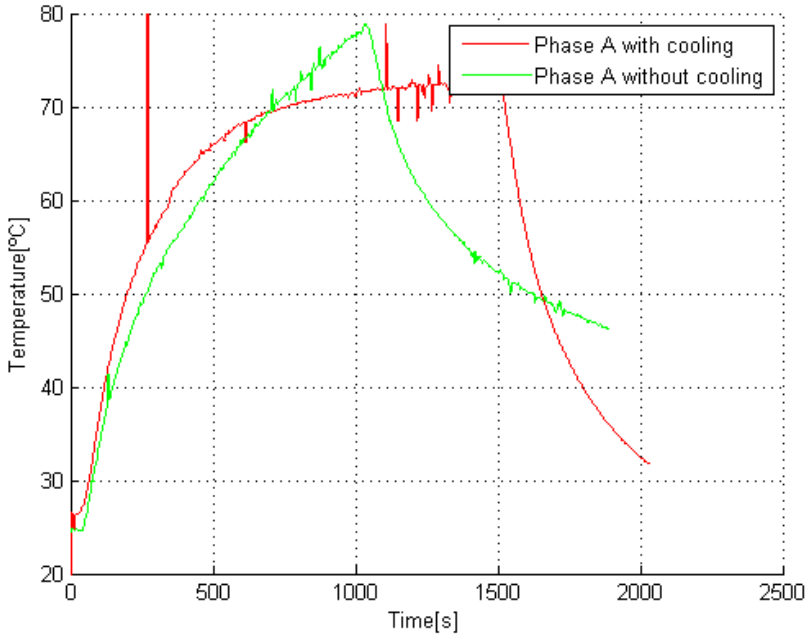

Figure 5.14: Temperatures of the MJF motor during endurance tests with and without cooling.

During these tests, the test-bench topology was inverted. The MJF motor was used as a generator connected to a three-phase resistor load of 0.3 Ω mounted in star and the Siemens generator was used as a motor with a velocity of 100 RPM.

Assuming that the iron losses at higher velocities with the same load will not increase the motor temperature higher than 80°C and that until 9000 RPM field-weakening does not occur (this assumption was verified and will be explained later in Figure 5.17), the nominal power is set to be around 5.5 kW (6 Nm at 9000 RPM). The nominal power is approximately 1 kW less than the expected. After analysing the thermal models and the prototype pieces, it was concluded the following: i) the insulation paper must be included on the FEA as it decreases considerably the heat transfer from the coils to the cooling system and, ii) thermal paste must be used between the outer stator surface and the housing, once during the repetitive assembly and disassembly of the motor the gap between them increased.

To conclude, the utilization of PM with a maximum working temperature of 120°C as studied by [13] would increase the nominal power. Further studies in this field are proposed as future work.

5.7.1 Final considerations

During the tests, it was possible to measure the terminal voltages feeding the motor. As the battery is limited to 600 V_{DC} and this voltage decreases during use, it is important to analyse the motor performance over the battery voltages. Furthermore, the battery has a resistance, resulting of the internal

resistance of each cell and of the wiring's resistance.

The inverters, responsible of inverting the DC voltage of the battery to AC voltage feeding the motors, have an associated factor of modulation, m_a, that decreases with the battery voltage [45]. Considering this factor given from the manufacturer (Appendix A), it is possible to determine the AC RMS phase voltage feeding the motor (Figure 5.15).

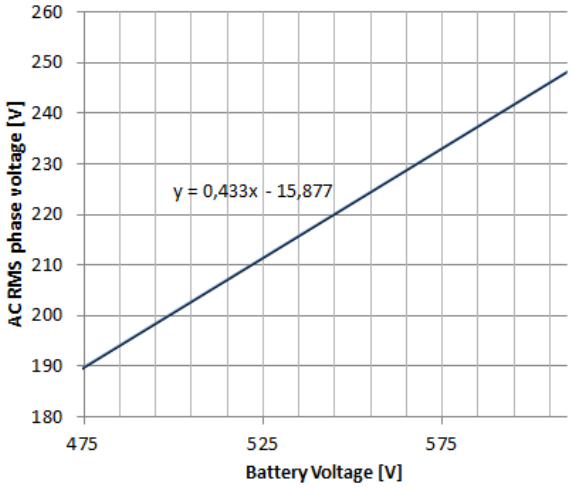

Figure 5.15: Maximum motor supplying voltage with battery voltage variation.

Not only the velocity contributes for the increase of the induced voltage, but also the voltage drop in the windings due to the current flowing through them. With low load, this is not negligible. As torque increases, the current passing through the motor also augments, increasing the induced voltage. This effect is registered in Figure 5.16, where load was incremented for the same velocity (400 RPM). Note that the torque in this figure is relative to the Siemens machine, to get MJF torque one must divide the values by the transmission ratio (1:5).

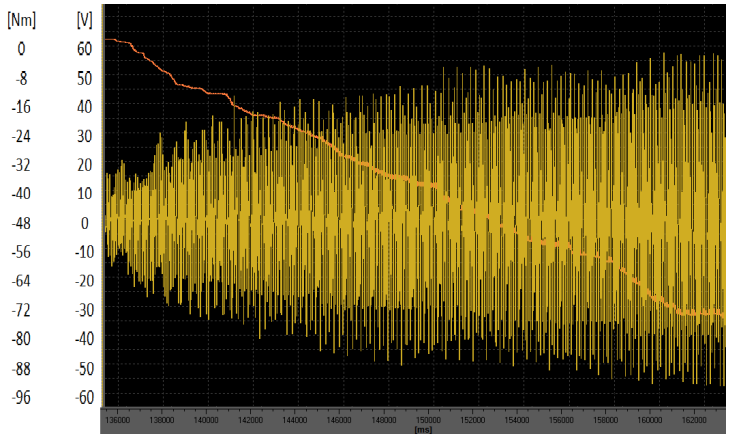

Figure 5.16: Motor terminal voltage at 400 RPM with linear increasing of load torque. (gold - terminal voltage [V], orange - torque [Nm]).

Considering the previous Figure 5.16, and summing this with the BEMF of the motor, one can conclude to see that the performance of the motor is limited by the battery voltage due to the fact that the induced voltage of the motor match the maximum output inverter voltage at 6500 RPM (instead of the

supposed base speed of 9000 RPM). From that point, torque will decrease for higher speeds due to field-weakening. Some part of the current will be responsible of reducing the rotor magnetic field instead of producing torque - field-weakening. Figure 5.17 shows the variation of the velocity and torque values of the motor with the battery voltage variation.

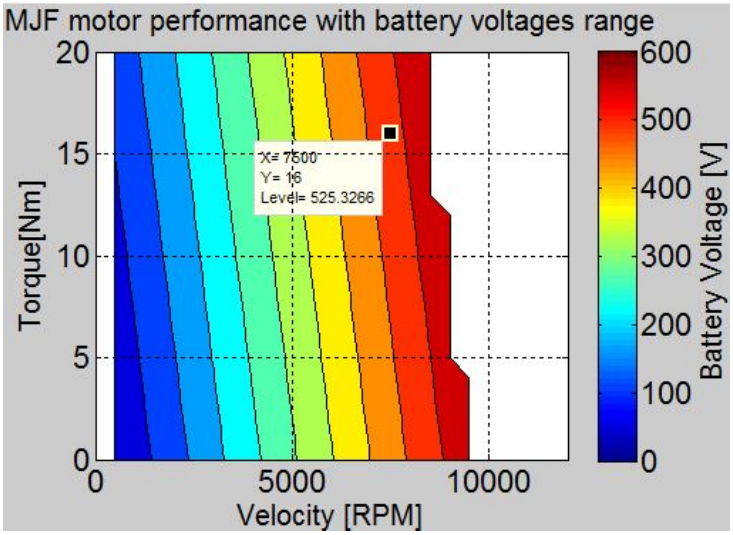

Figure 5.17: Torque and velocity of the motor over battery working voltages with 20 turn coils per slot.

According to Figure 5.17, it is possible to see that, for example, with 600V, the maximum motor velocity at 20 Nm is limited to 8 500 RPM; considering that the battery is almost at the minimum charge (475 V), this velocity is reduced to 6500 RPM. This means that it is possible to further improve the adaptation of the MJF motor to the prototype car, by changing the number of turns per coil of the windings. This is assured without compromising the torque, as the maximum value is generated with 50 A (without saturation) and the inverters are capable of feeding 100 A. By decreasing the number of turns per coil, it is possible to increase the number of conductors in parallel, reducing the phase resistance and inductance as well as the feeding voltage for a given torque and velocity. Those results showed that it is possible to increase the MJF motor velocity for the same battery voltage.

For the final solution, other unexpected events played an important role. They are briefly presented below.

The first unexpected situation occurred when a winding phase was damaged during a disassembly of the motor (Figure 5.18(b)). Three of the five conductors were broken and the insulation was lost. Due to time and financial limitations, a rewinding was not possible, so the conductors were repaired using a net of copper wire to assure the current conduction and insulation epoxy material was placed on top. Although these solutions worked well, they created a point of higher resistivity that heated more than the rest of the windings. Furthermore, an unbalanced condition was created and the motor vibrations increased. The efficiency and maximum power tests were done after this repair, which means they were influenced and limited by this issue.

From the torque-speed graph (Figure 5.19) one can see all the values measured during the different tests, and trace the equivalent graph (red). With those it is possible to draw the maximum torque-speed

(a) Rust layer. (b) Winding phase damage.

Figure 5.18: Damages that influenced the final results.

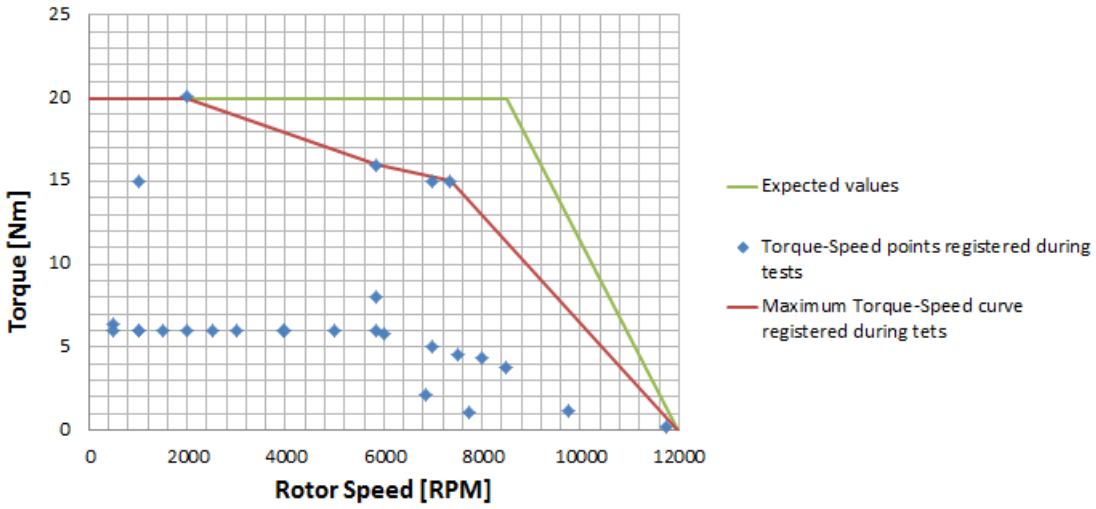

Figure 5.19: Torque-speed MJF curve of the MJF motor.

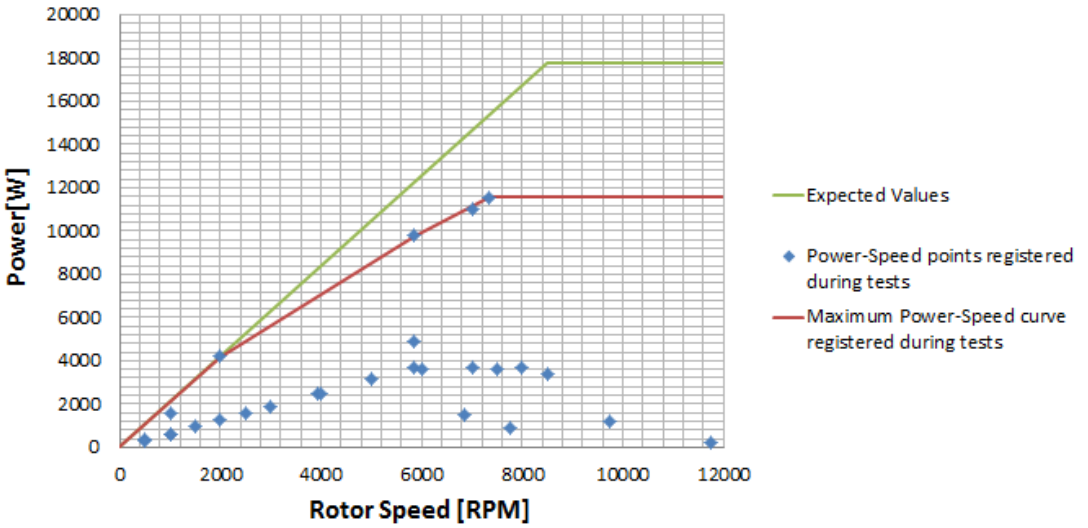

Figure 5.20: Power-speed MJF curve of the MJF motor.

real curve of the MJF motor if no test-bench limitations had occur (green graph). To trace this graph it is assumed that the maximum torque is maintained until the speed the BEMF is equivalent to the maximum voltage the inverter is capable of feeding (8500 RPM). After that point, the torque decrease linearly to zero, when the motor reach its maximum speed. Although, this was not tested, it is possible to estimate that graph, doing the two tests separately (velocity with lower torques and torque with lower velocities). All the graphs were traced considering a battery voltage of 600 V.

The same happens with the power-speed curve (Figure 5.20): the real tested power was less than the expected one because it was not possible to test all the working range points of the motor, mainly the ones having high torque at high rotor speeds (the estimated curve of the maximum power without test limitation is represented in purple and the power-speed curve for the MJF motor is represented in green). One can conclude that the motor cannot perform more than 18 kW with a feeding battery voltage of 600V. To the 20 kW, the battery should had around 620V. As it is not possible in FS, the solution passes by decreasing the number of turns per coils to 10, with no consequence to the maximum generating torque ability of the motor.

Others events, different from the one pointed out before, contributed for the final decrease of performance of the MJF motor such as:

- The second unexpected situation occurred when the motor was opened to perform a winding repair. A rust layer between the outer stator and housing, due to water infiltration during the cooling system assembly, was noticed (Figure 5.18(a)). The layer was sealed but this operation had huge implications on the maximum power test because the heat removal capability of the cooling system decreased exponentially. Therefore, a new maximum power test should be done in the future using thermal paste on the boundary, which is expected to improve the heat removal capability.
- The third unexpected situation occurred during the realization of one test due to the conjunction of a human error with a fault on the application of the security software for the inverter limit. The velocity of the motor went far above the limit imposed for the maximum value. This uncontrolled high acceleration created an instant peak and induced a voltage of the MJF motor in the inverter higher than the defined inverter limit value. The IGBTs did not handle the voltages and were destroyed. A new inverter needed to be used but the consequences on the MJF motor were not assessed as it continued to work normally.

In Figure 5.21 a comparison between theoretical and experimental results is performed, considering no limitations of the test-bench had occurred. A decrease of the maximum torque (from 20.5 to 20 Nm) and of the base speed (from 9 500 RPM to 8 500 RPM) was observed. The first one is due to the expected manufacturing influence on the motor, and the second occur because the induced voltage at the terminals at 20 Nm and 8 500 RPM was higher than the calculated. As a consequence, the peak power decreased from 20.5 kW to 18 kW.

Nevertheless, and with some minor modifications, the work carried out showed the possibility of design and manufacture a competitive tailored motor. With this, it is possible to design a geometry

adaptable to a racing environment instead of adapting a commercial solution which is more expensive and has more standards, some of them not important for the desire application.

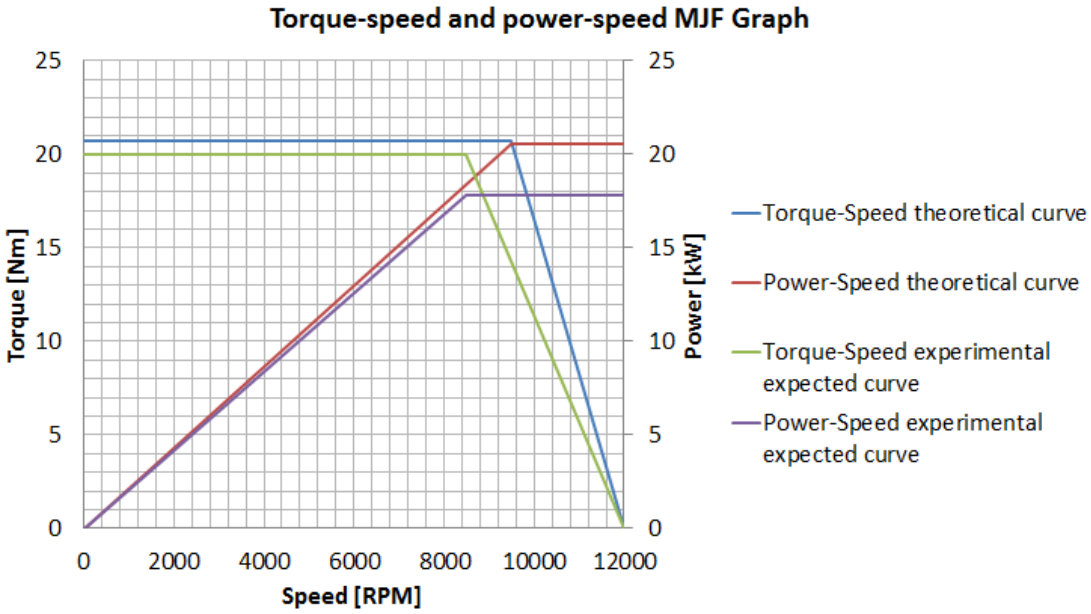

Figure 5.21: MJF theoretical and experimental results.

The MJF motor specifications and overall time-sheet is show n in Appendix F.

Chapter 6

Conclusions and future work

The main objective of this thesis was to design, manufacture and test an electric motor prototype for the FST 08e car, the future race-car (2018) of the team of FST Lisboa of the University of Lisbon. This objective required to cover knowledge of mechanical and electronic engineering. The mix of these two areas was performed with the aim of manufacturing a prototype of a tailored electric motor. Subsequently performance tests were performed to validate the machine characteristics.

The work carried out within this thesis was based in the following tasks:

1. To review the main literature on the use of PMSM in electric racing cars;
2. To study different magnetic circuit geometries of electric machines that meets the given performance specifications: maximum power of 20 KW, maximum torque of 20Nm, maximum weight of 5 kg and a maximum velocity of 12 000 RPM.
3. To optimize the magnetic circuit of the PMSM using an Evolutionary algorithm coupled to a FEA software; the objective functions of the two different algorithms used are associated to the electromagnetic torque, balanced stator windings layout and minimization of the magnetomotive force harmonics in the air-gap; defined constraints were the volume, power losses and weight of the motor;
4. To build a prototype, assembling the motor;
5. To perform an extensive set of experimental tests to obtain the motor electromechanical characteristics; in order to conduct the velocity, torque, power, efficiency and endurance tests, a test-bench was built.

The thesis presents a detailed description of all the design and manufacturing process of the motor as well as of the overall testing carried out to assess its behavior and performance. The tests results obtained are listed below:

- Coil turns, performed in order to determine the excitation voltage created by different coil distributions and the thermal behavior of the system; the tests showed that the chosen configuration with 20 turns per coil met the induced voltage requisites as it induced 220V at 9000 RPM;
- Maximum velocity, the maximum velocity reached on the tests was 11750 RPM (somehow limited

by the test-bench) – showing that the MJF motor is capable of doing the maximum velocity set in this thesis goals;
- Maximum torque, the maximum torque value of the MJF motor is around 20 Nm, laying in the defined goals;
- Maximum Power, the maximum mechanical power, tested to validate the thermal analysis of the motor, was set to 10kW; no higher values were tested as the risks of performing them on the self-developed test-bench were high;
- Efficiency, it was concluded that the value of the maximum efficiency is high, proving the characteristic of synchronous machines;
- Endurance simulation, two tests, 30 minutes long, were conducted in order to evaluate not only, reliability, but mainly, the temperatures of the motor with and without water refrigeration at the nominal torque and current that the car needs.

In what concerns the future work related with the MJF electric motor improvement it is proposed to undertake the following analyses:

- To model the car performance with HiperCo as core material;
- To build a new test-bench to fully test the performance of the motor;
- To isolate the windings with thinner paper or other material favoring the heat exchanges between the windings and the cooling system;
- To increase the working temperature of the motor without decreasing its performance by analysing the influence of the temperature in the winding insulating life-span and by using PM with higher Curie Temperature making possible to increase the peak and continuous torque and power of the motor without changing the geometry;
- To further improve the mechanical/structural analysis of the motor, as for example, to study the motor attachment to the car and to analyse the frequency resonances and its influence in the upright of the car;
- To analyse the demagnetization of the magnets;
- To include torque ripple minimization as another objective in the optimization script;
- To analyse the influence of non-ideal currents with harmonic content being supply to the motor;
- To test the prototype with fewer turns per coil winding;
- To analyse the integration of state of art cooling methods such as coolant through shaft or oil spray.

As a final conclusion, the work carried out resulted in the manufacturing of the MJF electric motor prototype which will serve as testing and validation model for the future and improved versions to integrate the powertrain of the FST 08e car. The electric motor prototype developed proved, according to the tests carried out, to comply with the defined requirements defined by the FST Lisboa team.

Bibliography

[1] IMechE, “About Formula Student,” accessed on 23.02.2017. [Online]. Available: https://www.imeche.org/events/formula-student/about-formula-student

[2] C. Smith, *Tune to Win - The art and science of race car development and tuning*. AERO Publishers, 1978.

[3] J. Antunes, “Torque Vectoring for a Formula Student Prototype,” Master’s thesis, Instituto Superior Técnico, 2017.

[4] W. Tong, *Mechanical Design of Electric Motors*. CRC Press, 2014.

[5] G. A. Mccoy, T. Litman, and J. G. Douglass, *Energy-Efficient Electric Motor Selection Handbook*. Washington: Washington State Energy Office Olympia, 1993, vol. 5, no. energia.

[6] A. Dente, “Máquina Síncrona,” Tech. Rep., 2007.

[7] M. Doppelbauer and P. Winzer, “Shut Up About the Batteries: The Key to a Better Electric Car Is a Lighter Motor,” 2017, acessed on 2017.08.28. [Online]. Available: https://spectrum.ieee.org/transportation/advanced-cars/shut-up-about-the-batteries-the-key-to-a-better-electric-car-is-a-lighter-motor

[8] A. Fitzgerald, C. Kingsley, and S. Umans, *Electric machinery*. McGraw-Hill, 2003, vol. 319, no. 4.

[9] Wiiwand, “Adjustable-speed drive,” accessed on 25.09.2017. [Online]. Available: http://www.wikiwand.com/en/Adjustable-speed{_}drive

[10] D. C. Hanselman, *Brushless permanent magnet motor design*. Magna Physics Publishig, 2006.

[11] “IPM and SPM machines,” accessed on 13-06-2016. [Online]. Available: https://ei.uni-paderborn.de/en/lea/research/forschungsprojekte/electrical-drives-and-mechatronic-systems/control-of-permanent-magnet-synchronous-motors-for-automotive-applications/

[12] B. Ricardo da Fonseca Marques, “Virtual Prototyping of a Brushless Permanent Magnet AC Motor - Electromagnetic and Thermal Design using CAD Software,” Master’s thesis, Instituto Superior Tecnico, 2012.

[13] P. M. d. A. Fontes, “Refrigeração do propulsor elétrico de um veículo Formula Student,” Master’s thesis, Universidade de Lisboa, 2016.

[14] J. Cardoso, “Análise de soluções para geradores eléctricos integrados em turbinas de aeronaves,” Master’s thesis, Instituto Superior Técnico, 2013.

[15] A. Goldman, *Handbook of Modern Ferromagnetic Materials*. Springer, 1999.

[16] P. Kueser and J. Toth, “Development and evaluation of magnetic and electrical materials capable of operating in the 800º to 1600º F temperature range,” NASA, Tech. Rep., 1973.

[17] “Performance Improvement Using Cobalt Iron Alloy Magnetic Core,” accessed on 19.10.2015. [Online]. Available: http://shodhganga.inflibnet.ac.in/bitstream/10603/16150/12/12_chapter%207.pdf

[18] B. Slusarek and K. Zakrzewski, “Magnetic properties of permanent magnets for magnetic sensors working in wide range of temperature,” *PRZEGLĄD ELEKTROTECHNICZNY (Electrical Review)*, no. 7, pp. 123–126, 2012.

[19] J. Gieras, *Permanent Magnet Motor Technology - Design and applications*. CRC Press, 2010.

[20] S. Magnetics, “The Difference between Maximum Working Temperature and the Curie Temperature,” accessed on 29-10-2015. [Online]. Available: http://www.magnet-sdm.com/2017/01/05/difference-maximum-working-temperature-curie-temperature/

[21] A. S. Metals, “Aerospace Specification Metals,” accessed on 8.11.2015. [Online]. Available: http://asm.matweb.com/search/specificmaterial

[22] J. Olivares-Galvan, F. de Leon, P. Georgilakis, and R. Escarela-Perez, “Selection of copper against aluminium windings for distribution transformers,” *IET Electric Power Applications*, vol. 4, no. 6, p. 474, 2009.

[23] K. Agrawal, “Winding insulation and its maintenance,” in *Industrial Power Engineering Handbook*, 2001, pp. 219–229.

[24] W. Shi, J. Liu, and C. Li, “Effect of cutting techniques on the structure and magnetic properties of a high-grade non-oriented electrical steel,” *Journal of Wuhan University of Technology-Mater. Sci. Ed.*, vol. 29, no. 6, pp. 1246–1251, 2014.

[25] A. Belhadj, P. Baudouin, F. Breaban, and A. Deffontaine, “Effect of laser cutting on microstructure and on magnetic properties of grain non-oriented electrical steels,” vol. 256, pp. 20–31, 2003.

[26] A. Schoppa, H. Louis, F. Pude, and C. Von Rad, “Influence of abrasive waterjet cutting on the magnetic properties of non-oriented electrical steels,” *Journal of Magnetism and Magnetic Materials*, vol. 254-255, pp. 370–372, 2003.

[27] A. Ahmed, “Maximum Torque Per Ampere (MTPA) Control for Permanent Magnet Synchronous Machine Drive System,” Master’s thesis, 2013.

[28] J. N.P.Quang, *Vector Control of Three-Phase AC Machines*. Springer.

[29] D. Delgado, “Automated AC winding design,” Master’s thesis, University of Manchester, 2009.

[30] Emetor, “Electric motor winding calculator,” 2011, accessed on 20.01.2017. [Online]. Available: https://www.emetor.com/edit/windings/

[31] D. Oliveira, “Electromagnetic Design of a PM Synchronous Generator for a 20 kW Ultra-low Head Hydro Turbine,” Master’s thesis, Instituto Superior Técnico, 2015.

[32] Comsol, *Introduction to LiveLink for MATLAB*. Comsol, 2012.

[33] COMSOL, *COMSOL Java API Reference Guide*. COMSOL, 2012.

[34] C. Power, “Cogent Power NO20 Datasheet,” accessed on 27.10.2015. [Online]. Available: https://cogent-power.com/cms-data/downloads/Hi-Lite{_}NO20.pdf

[35] COMSOL, *AC/DC Module User’s Guide*. COMSOL, 2017.

[36] E. Barkanov, “Introduction to the Finite Element Method,” Master’s thesis, Institute of Materials and Structures Faculty of Civil Engineering Riga Technical University, 2001.

[37] Comsol, “COMSOL Multiphysics 4.4 Reference Manual,” p. 1270, 2013.

[38] N. Sadowski, Y. Lefevre, M. Lajoie-Mazenc, and J. Cros, “Finite element torque calculation in electrical machines while considering the movement,” *IEEE Transactions on Magnetics*, vol. 28, no. 2, pp. 1410–1413, 1992.

[39] D. Gerling, “Comparison of Different FE Calculation Methods for the Electromagnetic Torque of PM Machines,” *NAFEMS Seminar: Numerical Simulation of Electromechanical Systems*, pp. 1–8, 2005.

[40] A. Santos, “Dynamic analysis and design of impact attenuator structures for a Formula Student prototype,” Master’s thesis, Instituto Superior Técnico.

[41] J. K. N. R. G. Budynas, *Shigley’s Mechanical Engineering Design, Ninth Edition*. New York: McGraw-Hill, 2011.

[42] L. Pinto, “Integrated Electrical Generators in Aircraft Turbines Thermal analysis of a front-low rotation 90 kVA PM synchronous auxiliary generator,” Master’s thesis, Instituto Superior Técnico, 2015.

[43] A. Krings and J. Soulard, “Overview and Comparison of Iron Loss Models for Electrical Machines,” *Journal of Electrical Engineering*, vol. 10, pp. 162–169, 2010.

[44] L. and Bauer, “Speed and position sensor MiniCoder GEL 2444,” Tech. Rep.

[45] E. H. E. Aboadla, S. Khan, M. H. Habaebi, T. Gunawan, B. A. Hamidah, and M. B. Yaacob, “Effect of modulation index of pulse width modulation inverter on Total Harmonic Distortion for Sinusoidal,” *2016 International Conference on Intelligent Systems Engineering, ICISE 2016*, no. 1, pp. 192–196, 2016.

[46] Supermagnete, “NdFeB tecnical information,” accessed on 03.11.2015. [Online]. Available: https://www.supermagnete.de/eng/data{_}sheet{_}Q-40-15-05-N.pdf

[47] Vacuumschmelze, “Hiperco Datasheet,” accessed on 20.10.2016. [Online]. Available: http://www.vacuumschmelze.com/fileadmin/Medienbiliothek{_}2010/Downloads/HT/VACODUR{_}49{_}.pdf

[48] SKF, “SKF Bearing technical information,” accessed on 10.01.2016. [Online]. Available: http://www.skf.com/ph/products/bearings-units-housings/ball-bearings/deep-groove-ball-bearings/deep-groove-ball-bearings/index.html?designation=6201-2RSL

Appendix A

Inverters and AMK motor Specifications

DC link voltage 510 ... 720 V DC		**Single Motor Module in booksize format**				
• Internal air cooling	6SL3120-	1TE24-5AA3	1TE26-0AA3	1TE28-5AA3	1TE31-3AA3	1TE32-0AA4
• External air cooling	6SL3121-	1TE24-5AA3	1TE26-0AA3	1TE28-5AA3	1TE31-3AA3	1TE32-0AA4
• Cold plate cooling	6SL3126-	1TE24-5AA3	1TE26-0AA3	1TE28-5AA3	1TE31-3AA3	1TE32-0AA4
• Liquid cooling	6SL3125-	–	–	–	–	1TE32-0AA4
Output current						
• Rated current I_{rated}	A	45	60	85	132 (105 [6])	200 (140 [6])
• Base-load current I_H	A	38	52	68	105 (84)	141 (99)
• For S6 duty (40 %) I_{S6}	A	60	80	110	150 (120)	230 (161)
• I_{max}	A	85	113	141	210	282
Rated pulse frequency	kHz	4	4	4	4	4
Type rating [1]						
• Based on I_n	kW (HP)	24 (30)	32 (40)	46 (60)	71 (100)	107 (150)
• Based on I_H	kW (HP)	21 (25)	28 (40)	37 (50)	57 (75)	76 (100)
DC link current I_d [2]	A	54	72	102	158	200
Current carrying capacity						
• DC link busbars	A	200	200	200	200	200
• 24 V DC busbars [3]	A	20	20	20	20	20
DC link capacitance	µF	1175	1410	1880	2820	3995
Current requirement At 24 V DC, max.	A	1.2	1.2	1.5	1.5	1.5
Internal/external air cooling						
• Power loss [4]						
- With internal air cooling in control cabinet	kW	0.46	0.62	0.79	1.29	2.09
- With ext. air cooling, int./ext.	kW	0.14/0.32	0.16/0.46	0.2/0.59	0.29/1.0	0.47/1.62
• Cooling air requirement	m^3/s (ft^3/s)	0.031 (1.1)	0.031 (1.1)	0.044 (1.6)	0.144 (5.1)	0.144 (5.1)
• Sound pressure level L_{pA} (1 m)	dB	< 65	< 65	< 60	< 73	< 73
Cold plate cooling						
• Power loss, int./ext. [4]	kW	0.11/0.34	0.13/0.48	0.15/0.62	0.24/1.05	0.39/1.7
• Thermal resistance R_{th}	K/W	0.055	0.055	0.05	0.028	0.028
Motor connection U2, V2, W2		M6 screw studs (X1)	M6 screw studs (X1)	M8 screw studs (X1)	M8 screw studs (X1)	M8 screw studs (X1)
• Conductor cross-section, max.	mm^2	2.5 ... 50	2.5 ... 50	2.5 ... 95, 2 × 35	2.5 ... 120, 2 × 50	2.5 ... 120, 2 × 50
Shield connection		See Accessories	See Accessories	See Accessories	See Accessories	See Accessories
PE connection		M6 screw	M6 screw	M6 screw	M8 screw	M8 screw
Motor brake connection		Plug-in connector (X11), 24 V DC, 2 A	Plug-in connector (X11), 24 V DC, 2 A	Plug-in connector (X11), 24 V DC, 2 A	Plug-in connector (X11), 24 V DC, 2 A	Plug-in connector (X11), 24 V DC, 2 A
Motor cable length, max.						
• Shielded/unshielded	m (ft)	100/150 (328/492)	100/150 (328/492)	100/150 (328/492)	100/150 (328/492)	100/150 (328/492)
Degree of protection		IP20	IP20	IP20	IP20	IP20
Dimensions						
• Width	mm (in)	150 (5.91)	150 (5.91)	200 (7.87)	300 (11.81)	300 (11.81)
• Height	mm (in)	380 (14.96)	380 (14.96)	380 (14.96)	380 (14.96)	380 (14.96)
- With fan [5]		–	–	–	629 (24.76)	629 (24.76)
• Depth						
- With internal air cooling	mm (in)	270 (10.63)	270 (10.63)	270 (10.63)	270 (10.63)	270 (10.63)
- With external air cooling, on/behind mounting surface	mm (in)	226/71 (8.90/2.80)	226/71 (8.90/2.80)	226/92 (8.90/3.62)	226/82 (8.90/3.23)	226/82 (8.90/3.23)
- With cold plate cooling	mm (in)	226 (8.90)	226 (8.90)	226 (8.90)	226 (8.90)	226 (8.90)
Weight, approx.						
• With internal air cooling	kg (lb)	9 (19.8)	9 (19.8)	15 (33.1)	21 (46.3)	21 (46.3)
• With external air cooling	kg (lb)	13.2 (29.1)	13.4 (29.5)	17.2 (37.9)	27.2 (60.0)	30 (66.2)
• With cold plate cooling	kg (lb)	9.1 (20.1)	9.1 (20.1)	12.5 (27.6)	18 (39.7)	18 (39.7)

Figure A.1: Siemens Inverter Specifications

	Terminal / strand	KW26-S5-FSE-4Q (data per inverter)
Rated input voltage HV+, HV- power supply	HV+, HV-	540 VDC
Input voltage range		250 VDC - 720 VDC
Input current **Power supply for HV = 540 VDC**		48 A
Intermediate circuit capacity		75 µF
Supply voltage **for logic supply LV**	X08 (X09)	24 VDC ±15%, The 0 V potential must be connected to the vehicle ground (vehicle chassis).
Input current **for logic supply LV**		≤ 500 mA
Capacity at input of internal switched-mode power supply		1,500 µF
Efficiency		Approx. 98%
Ground		Vehicle ground (vehicle chassis) or ground strap Switching GND for logic voltage is internally connected to the frame of the inverter
Control method **Switching frequency**		PWM 8 kHz
Output frequency	U, V, W	0 - 599 Hz
Output voltage (HV = 540 VDC)		350 VAC (sinusoidal output current)
Output voltage range (HV = 250 - 720 VDC)		160 - 490 VAC
Rated output power		26 KVA
Rated output current I_N		43 A
Peak output current I_{max}		105 A
Max. duration of peak output current I_{max}		
Output frequency f_{OUT}> 1 Hz		10 s
Output frequency f_{OUT}≤ 1 Hz		1 s
Temperature sensor evaluation	X12	KTY e.g., KTY84-130
Protective / monitoring function	Short-circuit / ground fault, intermediate circuit overvoltage, excess temperature at motor / heat sink, current overload as per I^2t	
Cooling	Liquid cooling	
Flow rate	1.5 bar / 10 l/min	
Max. cold plate and ambient temperature	40 °C	
Protection class	IP00	

Figure A.2: AMK Inverter Specifications

Motor-Datenblatt *motor data sheet*

AMK

Bezeichnung/name	**DD5-14-10-POW** - 18600-B5	Formula Student	Datum/date: 20.04.2015
Teile-Nr:/part number	**A2370DD**		Zeichn.-Nr:/drawing no.:12703-01260

Motorbeschreibung *motor description:*

Motorprinzip/motor principle:	synchron
Kühlart/cooling type:	Flüssigkeit
Bauform/mounting type:	IMB5
Schutzart/degree of protection:	IP 65
Isolierklasse/insulation class:	F

Leistungsdaten *performance data:*

Betriebsart/duty type:	S1 dT=80K
Dauerstillstandsmoment/continuous Stall Torque "Mo":	13,8 Nm
Maximales Moment/maximum torque "Mmax":	21 Nm
Bemessungsmoment/rated torque "Mn" (ID32771):	9,8 Nm
Bemessungsleistung/rated power "Pn":	12,3 kW
Bemessungsdrehzahl/rated speed "Nn" (ID32772):	12000 rpm
Theo. Leerlaufdrehzahl/theor. no-load-speed "No":	18617 rpm

Motorkennlinien *performance - characteristics:*

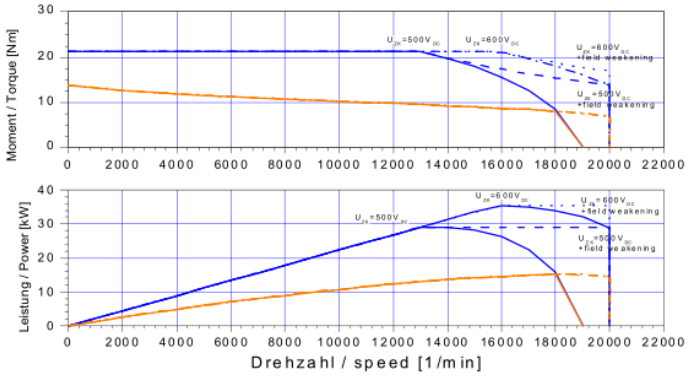

Kennlinie kann die maximal zulässige Drehzahl übersteigen! / Characteristic may exceed mechanical speed limit of motor

Elektrische Daten *electrical data:*

Nennspannung/rated voltage "Un" (ID32768):	350 V
Nennstrom/rated current "In" (ID111):	41 Arms
Dauerstillstandsstrom/cont. stall current " Io" (ID34096):	53,1 Arms
Maximalstrom/maximum current "Imax" (ID109):	100 Arms
Maximale Dauer für/duration for "Imax" (ID34168):	1,24 s
Drehmomentkonstante/torque constant " kt":	0,26 Nm/Arms
Spannungskonstante/voltage constant "ke" (ID 34234):	18,8 V/kU/min
Schaltung/connection type:	D
Polzahl/number of poles "2p" (ID32775):	10 Pole
Klemmenwiderstand/terminal resistance "Rtt" (ID34164):	0,13 Ohm
Klemmeninduktivität/terminal inductance "Ltt" (ID34167):	0,3 mH
Querachseninduktivität/quadrature axis inductance "Lq" (ID34046)	0,54 mH
Hauptachseninduktivität/direct axis inductance "Ld" (ID34045):	0,44 mH
Magn.-Strom/magn. current "Im" (ID32769):	70 Arms
Magn.-Strom/magn. current "Im1" (ID32770):	3,5 Arms
Rotorzeitkonstante/rotor time constant "Tr" (ID32774):	0,01 s

Reglereinstellungen *controller settings:*

Stromregler ***current controller:***

Verstärkung q-Achse/gain q-axis "Kpq" (ID34151):	1,62 V/A
Verstärkung d-Achse/gain d-axis "Kpd" (ID34152):	1,72 V/A
Nachstellzeitkonstante/time constant "Tnq" (ID34050):	1,2 ms
Nachstellzeitkonstante/time constant "Tnd" (ID34052):	1,2 ms
Adaption Verstärkung/adaption gain "Kpq2" (ID 34179)	20 %
Adaption Nachstellzeit/adaption time constant "Tnq2" (ID 34180)	400 %
Untere Anpaßschwelle/lower adaption limit "Iua" (ID34177):	32 %
Obere Anpaßschwelle/upper adaption limit "Ioa" (ID34178):	78 %

Drehzahlregler ***speed controller (default for plain motor):***

Verstärkung/gain "Kp_n" (ID100):	40
Nachstellzeitkonstante/time constant "Tn_n" (ID101):	10 ms

Spannungsregler ***voltage controller:***

Spannungsregler/voltage controller "Kp" (ID34148):	0,08 A/V
Spannungsregler/voltage controller "Tn" (ID34149):	6 ms
Spannungsüberhöhung "dU" (ID34235):	116 %
Systemwiderstand "Rs" (ID34233):	0 Ohm

Appendix B

MJF materials and components technical information

B.1 Magnets technical information

Article ID	Q-40-15-05-N
Material	NdFeB
Shape	Block
Size	40 x 15 x 5 mm
Side 1	40 mm
Side 2	15 mm
Side 3	5 mm
Pole faces	40 x 15 mm
Tolerance	+/- 0,1 mm
Direction of magnetisation	Axis 5 mm
Coating	Nickel-plated (Ni-Cu-Ni)
Manufacturing method	sintered
Magnetisation	N40
strength	approx. 8 kg (approx. 78,5 N)
Max. working temperature	80°C (possibly lower) *
Weight	22,8000 g
Curie temperature	310 °C
Residual magnetism Br	12600-12900 G, 1.26-1.29 T
Coercive field strength bHc	10.5-12.0 kOe, 860-955 kA/m
Coercive field strength iHc	≥12 kOe, ≥955 kA/m
Energy product (BxH)max	38-40 MGOe, 303-318 kJ/m^3

Figure B.1: NdFeB technical information [46].

B.2 Magnetic Core technical information

Main properties

Very high saturation induction up to 2.35 T
Adjustable yield strength up to 390 MPa

Applications

High performance motors with maximum power density and low losses

Magnetic properties (typical values)

Coercivity	H_c	50 A/m (optimum magnetic properties) 110 A/m (optimum mechanical properties)
Saturation polarisation	J_s	2.30 T
Maximum permeability	μ_{max}	7,000 (optimum magnetic properties) 15,000 (optimum mechanical properties)
Curie temperature	T_C	950 °C

Static virgin curve (typical values)

Magnetic field strength	H	(kA/m)	0.3	0.8	1.6	4.0	8.0	16
Induction @ $R_{p0.2}$ = 210 MPa	B	(T)	1.90	2.10	2.20	2.26	2.28	2.30
Induction @ $R_{p0.2}$ = 390 MPa	B	(T)	1.80	2.05	2.15	2.25	2.27	2.30

Iron losses for strip thickness 0.35mm (typical values)

Induction	B	(T)	1.5	1.5	2.0	2.0
Frequency	f	(Hz)	50	400	50	400
Loss @ $R_{p0.2}$ = 210 MPa	p_{Fe}	(W/kg)	1.6	31	2.5	60
Loss @ $R_{p0.2}$ = 390 MPa	p_{Fe}	(W/kg)	2.9	43	5.0	78

Physical properties (typical values)

Density	ρ	8.12 g/cm³
Specific electrical resistivity	ρ_{el}	0.4 µΩm
Thermal expansion coefficient	α	9.15 · 10^{-6} 1/K (20...200 °C)

Mechanical properties (typical values)

		optimum magnetic properties	optimum mechanical properties
Tensile strength	R_m	400 MPa	720 MPa
Yield strength	$R_{p0.2}$	210 MPa	390 MPa
Young's Modulus	E	200 GPa	250 GPa
Hardness	HV 10	185	220

Figure B.2: Hiperco technical information [47].

J_{peak} T	at 50 Hz W/kg	at 400 Hz W/kg	at 2500 Hz W/kg
0.1	0.02	0.17	2.79
0.2	0.07	0.72	10.6
0.3	0.14	1.49	24.4
0.4	0.23	2.50	40.4
0.5	0.32	3.80	58.4
0.6	0.42	5.17	78.4
0.7	0.54	6.70	103
0.8	0.66	8.36	133
0.9	0.80	10.3	166
1.0	0.95	12.3	200
1.1	1.14	14.8	248
1.2	1.36	17.9	
1.3	1.65	21.4	
1.4	2.00	25.3	
1.5	2.40	29.7	
1.6	2.75		
1.7	3.06		
1.8	3.32		

Figure B.3: NO20 technical information [34]

	GUARANTEED VALUES	TYPICAL VALUES
Loss at 1.0 T and 50 Hz, W/kg	-	0.95
Loss at 1.0 T and 400 Hz, W/kg	15.0	12.3
Loss at 1.0 T and 2500 Hz, W/kg	215	200
Nominal thickness, mm		0.20
Resistivity, μΩcm		52
Density, g/cm³		7.65
Yield strength, N/mm²		370
Tensile strength, N/mm²		450

Figure B.4: NO20 technical information [34]

B.3 Bearings Datasheet

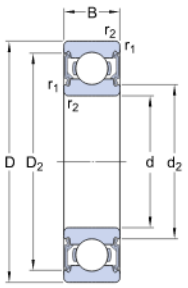

d		12	mm
D		32	mm
B		10	mm
d_2	≈	16.2	mm
D_2	≈	27.34	mm
$r_{1,2}$	min.	0.6	mm

Calculation data

Basic dynamic load rating	C	7.28	kN
Basic static load rating	C_0	3.1	kN
Fatigue load limit	P_u	0.132	kN
Reference speed		50000	r/min
Limiting speed		26000	r/min
Calculation factor	k_r	0.025	
Calculation factor	f_0	12	

Mass

Mass bearing		0.037	kg

Figure B.5: SKF 6201 - 2RSL technical information [48].

B.4 Encoder technical information

Electrical Data	
Output level	1 V_{SS} (difference signal)
Output signal	two 90° phase-shifted sinusoidal signals and their inverse signals, short-circuit proof; optionally with reference pulse
Output frequency	0 to 200 kHz (1)
Offset (static)	± 20 mV
Amplitude tolerance	-20% to +10%
Amplitude ratio U_{TR1} /U_{TR2}	0.9 to 1.1
Supply voltage U_S	5 V DC ± 5%
Power consumption without load	≤ 0.3 W
Mechanical Data	
Module of the target wheel	0.3 / 0.5
Admissible air gap	0.15 mm ± 0.02 mm with module 0.3 0.2 mm ± 0.03 mm with module 0.5
Width of the target wheel	min. 4.0 mm
Material of the target wheel	Ferromagnetic steel
Max. admissible cable length	100 m (observe the voltage drop on the power line)
Working temperature	-30 °C to +85 °C
Operating and storage temperature	-40 °C to +120 °C
Protection class	IP 68
Electromagnetic compatibility	EN 61000–6–1 to 4 (2)
Insulation stability	500 V, according to EN 60439–1
Vibration resistance	200 m/s², according to DIN EN 60068–2–6
Shock resistance	2000 m/s², according to DIN EN 600068–2–27
Weight	30 g
Housing	Polyphenylensulfid (PPS), fibre reinforced
Connection • Core x cross section • Outer diameter (O.D.) • Min. bending radius	Separate screen connection line for near-sensor earthing(3) 9 x 0.15 mm² $5_{-0.3}$ mm 25 mm

Figure B.6: Encoder technical information [44].

B.5 MJF theoretical efficiency

Table B.1: Theoretical efficiencies using NO20 core material

	Torque[Nm]										
Speed [kRPM]	0,5	1	2	3	4	5	6	8	10	15	20
0,4	0,79	0,76	0,79	0,73	0,68	0,64	0,60	0,53	0,47	0,38	0,31
0,5	0,80	0,78	0,81	0,77	0,72	0,68	0,65	0,58	0,53	0,43	0,36
0,75	0,80	0,82	0,85	0,82	0,79	0,76	0,73	0,67	0,62	0,53	0,46
1	0,80	0,83	0,87	0,85	0,83	0,80	0,78	0,73	0,69	0,60	0,53
1,245	0,80	0,84	0,89	0,87	0,85	0,83	0,81	0,77	0,73	0,65	0,58
1,5	0,80	0,85	0,89	0,89	0,87	0,85	0,84	0,80	0,77	0,69	0,63
2	0,79	0,86	0,90	0,90	0,89	0,88	0,87	0,84	0,81	0,75	0,69
2,52	0,79	0,86	0,91	0,91	0,91	0,90	0,89	0,86	0,84	0,79	0,74
3	0,78	0,86	0,91	0,92	0,92	0,91	0,90	0,88	0,86	0,81	0,77
4	0,77	0,86	0,91	0,92	0,93	0,92	0,92	0,90	0,89	0,85	0,81
5	0,76	0,85	0,91	0,93	0,93	0,93	0,93	0,92	0,91	0,87	0,84
6	0,75	0,85	0,91	0,93	0,93	0,94	0,93	0,93	0,92	0,89	0,87
7	0,74	0,85	0,91	0,93	0,94	0,94	0,94	0,93	0,93	0,90	0,88
8	0,74	0,84	0,91	0,93	0,94	0,94	0,94	0,94	0,93	0,91	0,89
9	0,73	0,84	0,91	0,93	0,94	0,94	0,94	0,94	0,94	0,92	0,90
10	0,72	0,83	0,90	0,93	0,94	0,94	0,94	0,94	0,94	0,93	0,91
11	0,71	0,83	0,90	0,93	0,94	0,94	0,95	0,95	0,94	0,93	0,92
12	0,71	0,82	0,90	0,93	0,94	0,94	0,95	0,95	0,95	0,94	0,92

B.6 MJF theoretical losses

Table B.2: MJF total theoretical losses using NO20 core material

	Torque[Nm]										
Speed [kRPM]	0,5	1	2	3	4	5	6	8	10	15	20
0,4	4,3	5,4	13,5	22,8	46,0	78,4	120,0	171,0	300,6	467,2	1046,0
0,5	5,5	6,6	14,7	24,0	47,1	79,5	121,2	172,1	301,8	468,4	1047,1
0,75	8,5	9,7	17,8	27,0	50,2	82,6	124,3	175,2	304,8	471,5	1050,2
1	11,8	12,9	21,0	30,3	53,4	85,8	127,5	178,4	308,0	474,7	1053,4
1,245	15,1	16,2	24,3	33,6	56,7	89,1	130,8	181,7	311,4	478,0	1056,7
1,5	18,7	19,8	27,9	37,2	60,3	92,7	134,4	185,3	315,0	481,6	1060,3
2	26,1	27,3	35,4	44,7	67,8	100,2	141,9	192,8	322,4	489,1	1067,8
2,52	34,4	35,6	43,7	52,9	76,1	108,5	150,2	201,1	330,7	497,4	1076,1
3	42,5	43,7	51,8	61,1	84,2	116,6	158,3	209,2	338,8	505,5	1084,2
4	60,7	61,9	70,0	79,3	102,4	134,8	176,5	227,4	357,0	523,7	1102,4
5	80,6	81,8	89,9	99,1	122,3	154,7	196,3	247,3	376,9	543,6	1122,3
6	102,0	103,2	111,3	120,6	143,7	176,1	217,8	268,7	398,3	565,0	1143,7
7	125,0	126,2	134,3	143,5	166,7	199,1	240,8	291,7	421,3	588,0	1166,7
8	149,5	150,6	158,7	168,0	191,1	223,5	265,2	316,1	445,7	612,4	1191,1
9	175,3	176,5	184,6	193,8	217,0	249,4	291,1	342,0	471,6	638,3	1217,0
10	202,6	203,8	211,9	221,1	244,3	276,7	318,3	369,3	498,9	665,6	1244,3
11	231,2	232,4	240,5	249,8	272,9	305,3	347,0	397,9	527,5	694,2	1272,9
12	261,2	262,4	270,5	279,7	302,9	335,3	377,0	427,9	557,5	724,2	1302,9

Appendix C

Electromagnetic and thermal models meshes

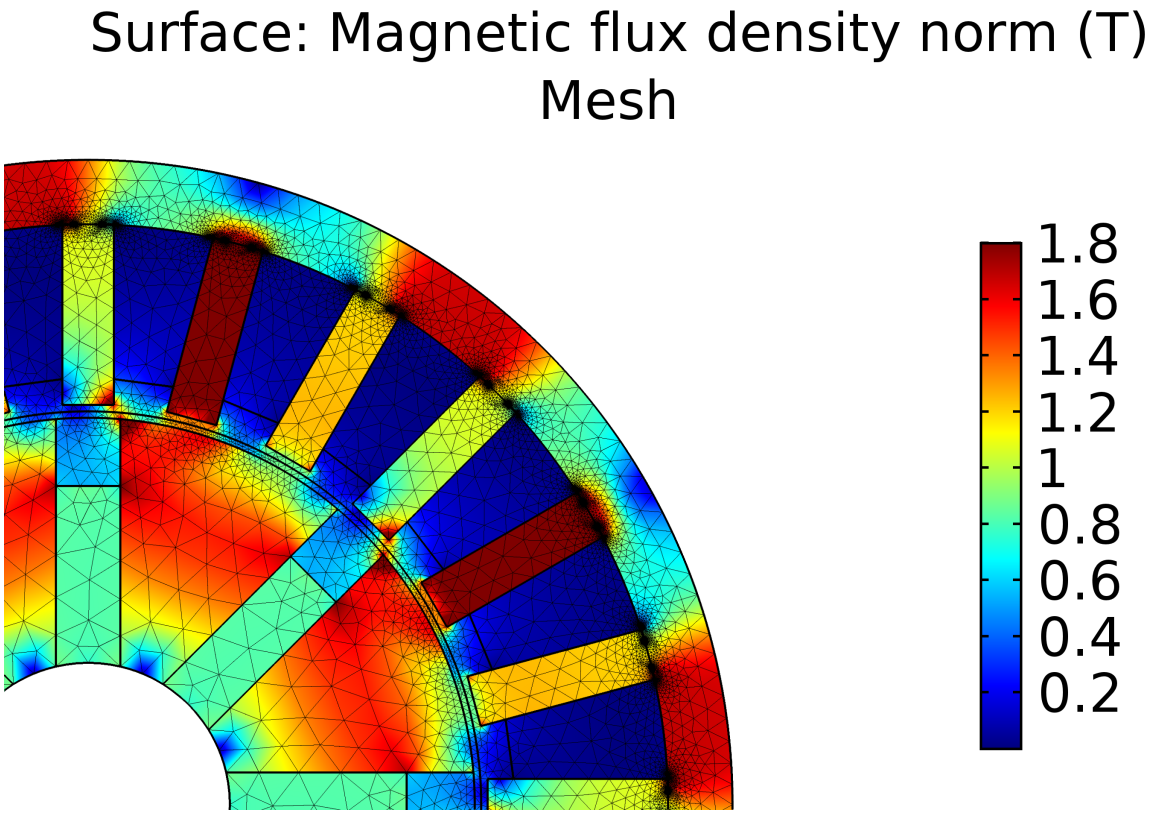

Figure C.1: Mesh of the best result with 24 slots used during the electromagnetic and thermal analysis

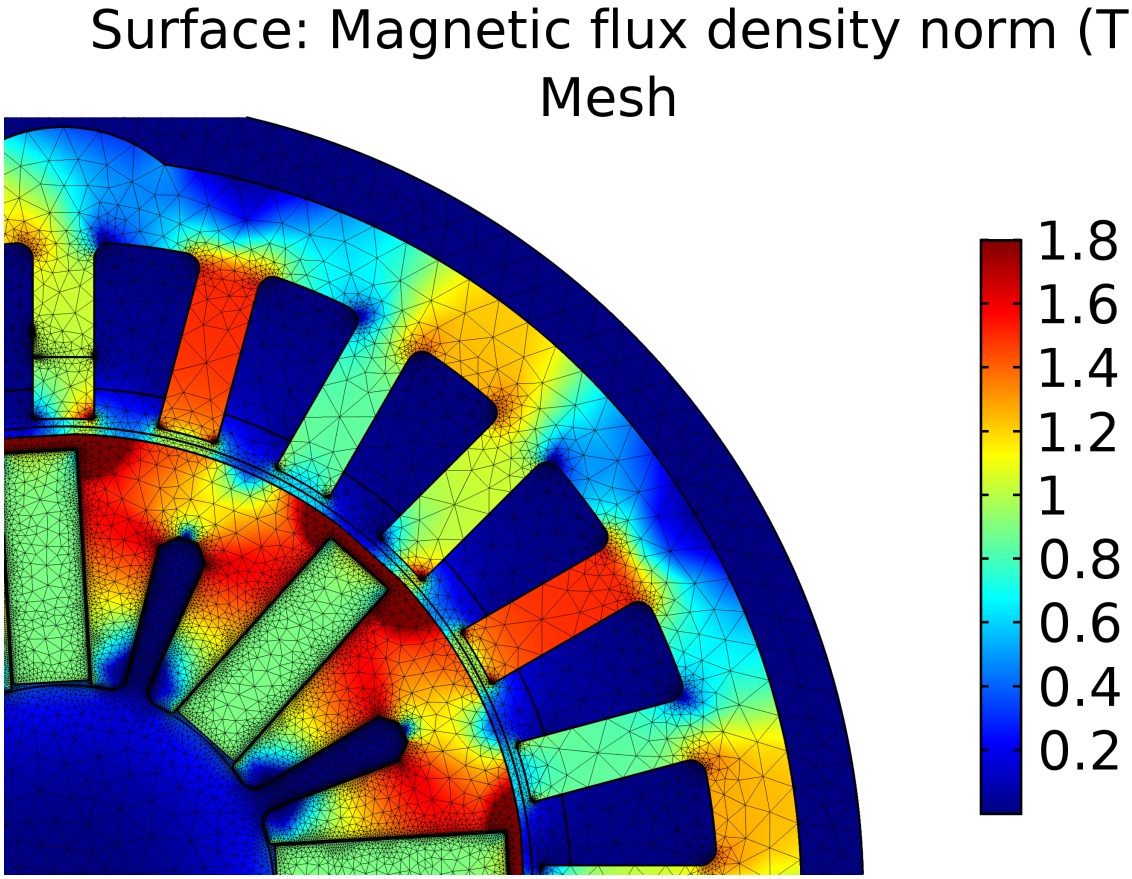

Figure C.2: Mesh of the final (after iterations) result with 24 slots used during the electromagnetic and thermal analysis

Appendix D

Optimization results

D.1 Optimized results from the third version software

Table D.1: Motor optimization version 3

number	pop_size	gen_limit	total	time [h]	torque [Nm]	weight[kg]	[Nm/kg]	slots	poles
44	20	10	200	20,9			error		
45	20	15		101,3	20,5	2,2	9,2	24	8
46	30	12	360	41,2	28,1	2,6	10,9	24	8
47	30	12	360	41,2	28,1	2,5	10,9	24	8
48	50	15	750	0,0			error		
49	30	15	450	51,4	2,9	1,8	1,6	12	8
50	30	12	360	17,4	3,8	1,6	2,3	12	8
51	30	5	150	15,0			error	24	8
52	30	10	300	14,4	31,0	2,1	14,9	24	8
53	30	15	450	4,9	31,0	2,1	14,9	24	8
54	30	7	210	19,7	19,3	2,1	9,3	24	8
55	30	4	120	8,4	error		error		
56	30	6	180	3,1			13,7	24	8
57	30	6	180	13,6			12,5	24	8
58	30	15	450	19,4	30,6	1,9	16,3	24	8
59	50	6	300	23,2			13,0	24	8
60	50	20	1000	58,5	33,7	2,1	16,1	24	8
61	50	10	500	33,7	31,7	2,2	14,4	24	8

D.2 Optimized results from the second version software

Table D.2: Motor optimization version 2

number	pop_size	gen_limit	total individuals	total time [h]	torque[Nm]	weight[kg]	ratio[Nm/kg]
1	15	5	75	0,9	0,1	2,1	0,1
2	20	8	160	3,1	3,7	3,9	1,0
3	20	8	160	5,1	3,0	3,5	0,9
4	50	10	500	11,8	7,0	4,4	1,6
5	25	8	200	5,3	3,9	4,3	0,9
6	50	10	500	12,0	7,0	4,4	1,6
7	50	10	500	6,1	4,8	4,4	1,1
8	10	5	50	5,0	4.9		
9	50	10	500	15,0	5,2	3,3	1,6
10	10	3	30	4,6	10,5	3,0	3,5
11	25	10	250	4,6	9,4	3,1	3,0
12	40	10	400	7,3	6,1	2,5	2,4
13	25	10	250	4,9	5,5	2,9	1,9
14	10	5	50	1,8	11,2	3,1	3,6
15	40	10	400	16,9	12,5	3,2	3,9
16	10	1	10	6,7	10,5	3,0	3,6
17	10	3	30	2,5	10,5	3,0	3,6
18	50	20	1000	3,2	9,5	3,1	3,1
19	100	20	2000	64,0	16,5	3,6	4,6
20	25	8	200	1,9			#DIV/0!
21	15	5	75	11,1	12,6	3,0	4,2
22	15	5	75	5,6	11,6	2,9	4,0
23	20	5	100	9,8	15,0	3,1	4,8
24	20	5	100	5,0	12,2	2,9	4,2
25	40	10	400	5,0	18,0	3,0	5,9
26	15	5	75	6,1	15,4	3,1	5,0
27	40	10	400	7,3	19,4	3,4	5,7
30	10	5	50	8,8	14,2	3,0	4,7
28	10	3	30	9,2	15,8	3,0	5,2
29	10	5	50	6,5	15,8	3,0	5,2
31	20	8	160	7,8	16,8	3,1	5,4
32	20	15	300	13,3	18,6	3,5	5,3
33	30	20	600	18,6	16,0	3,6	4,4
34	40	15	600	22,1	15,4	3,3	4,7
35	40	20	800	24,6	18,1	3,3	5,5
36	40	27	1080	15,0	17,6	3,2	5,5
37	50	26	1300	26,9	15,6	3,0	5,2
38	50	50	2500	28,6	17,9	3,2	5,6
39	30	10	300	15,3	22,5	3,1	7,3
40	30	30	900	25,0	22,5	3,1	7,3
41	50	30	1500	45,6	21,9	2,7	8,2
42	30	9	270	9,4	14,5	2,4	6,1
43	30	10	300	22,8	27,4	2,4	11,6

D.3 Optimized results from the first version software

Table D.3: Optimization version 1 results

number	pop_size	gen_limit	total individuals	total time [h]	torque[Nm]	weight [kg]
1	8	10	80	0,0	error	error
2	6	20	120	0,0	error	error
3	10	20	200	0,0	error	error
4	15	20	300	12,4	error	error
5	10	20	200	2,5	error	error
6	20	20	400	2,9	error	error
7	15	40	600	0,0	error	error
8	20	20	400	3,7	error	error
9	20	20	400	3,9	error	error
11	10	10	100	4,7	error	error
12	20	20	400	9,7	error	error
13	30	20	600	31,8	error	error
14	15	15	225	38,2	error	error
15	30	20	600	31,5	error	error
16	4	3	12	1,6	0,8778	3.68
17	10	10	100	4,2	2,416344	3,462
18	6	3	18	1,0	47,11164	3,08
19	8	5	40	3,5	15,7092	3,48
20	10	8	80	1,7	5,3352	2,44
21	8	3	24	0,8	14,1132	3,25
22	8	3	24	0,9	error	error
23	20	4	80	2,8	9,2112	3,07
24	30	16	480	23,4	22,344	3.55
26	40	20	800	55,5	33,1284	3,62
27	50	18	900	66,9	59,4624	3,25
28	20	20	400	37,1	24,8406	3,85
29	25	20	500	42,0	14,6376	3.68
30	25	10	250	11,9	16,0968	3.17
31	15	5	75	4,2	error	error
32	25	10	250	12,4	10,26	
34	25	10	250	16,0	16,0968	3.17
35	25	10	250	16,6	12,996	3.56
36	25	10	250	16,8	11,7192	3.25
37	25	10	250	16,8	11,9928	3.61
38	25	10	250	20,3	11,6964	3.84
39	15	5	75	21,5	18,7416	4.6
40	50	50	2500	23,2	0	3.7
41	50	50	2500	43,9	error	error
42	25	10	250	47,7	25,4904	3.81
43	20	8	160	38,6	15,7092	3.9
44	25	10	250	33,2	24,6012	3,7
45	15	5	75	11,4	2,5764	2.46
46	20	10	200	39,1	4,446	
47	50	50	2500	143,0	15,5268	
48	20	10	200	49,4	2,3484	
49	20	10	200	41,9	11,0808	
50	20	10	200	41,8	11,0808	
51	10	10	100	30,0	14,4552	
52	10	10	100	17,8	14,4552	
53	10	10	100	31,0	5,244	

Appendix E

Clearance fit table

Type of Fit	Description	Symbol
Clearance	*Loose running fit:* for wide commercial tolerances or allowances on external members	H11/c11
	Free running fit: not for use where accuracy is essential, but good for large temperature variations, high running speeds, or heavy journal pressures	H9/d9
	Close running fit: for running on accurate machines and for accurate location at moderate speeds and journal pressures	H8/f7
	Sliding fit: where parts are not intended to run freely, but must move and turn freely and locate accurately	H7/g6
	Locational clearance fit: provides snug fit for location of stationary parts, but can be freely assembled and disassembled	H7/h6
Transition	*Locational transition fit:* for accurate location, a compromise between clearance and interference	H7/k6
	Locational transition fit: for more accurate location where greater interference is permissible	H7/n6
Interference	*Locational interference fit:* for parts requiring rigidity and alignment with prime accuracy of location but without special bore pressure requirements	H7/p6
	Medium drive fit: for ordinary steel parts or shrink fits on light sections, the tightest fit usable with cast iron	H7/s6
	Force fit: suitable for parts that can be highly stressed or for shrink fits where the heavy pressing forces required are impractical	H7/u6

Figure E.1: Clearance fit table meaning [41]

Appendix F

MJF general information

F.1 Cost Analysis

slots	24
V_copper(m3)	1.11e-4
V_iron(m3)	4.43e-4
V_magnet (m3)	3.85e-5
V_shaft (m3)	7.37e-5
V_glue (m3)	2.65e-4

Density_copper [Kg/m3]	8900
Density_iron [Kg/m3]	7600
Density_magnet [Kg/m3]	7500
Density_shaft [Kg/m3]	7800
Density_glue [Kg/m3]	1000

Weight_copper [Kg]	0.99
Weight_iron [Kg]	3.37
Weight_magnet[Kg]	0.29
Weight_shaft [Kg]	0.58
Weight_glue [Kg]	0.26
Total Weight [Kg]	5.49

Price_copper [EUR]	100
Price_iron [EUR]	800
Price_magnet [EUR]	70
Price_shaft [EUR]	103.5
Price_bearings [EUR]	14
Total Price [EUR]	1087.5

Figure F.1: MJF cost analysis.

Motor Data sheet

Name **MJE_v0** Formula Student Date: 23.06.2017

Motor Description:

Motor type:	synchronous
Cooling type:	Water
Degree of protection:	IP 22
Insulation class:	H(180ºC)

Performance:

Maximum torque:	20 Nm
Rated torque :	6 Nm
Maximum power:	20 kW
Rated power :	6 kW
Rated speed :	9000 rpm
No-load-speed :	12000 rpm

Mechanical data:

Motor mass "m":	5,05 kg
Inertia "J":	2,66 kgcm²
Mech. speed limit "Nmax":	20000 rpm

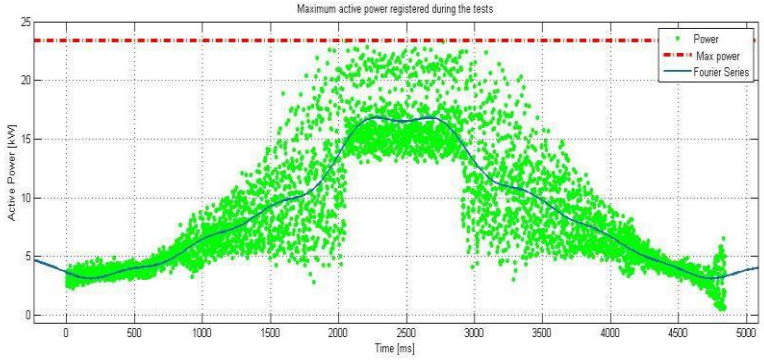

Electrical data:

Rated voltage:	350 V
Rated current:	16,7 Arms
Maximum current:	50 Arms
Duration for maximum current:	16 s
Torque constant " kt":	0,4 Nm/Arms
Voltage constant "ke":	24 V/kRPM
Connection type:	Y
Number of poles:	8 Pole
Terminal resistance "Rtt":	0,42 Ohm
Terminal inductance "Ltt":	1,39 mH
Torque/Weight (active) Ratio:	5,26
Torque/Weight (total) Ratio:	4

	Velocity[RPM]												
Torque [Nm]	0,5	1	2	3	4	5	6	7	8	9	10	11	12
1	0,52	0,55	0,57	0,60	0,61	0,63	0,66	0,70	0,68	0,67	0,65	0,60	0,58
2	0,46	0,54	0,59	0,60	0,65	0,67	0,71	0,72	0,73	0,75	0,73	0,72	NaN
3	0,44	0,53	0,62	0,70	0,73	0,76	0,80	0,81	0,82	0,85	0,86	NaN	NaN
4	0,43	0,56	0,65	0,75	0,76	0,80	0,82	0,88	0,91	0,92	NaN	NaN	NaN
6	0,42	0,62	0,72	0,79	0,81	0,83	0,84	0,86	0,93	0,94	NaN	NaN	NaN
8	0,42	0,52	0,73	0,73	0,74	0,76	0,80	0,85	0,90	0,92	NaN	NaN	NaN
10	0,37	0,52	0,66	0,68	0,68	0,69	0,75	0,80	0,85	0,90	NaN	NaN	NaN
12	0,35	0,49	0,62	0,64	0,66	0,68	0,70	0,75	0,80	NaN	NaN	NaN	NaN
14	0,31	0,46	0,58	0,60	0,62	0,65	0,67	0,70	0,75	NaN	NaN	NaN	NaN

F.2 MJF Gantt Chart

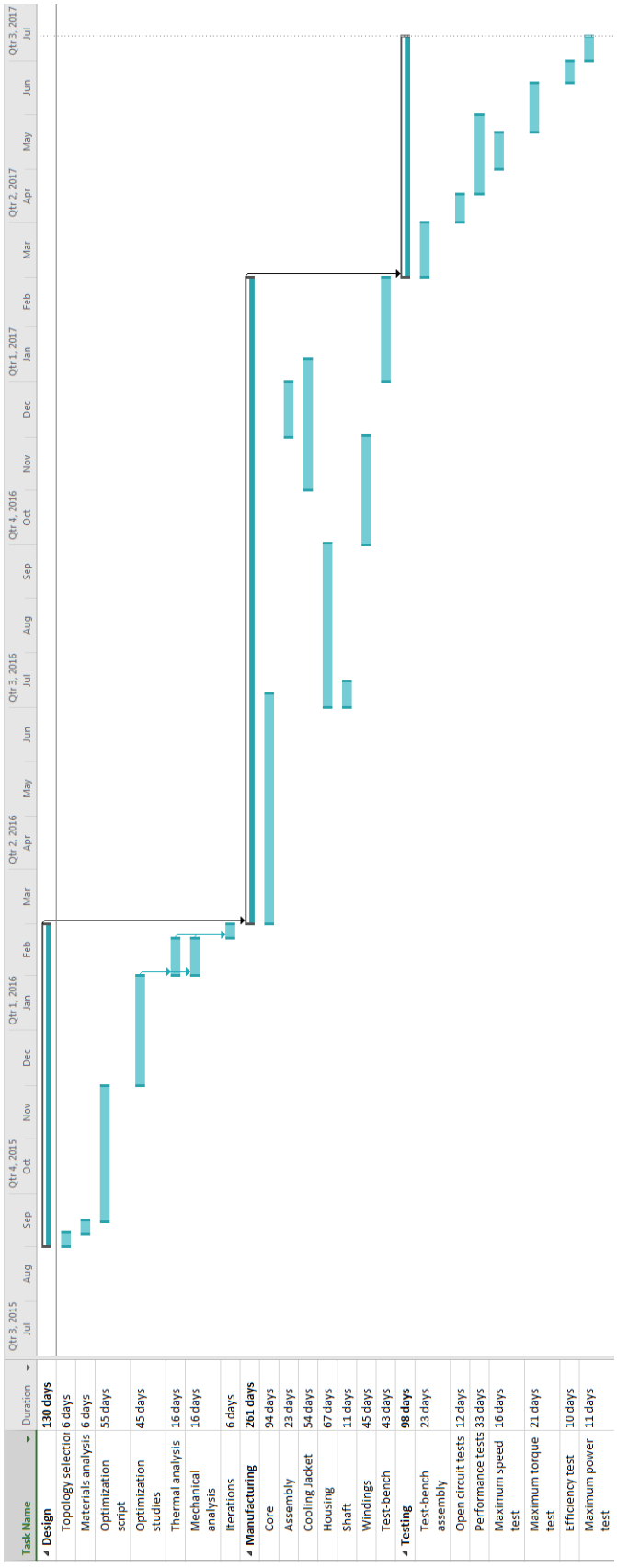

Figure F.2: Render of the MJF motor CAD.

Appendix G

Tests data

G.1 Number of turns per coil test

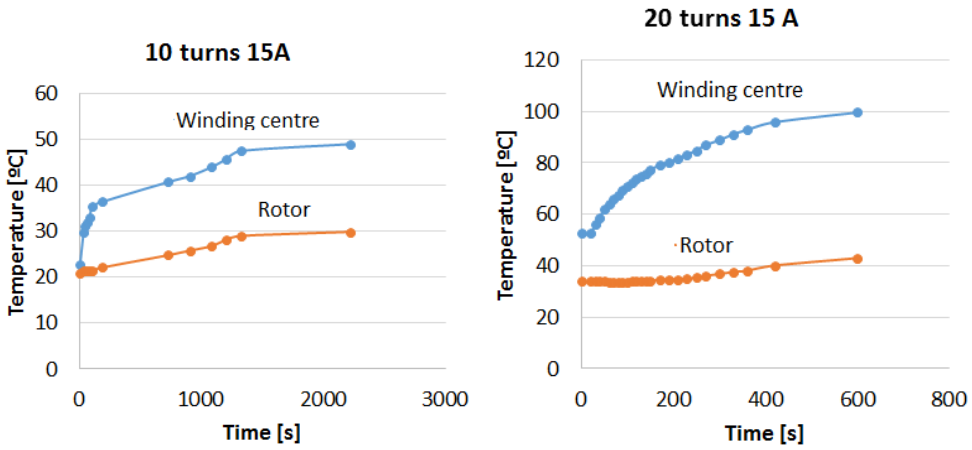

Figure G.1: MJF temperature data of test with one phase with a current of 10 A.

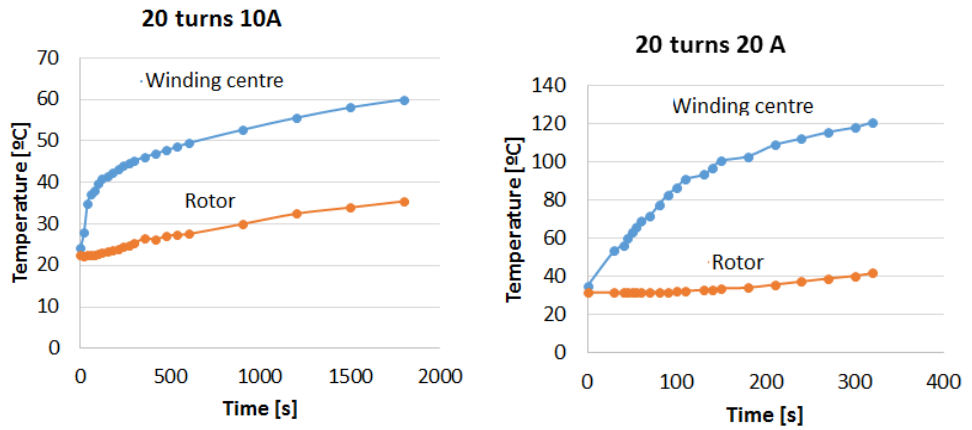

Figure G.2: MJF temperature data of test with one phase with 20 turns per coil.

G.2 Maximum torque test

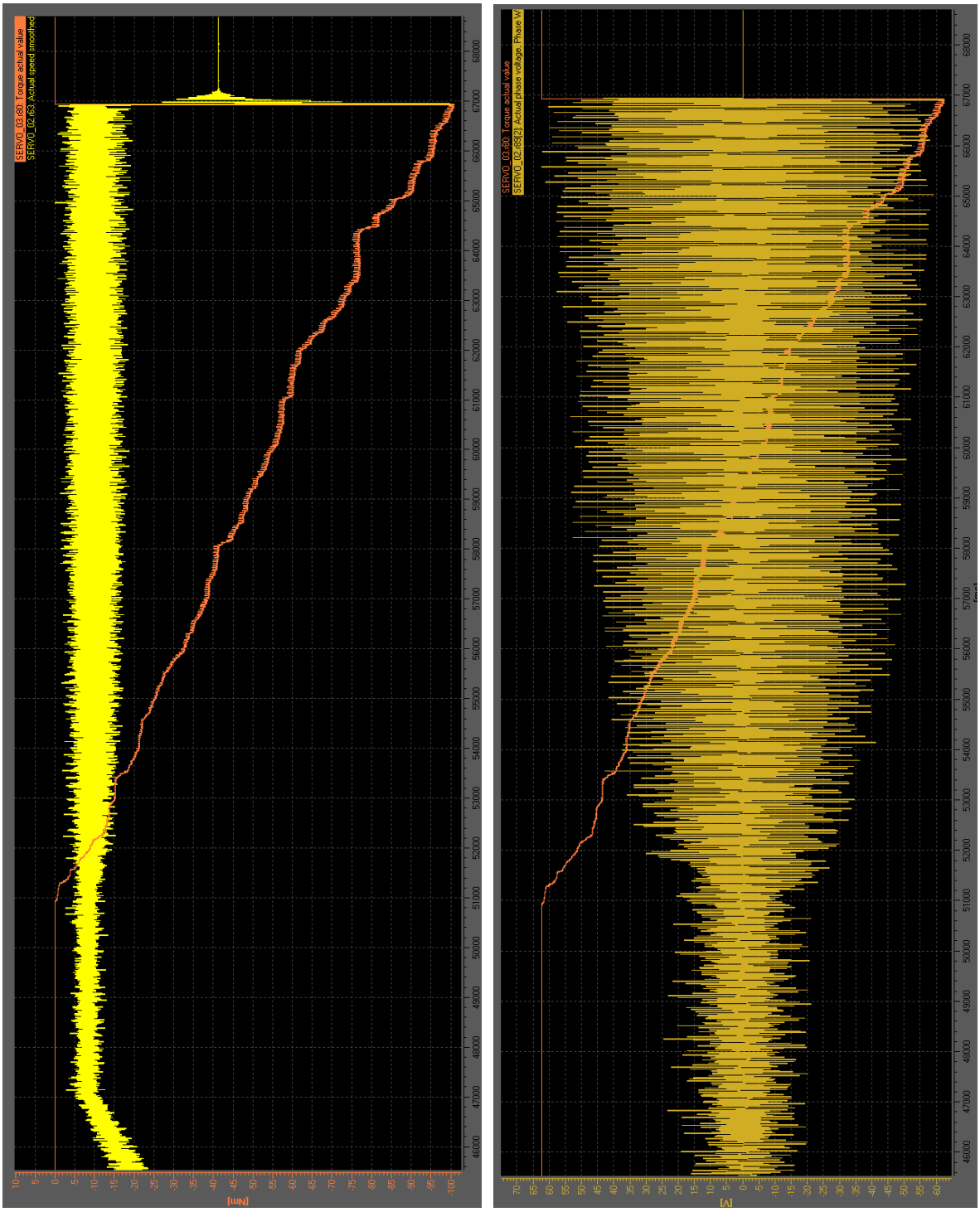

Figure G.3: Siemens torque and MJF line-neutral voltage registered during maximum torque test.

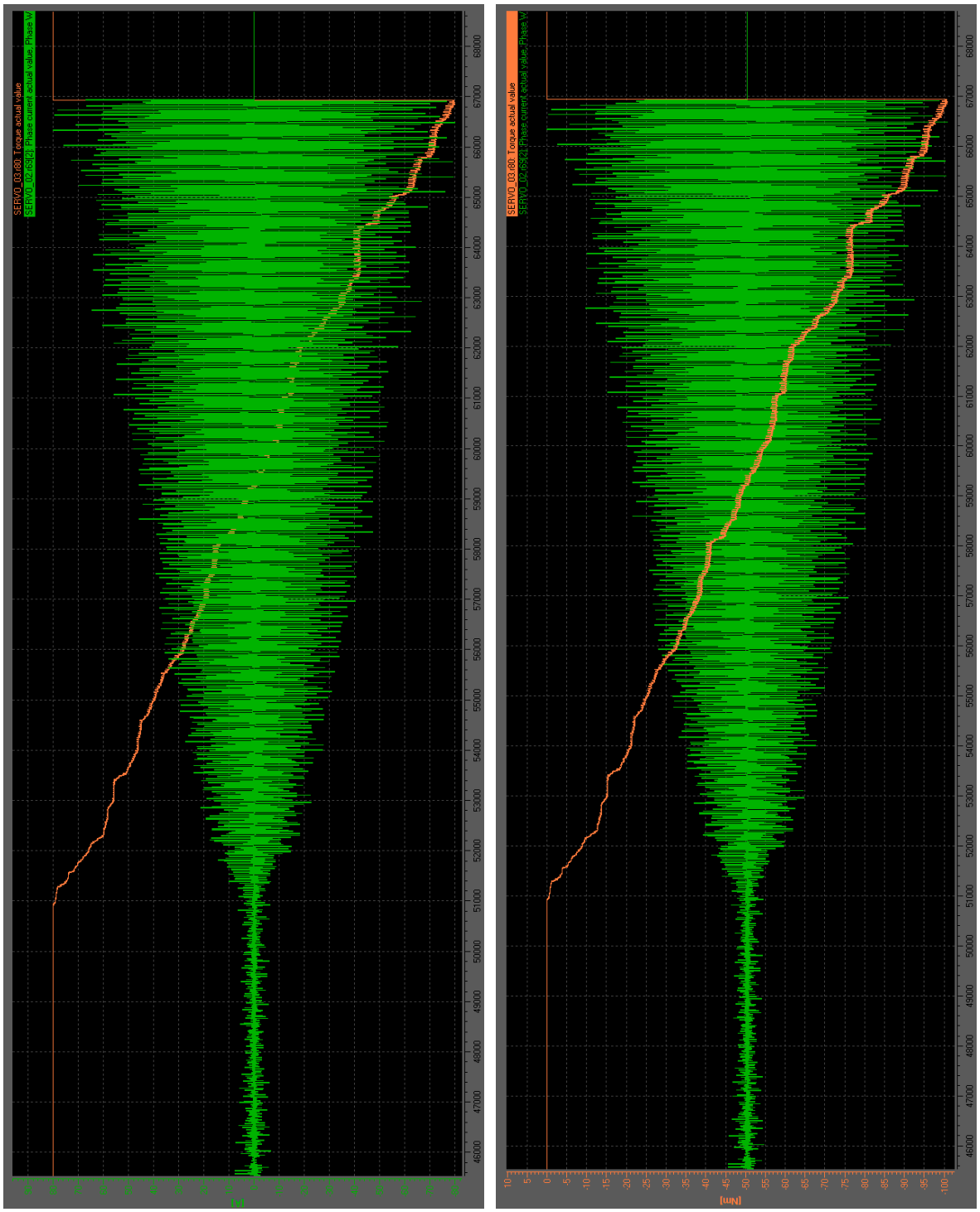

Figure G.4: MJF phase current and Siemens torque registered during maximum torque test.

G.3 Maximum velocity test

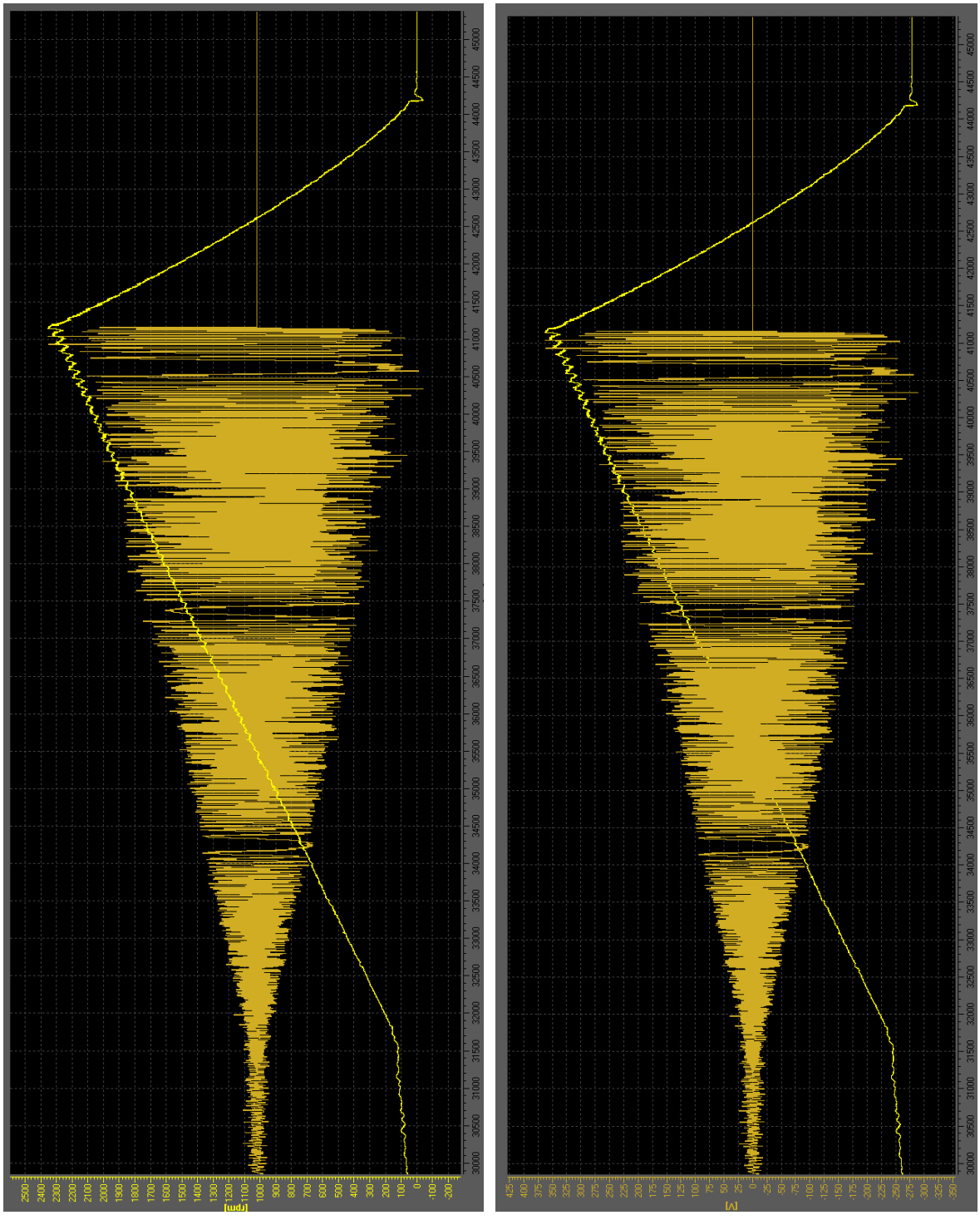

Figure G.5: Siemens velocity and MJF line-neutral voltage registered during velocity test without load.

G.4 Maximum power test

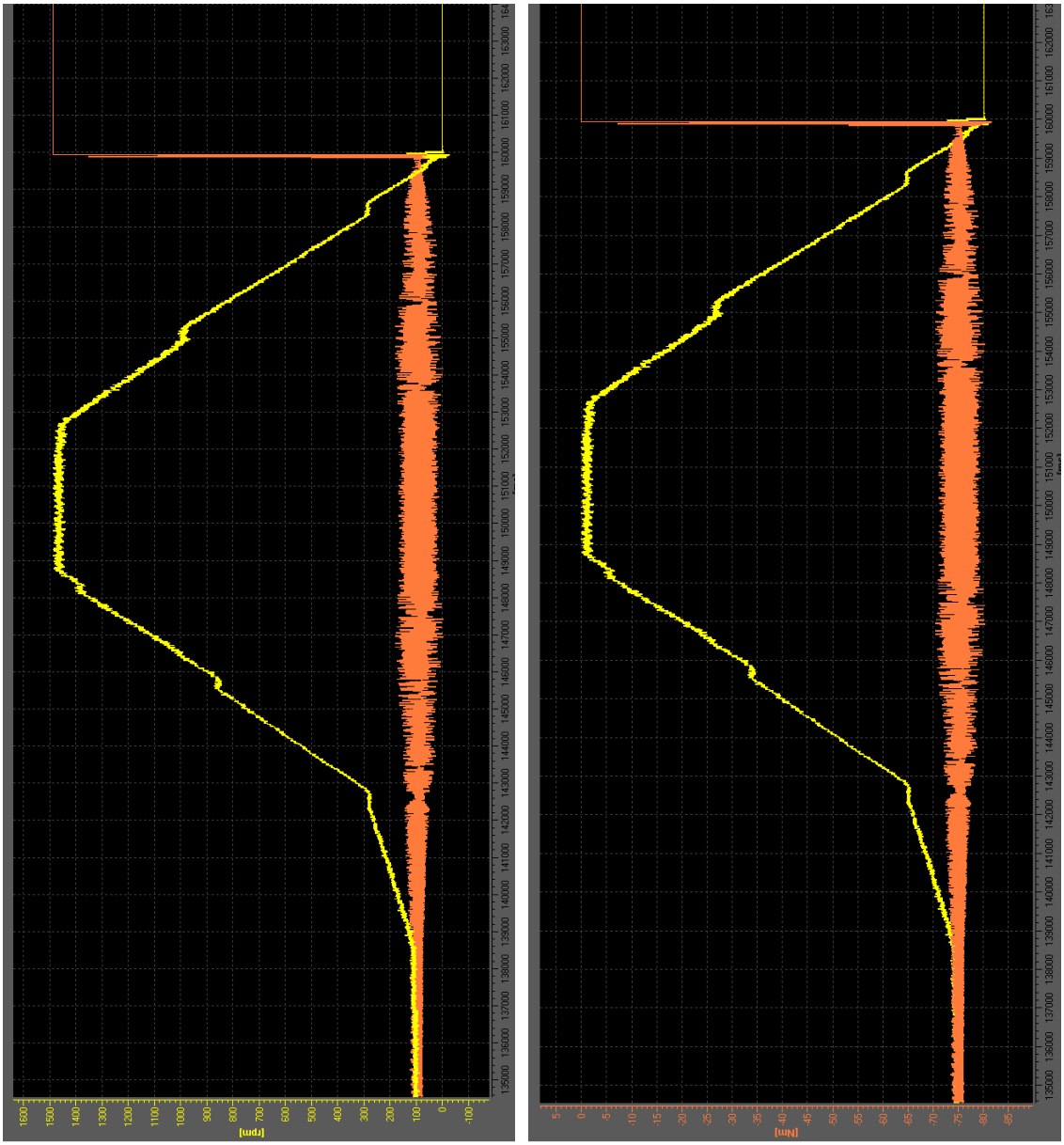

Figure G.6: Siemens velocity and torque registered during maximum power test.

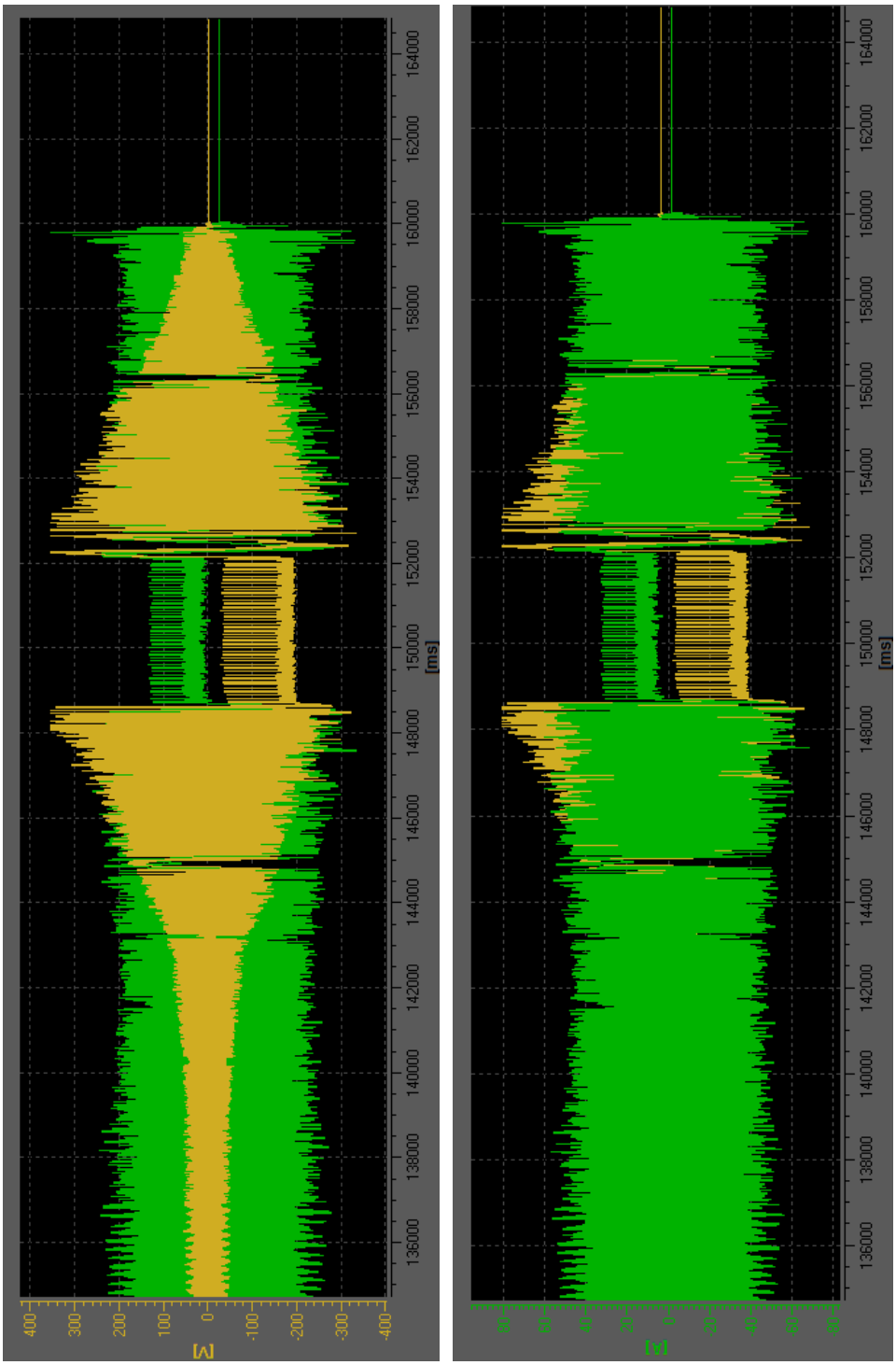

Figure G.7: MJF line-neutral voltage and phase current registered during maximum power test.